THE UNIVERSITY *of* EDINBURGH

Characterization of Lignin Degrading Enzymes from Fungi and Bacteria

Fatai Olumide Bello

2018

Doctor of Philosophy (PhD) – The University of Edinburgh - 2018

Abstract

Fossil fuels serve as a source of raw materials and energy worldwide but their continued use is unsustainable due to rapidly depleting sources and the harm their use causes to the environment. Lignocellulosic biomass is a renewable and sustainable source that can contribute to the generation of fuels and raw materials which fossil fuels, a non-renewable resource currently provides. Lignin degrading enzymes are very important for the full break down of biomass as lignin content is closely linked with biomass recalcitrance. In this project, a fungal enzyme, identified as a laccase from *Panus rudis* was cloned and expressed using the *Pichia pastoris* expression system. It showed an ability to degrade several lignin model compounds. Several techniques including scanning electron microscopy (SEM), Fourier-transform infrared (FTIR) spectroscopy and Fourier-transform ion cyclotron resonance (FTICR) spectrometry were used to investigate the effect of this laccase on Kraft lignin in the presence of several mediators. Two bacterial lignin degrading enzymes from *Pseudomonas putida* and *Bacillus subtilis* were also investigated. Using X-ray crystallography, structural data for both enzymes was obtained and the active site residues identified. These studies have enabled a better understanding of lignin degrading enzymes and the lignin breakdown process.

Declaration

I hereby declare that the contents of this thesis was written by me and all work in it; unless otherwise stated, all the results present herein are my own work. This work has not been submitted for any other degree or personal qualification.

…….

FATAI OLUMIDE BELLO

Acknowledgements

Firstly, my sincere and eternal appreciation goes to Dr Louise Horsfall for the opportunity to carry out my Ph.D. research in her laboratory and for all her support, mentoring and understanding during the highs and lows of the whole experience. To Dr Jon Marles-Wright, I am also very grateful for his total support and his help with all of the X-ray crystallography aspect of the Ph.D. I am also very grateful to Professor Chris French for stepping in and taking over supervision for his support and advice during Louise's absence and Professor Alistair Elfick for being on my thesis committee.

I owe a debt of gratitude and more to Dr Michael Capeness (still the greatest doctor that ever lived) and Dr Matthew Edmundson for all their help with all aspects of the project and also for being very good friends both inside and outside the laboratory. Special thanks and appreciation to Dr Virginia Echavarri-Bravo of the Horsfall laboratory and Drs David Clarke and Logan Mackay in Chemistry for their help with the FTICR-MS aspect of the Ph.D. All other members of the Horsfall laboratory, past and present are also appreciated for their help at various times as well.

I acknowledge the help of my family members for all their words of prayer and encouragement during my time here. Special appreciation to Emma Camm who has supported me and always believed in me throughout the course of my Ph.D., particularly through its final stretch which was most challenging indeed.

Finally, I would like to thank the Nigerian government for the opportunity to do this Ph.D. in the first place.

Abbreviations

ABTS	2,2'-azino-bis(3-ethylbenzothiazoline-6-sulphonic acid
ACN	Acetonitrile
BLAST	Basic Local Alignment Search Tool
BMGY	Buffered Glycerol Complex Medium
BMMY	Buffered Methanol Complex Medium
Cm	Chloramphenicol
Cop A	Copper resistance protein A
°C	Degrees Celsius
DTT	Dithiothreitol
EDTA	Ethylenediaminetetraaceticacid
FF	Fast Flow
x g	Gravitational force
HBT	1-hydroxybenzotriazole
IMAC	Immobilized Metal Affinity Chromatography
IEC	Ion Exchange Chromatography
IPTG	Isopropyl-β-D1-thiogalactopyranoside
Kn	Kanamycin
LB	Lysogeny broth
m/z	mass/charge
MALDI-TOF	Matrix Assisted Laser Desorption/Ionization-Time-of-Flight
MES	2-(N-morpholino)ethanesulfonic acid
MPa	Megapascals
µl	Microlitres
µM	Micrometres

MWCO	Molecular weight cut-off
nl	nanolitres
nm	Nanometres
NCBI	National Centre for Biotechnology Information
OD_{600}	Optical density at 600nm
PEG	Polyethylene glycol
PIPES	2-(4-(2-Hydroxyethyl)-1-piperazinyl)ethanesulfonic acid sodium salt
PMSF	Phenylmethylsulfonyl fluoride
rpm	Revolutions per minute
Se-Met	Selenomethionine
SEC	Size Exclusion Chromatography
SDS-PAGE	Sodium dodecyl sulphate polyacrylamide gel electrophoresis
PVDF	Polyvinylidene fluoride
RT	Room temperature
U/ml	Units/millilitres
kPsi	Kilopound per square inch
YPD	Yeast Extract Peptone Dextrose Medium

Table of Contents

List of Figures

Chapter 1: Introduction

The population worldwide is projected to reach 10 billion by the end of this century with severe consequences for the people and the environment. Given that both energy and food provision is projected to increase, it will become more difficult to provide for this huge population (Azadi et al., 2013). At present, society faces the difficulty of searching for alternative and renewable energy sources to the presently used fossil fuels. The potential energy crisis could be averted with the development of processes that are based on renewable and sustainable substrates (Singhvi, Chaudhari and Gokhale, 2014). Lignocellulosic biomass (primarily composed of cellulose, hemicellulose and lignin) has long been recognized as a potential sustainable source of mixed sugars for fermentation to biofuels and other biomaterials (Abdel-Hamid, Solbiati and Cann, 2013). Several technologies have been developed during the past 80 years that allow biomass conversion to occur, but the efficiency of the processes have limited their use (Himmel et al., 2007).

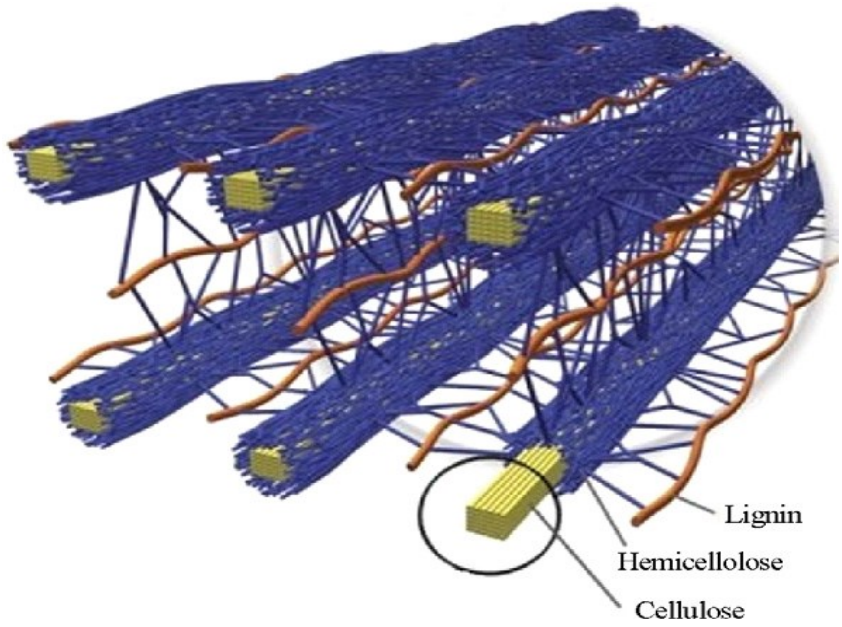

Figure 1. Lignocellulosic biomass structure (Doherty, Mousavioun and Fellows, 2011)

Cellulose and hemicellulose are regarded as high value components of lignocellulose because they can be fermented into higher value chemicals such as glucose, levulinic acid

and hydroxymethylfurfural (Wei and Wu, 2017), whereas the vast majority of lignin is burned to provide a source of heat to industry (Gosselink, 2004). Economically, burning lignin for fuel makes no financial sense, when used for fuel the lignin's value is 0.18 US dollars/kg while value-added chemicals could increase the value of the lignin to as high as 1.08 US dollars/kg (Vishtal and Kraslawski, 2011).

1.1 Lignin Structure

Lignin is majorly composed of three major monomeric units or monolignols; *p*-coumaryl alcohol, coniferyl alcohol and sinapyl alcohol (Higuchi, 1990). The monolignols are biosynthesised from phenylalanine, an amino acid, in a process called the phenylpropanoid pathway, in the cytosol of plant cells. The first step in the pathway is the deamination of phenyalanine to cinnamate by phenylalanine ammonia lyase (PAL) (Rasmussen and Dixon, 1999). This is the beginning of a series of transformations involving various enzymatic transformations that eventually ends when the three monomeric units (*p*-coumaryl alcohol, coniferyl alcohol and sinapyl alcohol) are biosynthesised (Liu, Luo and Zheng, 2018). *p*-coumaryl alcohol, coniferyl alcohol and sinapyl alcohol are inserted into the lignin polymer as 4-hydroxyphenol (H), guaiacyl (G) and sinapyl (S) units respectively (Yoshida, Cheynier and Quideau, 2016). After their biosynthesis, the monolignols are oxidatively radicalised, and the radicalised monolignols coupled preferentially at the β positions to form dimers and oligomers linked by several bonds including arylglycerol-β-aryl ether (β-O-4), pinoresinol (β-β'), phenylcoumaran (β-5'), spirodienone and diphenylethane (β-1') bonds as shown in Figure 3 (Crestini et al., 2011). Further polymerization of the dimeric and the oligomeric units formed with more monomeric radicals goes on until a complex branched polymer, lignin results (Figure 3) (Pandey and Kim, 2011). Products from incomplete monolignol biosynthesis may also be incorporated into the lignin polymer (Vanholme et al., 2008).

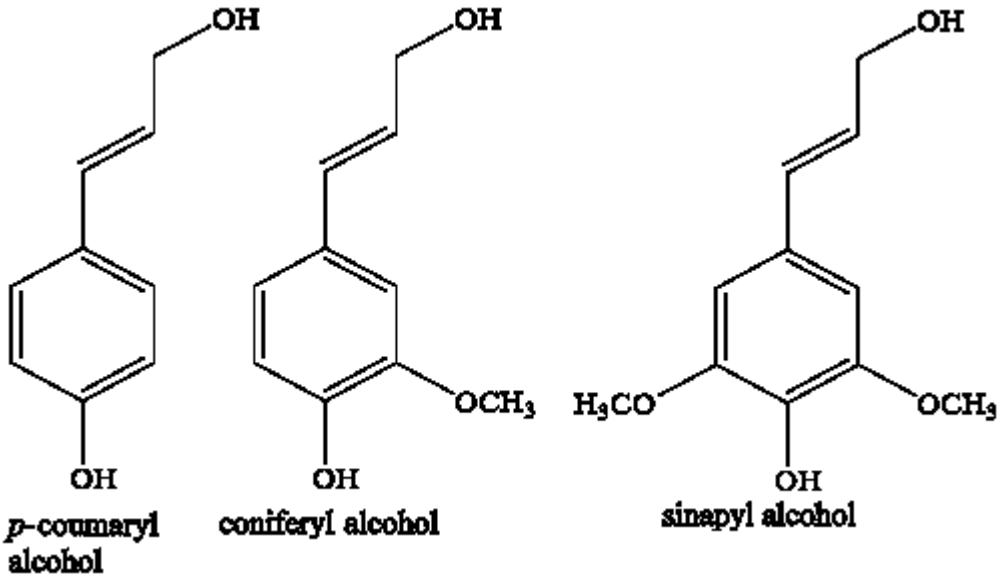

Figure 2. Major monolignols in lignin

The high degree of the structural heterogeneity of lignin is believed to be a powerful defensive mechanism, making it difficult for pathogens to develop effective methods of degradation (Ralph et al., 2004).

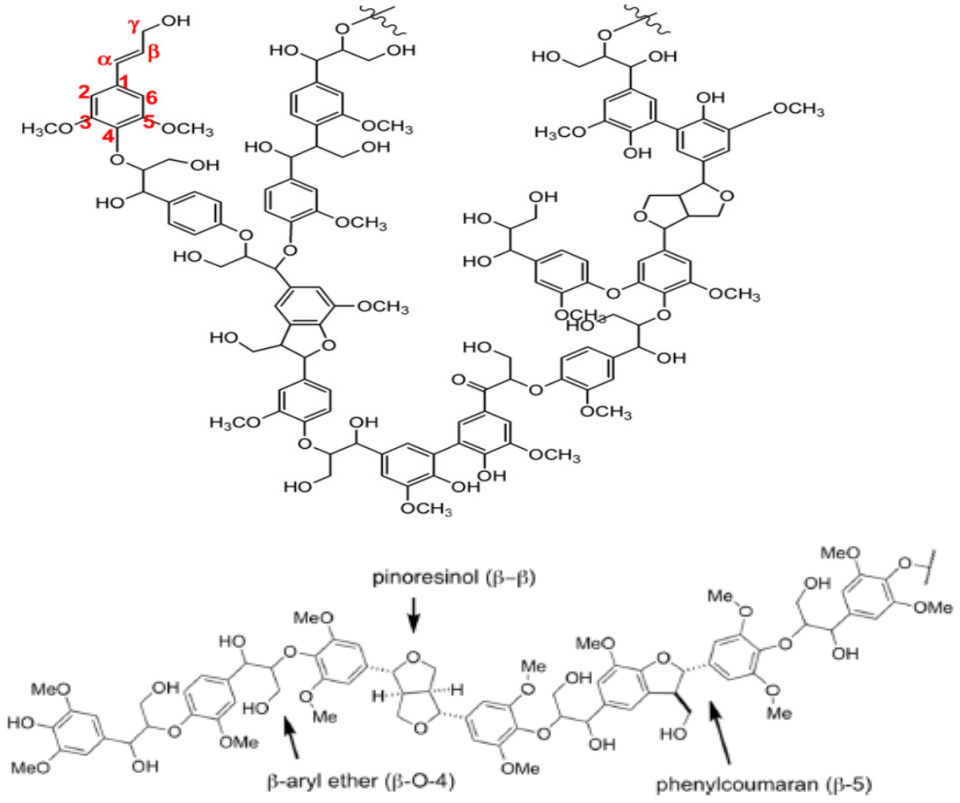

Figure 3. A fragment of a typical lignin macromolecule and some of the inter-unit linkages present within it. These does not represent the full molecule nor all of the inter-unit linkages, and the overall structures and inter-unit linkages vary based on the type of lignin. The diagrams are taken from (Zhao and Lercher, 2013 and Lancefield et al., 2016).

To utilize lignocellulosic biomass efficiently, the effective degradation of lignin is very important. Currently, the biofuel, paper milling and textile industries predominantly make use of harsh, expensive and energy consuming pre-treatment technologies to remove lignin from biomass (Weng et al., 2008).

1.2 Organisms Involved in Lignin Degradation

Fungi and bacteria have the ability to degrade lignin with varying degrees of success (Sigoillot et al., 2012). The fungal class, basidiomycetes are the most efficient lignin degraders with *Phanaerochete chrysosporium*, a member of this group the best studied lignin degrading microorganism (Wong, 2009). Species of the fungal classes; zygomycetes, ascomycetes, and deuteromycetes are also involved in lignin degradation (Paliwal et al., 2012). *Streptomyces viridosporus* T7A, *Rhodococccus jostii* RHA1 and *Pseudomonas putida* mt-2 are examples of bacteria capable of lignin degradation (Bugg et al., 2011). Although not as well characterized and believed to be slower than fungal lignin degradation, the environmental adaptability and biochemical versatility of bacteria makes them good candidates for discovering industrially useful lignin degrading enzymes (Wang et al., 2013).

1.3 Enzymes involved in lignin degradation

The complexity of lignin and the wide variety of chemical linkages present in its structure means that several classes of enzymes are involved in lignin degradation (Abdel-Hamid et al., 2013). The two major classes of enzymes known to degrade lignin are the peroxidases (lignin peroxidase, manganese peroxidase, versatile peroxidase and dyp-type peroxidase) and the copper containing laccases (Wong, 2009).

Lignin peroxidases (LiPs) were first discovered in *P. chrysosporium*. They catalyse the H_2O_2 dependent oxidative cleavage of lignin (Wong, 2009). They are a family of monomeric extracellular enzymes, with a molecular mass between 35 and 48 kDa and an isoelectric point

(pI) between 3.1 and 4.7 (Sigoillot et al., 2012). They have one haem group per molecule and are stronger oxidants than classical peroxidases because the iron in the porphyrin ring in LiPs is more electron deficient than in classical peroxidases (Millis et al., 1989). They are capable of oxidizing both the phenolic and non-phenolic components of lignin (Martínez et al., 2005). Manganese peroxidases (MnPs) are haem-containing enzymes that oxidize Mn^{2+} to Mn^{3+}, which in turn can oxidize a large number of phenolic substrates (Abdel-Hamid et al., 2013). Also, first discovered in *P. chrysosporium,* the overall structure of MnPs is similar to LiPs, consisting of two domains with the haem sandwiched in-between (Wong, 2009).

Versatile peroxidases (VPs) are haem-containing lignolytic peroxidases with hybrid molecular architecture combining different oxidation-active sites (Ruiz-Dueñas et al., 2009). They have both the Mn(II)-binding site typical of MnPs, and the tryptophan residue of the LiPs involved in the interaction with aromatic substrates (Camarero et al., 1999). The hybrid molecular structure of VPs enables them to directly oxidize a whole range of compounds (Camarero et al., 1999).

DyP-type peroxidases are a novel class of peroxidases showing no similarity in primary sequence or structure to the other plant, bacterial or fungal peroxidases. They oxidize synthetic high-redox potential dyes of the anthraquinone type, compounds previously unconverted by other peroxidases (Sugano, 2009). DypB also appears to play a major role in lignin degradation by *Rhodococcus jostii* RHA1 (Ahmad et al., 2011).

DyP-type peroxidases are classified into four phylogenetically distinct classes A, B, C, and D (Colpa, Fraaije and van Bloois, 2014). Class A contains a Tat-dependent signal sequence, which could mean that they have a physiological function extracellularly. Classes B and C are putative cytoplasmic enzymes and could be involved in intracellular metabolism. (Ahmad et al., 2011). Classes A to C are of bacterial origin while Class D is mainly fungal variants (Ahmad et al., 2011). The first dyP-type peroxidase was discovered, purified and

characterized in 1995 from cultures of the basidiomycete, *Thanatephorus cucumeris* Dec 1. It was reported to decolorize 18 different types of dyes (Kim and Shoda, 1999). DyP-type peroxidases have a molecular weight ranging between 40 – 60 kDa, are non-covalently bound to the cofactor heme (proto heme IX) and have been discovered as monomeric units and more complex units (dimers to hexamers) (Colpa et al., 2014). X-ray structural analysis and sequence alignments of the DyP-type peroxidases showed that they could not be grouped into the existing families of the plant, bacterial, and fungal peroxidases (Hofrichter et al., 2010). Alignment of primary sequences of different types of DyP-type peroxidases show an identity of roughly 15% and when different classes are aligned the identity between them are as low as 5% (Yoshida et al., 2011). The DyP-type peroxidases are enzymes that do not show common origin when examined on the protein sequence level, but are grouped together based on a common structural fold and their conserved active site residues (Hofrichter et al., 2010), as shown by the alignment in Figure 5. It has been suggested that the DyP family likely evolved from a different ancestral gene, and might be an example of convergent evolution of peroxidase function (Zubieta et al., 2007). A major difference between DyP-type peroxidases and other peroxidases is that they are made up of two domains that contain α-helices and anti-parallel β-sheets, while the other class of peroxidases are primarily α-helical proteins (Colpa et al., 2014). X-ray structural analysis of the Dyp from *Bacteroides thetaiotaomicron* (BtDyp) show that they are made up of α + β domains with each domain individually forming a ferredoxin-like fold (Zubieta et al., 2007). The haem cofactor is sandwiched between these two domains which closely represent the haem-binding motif of class II fungal peroxidases with a major difference being the absence of the distal histidine residue which is always present in the class II fungal peroxidases (Colpa et al., 2014). In dye decolourising peroxidases, the GXXDG motif found in the primary sequence of most of them as shown in Figure 4 is believed to play the role of the absent distal histidine residue (Sugano, 2009).

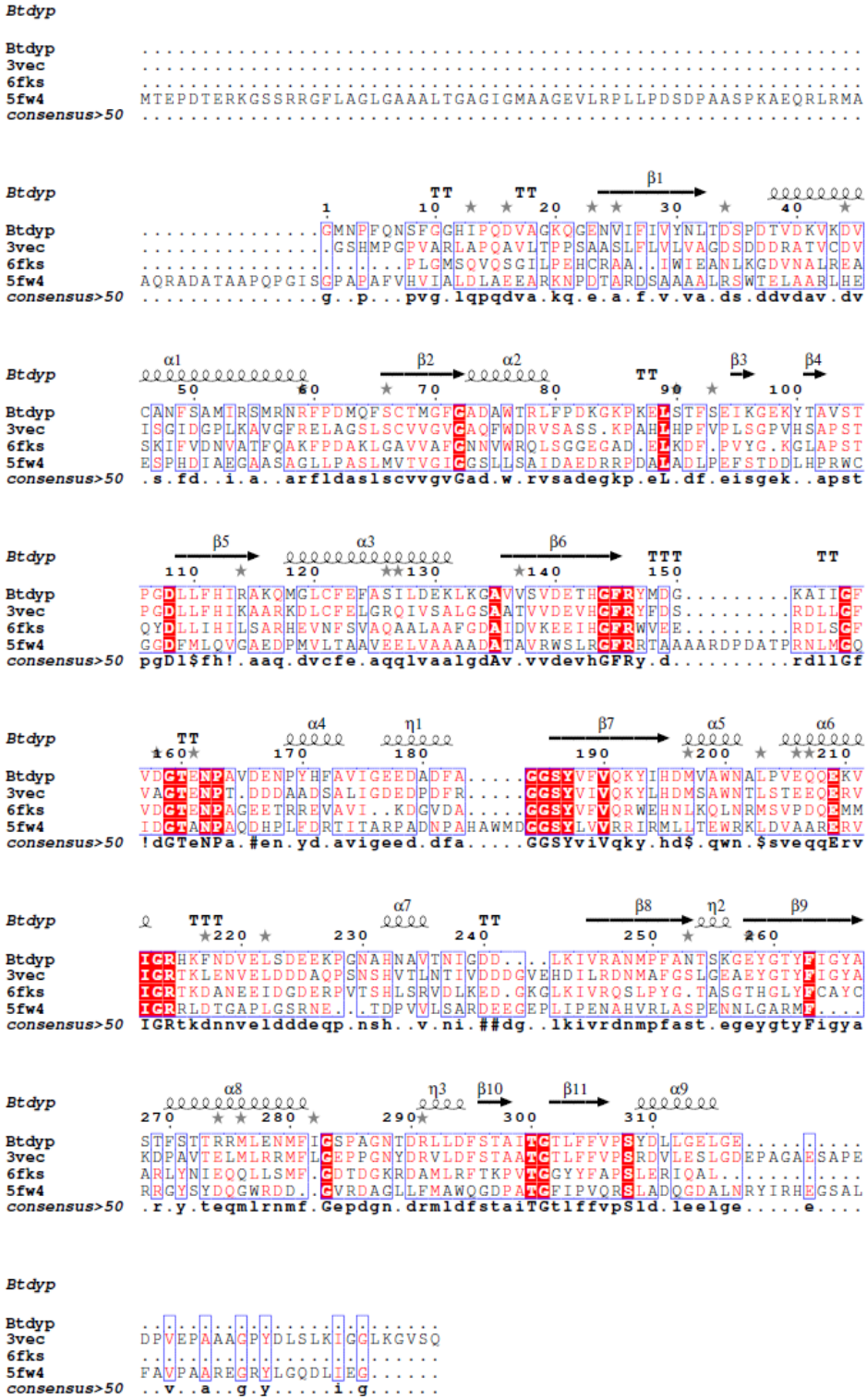

Figure 4. Multiple sequence alignment of some dye-decolourising peroxidases

The primary sequence *Bacteriodes thetaiotaomicron* VPI-5482 dye-decolourising peroxidase was aligned with three other dye-decolourising peroxidases: (A) DypB D153A variant in complex with haem from *Rhodococcus jostii* RHA1, 3VEC; (B) Dye-decolourising peroxidase from *Klebsiella pneumoniae*, 6FKS; (C) Dyp-type peroxidase from *Thermobifida fusca*, 5FW4, 21.59%, 1.8 Å..The alignment was done using Multalin and Clustal Omega (Corpet, 1988, Li et al., 2015) and the output displayed as an ESPript 3.0 file (Robert and Gouet, 2014) The conserved GxxDG sequence around Aspartic acid 286 common to all dye-decolourising peroxidases is present in the concensus sequence of all four peroxidases (Sugano, 2009)

Mutation of the aspartic acid residue in this motif in different Dyp classes has shown a mixed result in its effect on their activity with some subclasses showing little or no reduction in their activities while there is a significant reduction in activity in some other sub-classes suggesting varying roles for the aspartic acid in different dye-decolourising peroxidases (Sugano et al., 2007, Liu et al., 2011, Pfanzagl et al., 2018). From the structural analysis of the DypB from *Rhodococcus jostii*, the presence of the channel through which the H_2O_2 gets access to the haemoglobin centre at the active site. Residues along the channel may also provide the site of binding for the Mn^{2+} to transfer electron to the haemoglobin centre (Singh et al., 2012).

Figure 5. Multiple structural alignment of some dye-decolourising peroxidases
Three previously deposited structures in the Protein database (PDB) were aligned with the dye-decolourising peroxidase from *Bacteriodes thetaiotaomicron* VPI-5482 (BtDyp). The three proteins share varying percentages of primary sequence identity with BtDyp. BtDyp is represented by the yellow colour while the proteins being compared against it are represented by the other colours. The three proteins, PDB identities, their percentage sequence identities, and the resolution of their crystal structures are: - (A) DypB D153A variant in complex with haem from *Rhodococcus jostii* RHA1, 3VEC, 48.04%, 2.6 Å; (B) Dye-decolourising peroxidase from *Klebsiella pneumoniae*, 6FKS, 34.01%, 1.6 Å; (C) Dyp-type peroxidase from *Thermobifida fusca*, 5FW4, 21.59%, 1.8 Å. Despite the major disparity in primary sequences, there is high structural alignment of the secondary structure elements (α-helices and β-sheets for all four peroxidases. The alignments were done using the PyMol software. (Singh et al., 2012, Zubieta et al., 2007, Rahmanpour et al., 2016, Pfanzagl et al., 2018, Schrodinger, 2015)

Laccases are phenol oxidases belonging to the multi-copper oxidase superfamily. The first laccase discovered was in the latex of the Japanese lacquer tree, *Rhus vernicifera*.(Yoshida, 1883). Laccases have since been discovered in filamentous fungi, bacteria, plants and insects (Giardina et al., 2010, Baldrian, 2006, Dwivedi et al., 2011). Laccases represent the largest subgroup of the multi-copper oxidase (MCO) superfamily, a family that uses the distinctive redox ability of copper ions to catalyse the oxidation of a wide range of aromatic substrates while simultaneously reducing molecular oxygen to water. (Solomon, Sundaram and Machonkin, 1996). Other members of the multi-copper oxidase superfamily include ascorbate oxidase, ferroxidase nitrite reductase and ceruloplasmin (Reiss et al., 2013). Laccases are usually glycosylated with an isoelectric point around pH 4.0, and can either exist in monomeric or polymeric forms. (Sigoillot et al., 2012). Glycosylation in laccases is believed to be responsible for proteolytic susceptibility, copper retention, activity, thermal stability and its secretion.(Madhavi and Lele, 2009). Multiple sequence alignments of more than 100 laccases has led to the identification of a set of four ungapped sequence regions, L1 – L4, useful for distinguishing laccases from the other multicopper oxidases (Kumar et al., 2003). A total of 10 histidines and 1 cysteine are conserved across all multi-copper oxidases and are thought to serve as the copper ligands (Kumar et al., 2003)

Although laccases were the first ligninolytic enzymes to be investigated, the first molecular structure of a complete fungal laccase was published only in 2002 when the crystal structures of the laccases from the basidiomycete *Trametes versicolor*, and the ascomycete *Melanocarpus albomyces* (Figure 6) were reported (Martinez et al., 2005).

Figure 6. The crystal structure of Melanocarpus albomyces laccase. Taken from(Hakulinen et al., 2002).

The figure shows the crystal structure of the laccase from Melanocarpus albomyces, one of the very first laccase structures solved. The structure includes four copper ions at the active site of the laccase and the high level of glycosylation of the enzyme is also captured in this structure. Four copper ions (Cu^{2+}) is the full complement of copper necessary for the complete reduction of oxygen to water at the laccase's active site

The structure of laccases is organized into three domains made up of β-sheets, which are strongly associated and envelope the copper centres (Sigoillot et al., 2012). The active site of laccases is highly conserved and is made up of four copper atoms held at two sites, a type-1 (T1) mononuclear copper centre and a tri-nuclear copper cluster consisting of one type-2 (T2) mononuclear copper centre and a coupled binuclear type-3 (T3) copper centre (Claus, 2004). In the resting state of the enzyme , all four coppers are in the Cu^{2+} oxidation state (Wong, 2009). The four copper atoms all show characteristic electronic paramagnetic resonance patterns (Sigoillot et al., 2012). The T1 Cu exhibits a planar triangular coordination with the sulphur atom of a cysteine and with the Nδ1 nitrogen of two histidines (Giardina et al., 2010). This coordination is responsible for substrate oxidation and for the redox potential of laccases (Sigoillot et al., 2012). The charge-transfer transitions from Cys-S to Cu (II) at the T1 centre

of the laccases is responsible for a very intense absorption band with a molar absorption coefficient (ε) of 5,300 M^{-1} cm^{-1} at 614nm (Lee et al., 2002). The absorption band gives laccases their characteristic blue colour (Giardina et al., 2010).

The catalytic cycle of laccases involves four one electron oxidations of a reducing substrate with a concomitant two electron reduction of dioxygen to water (Wong, 2009). The catalytic cycle is believed to take place in three reaction steps (Figure 7). First, the type 1 Cu (the primary electron acceptor) is reduced by a reducing substrate (HuangZoppellaro and Sakurai, 1999) The electrons abstracted from the reducing substrate at the type 1 Cu centre are then transferred to the type 2 and type 3 Cu tri-nuclear cluster via a His–Cys–His tripeptide pathway converting the resting form of the enzyme to a fully reduced state (Wong, 2009, Piontek, Antorini and Choinowski, 2002a). Finally, O_2 reduction to water takes place at the tri-nuclear cluster and the enzyme is converted back to its initial resting fully oxidized state (Gianfreda, Xu and Bollag, 1999). The intramolecular electron transfer from the T1 Cu, and the diffusion of O_2 to the tri-nuclear cluster are the two rate limiting steps in the catalytic cycle (Wong, 2009).

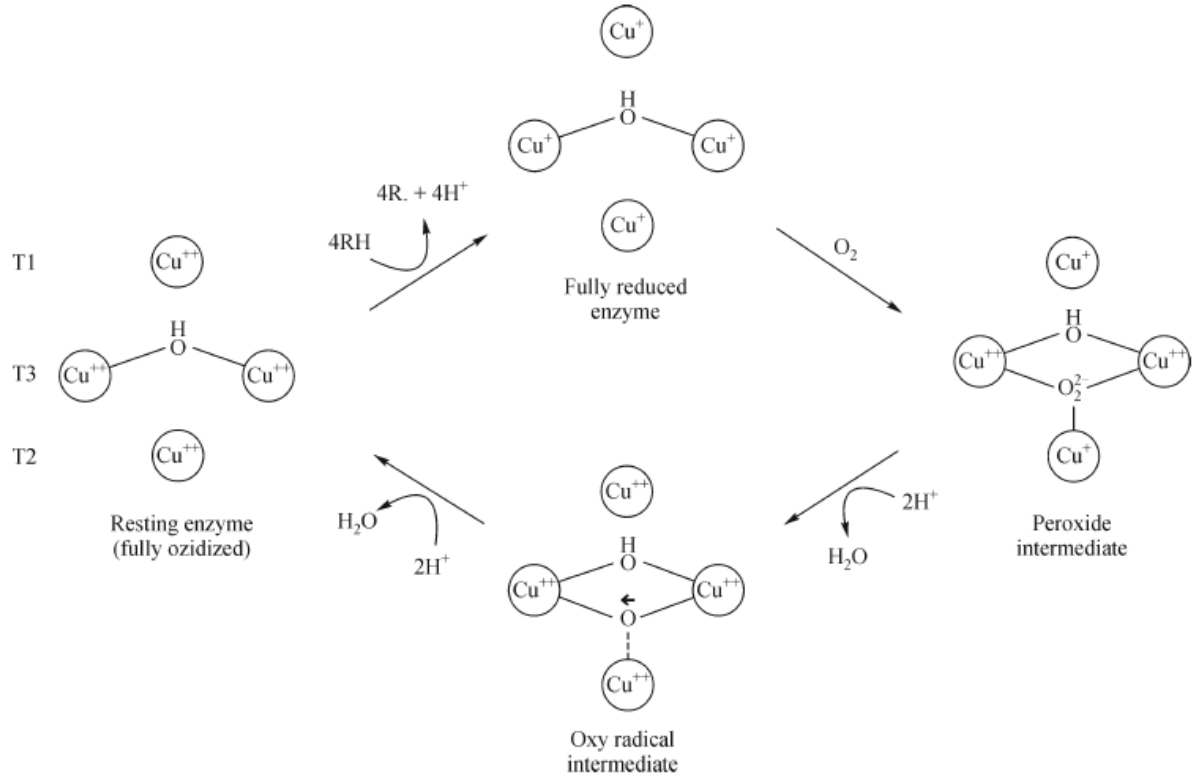

Figure 7. Catalytic cycle of laccases

The figure above shows the changes that take place at the active site of laccases during its oxidation of the substrate it encounters, its conversion from a fully oxidised state when all four Cu atoms are in the +2 state through a fully reduced state (all Cu atoms are in the +1 state), through the formation of the intermediate peroxide and oxy radical stages before going back to its resting state where the process can then repeat itself again when it comes in contact with a new substrate molecule. All these processes result in the oxidation of the substrate and the reduction of the oxygen to two molecules of water (Wong, 2009).

Laccases can be classified into three groups based on the redox potential of their type 1 Cu centre. It could be low (0.4 - 0.5 V), medium (0.5 – 0.6 V) and high (0.7 – 0.8 V) (Xu et al., 1996). The substrate oxidized by laccases encompasses a whole range of substances including aromatic compounds, inorganic/organic metal complexes, ferrocyanide and a whole range of organic, inorganic and biological compounds as long as they have a low redox potential (Gianfreda et al., 1999) Laccases can directly oxidize only the phenolic units of lignin, which compose just about 10% of the lignin polymer (Martinez et al., 2005) They are also able to oxidize phenolic lignin model compounds like vanillyl glycol and syringaldehyde to form phenoxy radicals (Wong, 2009). The formation of phenoxy radicals leads to C_α - C_β cleavage, C_α oxidation, alkyl – aryl cleavage and aromatic ring cleavage (Kawai et al., 1988).

The discovery that *Pycnoporus cinnabarinus,* a white rot fungi that produces laccases only is able to degrade non-phenolic compounds of lignin in the natural lead to the discovery of mediators (Eggert et al., 1996). Mediators are compounds that enable laccases to directly oxidize non-phenolic portion of kraft lignin as well as non-phenolic lignin model compounds (Bourbonnais and Paice, 1990). The rate of oxidation by the laccase/mediator system depends on the K_{cat} of the laccase for the mediator and the stability of the enzyme to inactivation by the free radical of the mediator (Li, Xu and Eriksson, 1999). More than 100 different compounds including ABTS have been used as mediators but the most effective mediators for lignin degradation so far have been the N-heterocycle-bearing N-OH group of compounds with an example being 1-hydroxybenzotriazole (HBT) (Giardina et al., 2010). Laccases are of biotechnological interest because of their stability over a wide range of temperature and pH conditions and also their ability to oxidize high redox potential substrates in the presence of synthetic mediators (Sigoillot et al., 2012).

The β-O-4 bond in lignin makes up about half of the ether bonds that are present within the various types of technical lignin and usually require at least three enzymatic steps to break this bond down in the dimeric β-ether lignin model compound, GGE (1-(4-hydroxy-3-methoxyphenyl)-2-(2-methoxyphenoxy)propane-1,3-diol) (Rosini et al., 2016). The multiple enzyme catalysed steps involve alcohol dehydrogenases from *Sphingobium sp.* strain SYK-6 such as LigD, LigO, LigN and LigL (Figure 8) that catalyse the conversion of GGE to MPHPV (α-2-methoxyphenoxy)-β-hydroxypropiovanillone) (Sato et al., 2009) then the MPHPV is attacked by multiple enantioselective glutathione-S-transferases such as LigE, LigF and LigP that convert the MPHPV to GS-HPV (α-glutathionyl-β-hydroxypropiovanillone) and guaiacol while another glutathione-S-transferase, LigG catalyses some epimers of LigE, F and P attack (Gall et al., 2014, Higuchi et al., 2018). The minimum number of enzymes that would be capable of completely degrading the β-ether

bonds in the lignin model compound GGE was determined to be LigD, LigN, LigE and LigF together with *Novosphingobium aromaticivorans* glutathione-S-transferase, $NaGST_{NU}$ which catalyses the reduced glutathione dependent of the GS-HPV epimers to HPV and oxidised glutathione, and AvGR which catalyses the NADH-dependent reduction of oxidised glutathione to enable a recycling of NAD^+ and reduced glutathione, essential co-factors in the lignin degradation process (Gall et al., 2018, Kontur et al., 2018).

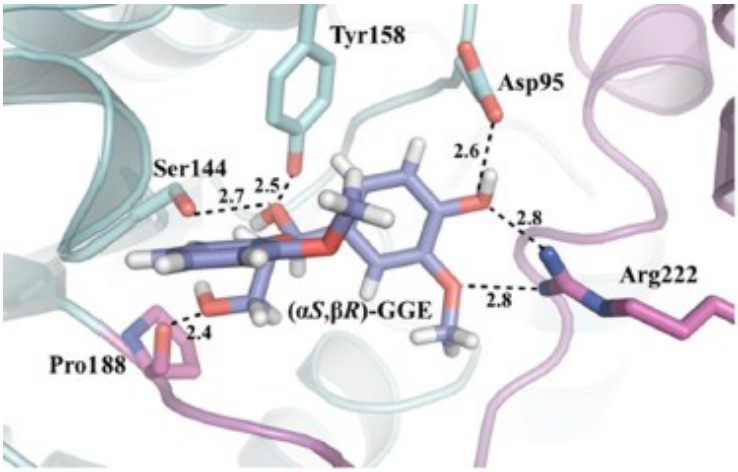

Figure 8. LigL bound to the lignin model compound, (αS,βR)-GGE

The figure was taken from (Pereira et al., 2016).This shows the different residues, Pro^{188}, Arg^{222}, Asp^{95}, Tyr^{158} and Ser^{144} that have a direct interaction with the GGE molecule unlike in some other lignin degrading enzyme classes where there is no direct connection between enzyme and substrate molecule.

Other extracellular enzymes involved in lignin degradation are aryl-alcohol oxidase, glyoxal oxidase, aryl-alcohol dehydrogenase, quinone reductase and cellobiose dehydrogenase (Martínez et al., 2005).

1.4 Lignin Degradation Products

Lignin, due to its aromatic structure could potentially be a source of a whole range of useful chemical compounds upon its degradation. Potential products of lignin degradation are aromatic bio-products that would be valuable raw materials for the synthesis of fine chemicals for use in the food and flavour industry (Bugg et al., 2011). Chemicals such as

phenols, vanillin, syringaldehyde and aliphatic compounds could potentially be obtained as a result of lignin degradation (MacfarlaneMai and Kadla, 2014). Achieving selectivity in transforming lignin into useful industrial chemicals is the major challenge facing lignin utility in the bio-refinery (Bozell, 2014).

1.5 Aims and objectives

The purpose of this study is to identify lignin degrading enzymes from bacteria and fungi, determine the optimum expression and solubility conditions of these enzymes, characterise the expressed enzymes and the processes they perform and determine the structure of these enzymes using x-ray crystallography. Degradation of Kraft lignin will be carried out using the *Panus rudis* laccase in combination with acetosyringone, HBT and guaiacol. Scanning electron microscopy (SEM), Fourier transform infrared (FTIR) spectroscopy combined with principal component analysis and Electrospray ionisation Fourier transform ion cyclotron resonance spectroscopy will be used to monitor the degradation process and analyse the lignin degradation products. Purification of the dye-decolourising peroxidases using different chromatography techniques such as ion exchange and gel filtration chromatography will be done as well.

Chapter 2: Materials & Methods

2.1 Materials Used in This Study

The plasmid pET-28b (+) (Novagen) obtained from Dr Jon Marles-Wright was used in several cloning experiments. Plasmid pET-28a (+) (Novagen) was also utilized in the course of this Ph.D. They both have T7 promoter, a lac operator, low copy PBR322 origin of replication, kanamycin resistance and N and C-terminal histidine tags (pET User Manual, 2011). The plasmid pPicZαA was used in the transformation of the fungal enzymes.

E.coli strains BL21-AI, DH5α, JM109, B834 and Top 10 competent cells were purchased from Invitrogen. BL21 (DE3) and Q5 polymerase site directed mutagenesis kit were purchased from New England Biolabs (NEB). The *Pichia pastoris* strain X-33 (Invitrogen) was used in expressing the fungal enzymes.

Immobilized Metal Affinity Column (IMAC) Hi Trap FF 1 ml, Q sepharose FF 1ml, SP sepharose FF 1ml, Resource Q, Resource S and Superdex 200 16/60 columns (GE Healthcare) were all utilized in this study. Pre-cast SDS-PAGE gels were purchased from Novex. Kraft lignin (alkali) was purchased from Sigma Aldrich.

2.2 Buffers and Media Used

All buffers were sterilized before use.

- **Loading Buffer for Ion Exchange Chromatography of BsDyp**
  20 mM Tris-HCl buffer. pH was adjusted to pH 7.6 with 1 M HCl.
- **Lysis Buffer for Ion Exchange Chromatography of BsDyp**
  Loading buffer plus EDTA-free protease inhibitor cocktail tablets (1 tablet for every gram of bacterial cells).
- **Elution Buffer for Ion Exchange Chromatography of BsDyp**
  20 mM Tris-HCl and 1 M NaCl, pH 7.6.

- **Loading Buffer for Ion Exchange Chromatography of PpDyp**

  20 mM Bis Tris-HCl buffer, pH 6.0.

- **Lysis Buffer for Ion Exchange Chromatography of PpDyp**

  Loading buffer plus EDTA-free protease inhibitor cocktail tablets (1 tablet for every gram of bacterial cells).

- **YPD medium/plates**

  10 g yeast extract and 20 g peptone were dissolved in 900 ml water. Autoclave for 20 min. Allow to cool before adding 2% glucose to make a 1 L final volume. To make YPD plates, 20 g agar is added to final mixture.

- **BMGY and BMMY medium**

  10g yeast extract and 20 g peptone were dissolved in 700 ml water. Autoclave for 20 min. Allow to cool before adding 100 ml of 1 M potassium phosphate buffer, pH 6.0, 1.34% Yeast Nitrogen Base, 4 x 10^{-5}% biotin and 1% glycerol for BMGY or 0.5% methanol for BMMY to make a 1 L final volume.

2.3 Methodology

2.3.1 *Bacillus subtilis* (BsDyp) and *Pseudomonas putida* MET94 (PpDyp) dye-decolorizing peroxidases

2.3.1.1 Cloning and overexpression of full length PpDyp and BsDyp in *Escherichia coli* (Santos et al., 2014)

This experiment was performed by Professor Ligia Martin's group and the protocol has been reported as described in Santos et al., 2014. Genomic DNA of *P. putida* MET94 (NCIMB 14727) and *B. subtilis* 168 (NCIMB 10106) were obtained by centrifuging 200 µL of fresh cell cultures for 1 min at 13,000 rpm. Pellets were washed twice, suspended in 50 µL of Milli Q water, boiled for 5 min, and the chromosomal DNA applied as a template for gene-specific

primed PCR amplification. The PpDyP (PP_3248 gene; accession number, NC_002947.3) and BsDyP (BSU38260 gene; accession number, NC_000964.3) were amplified using the primers DypPpF (5′GGATTAGCCT**CA′T**<u>**ATG**</u>CCGTTCCAGCAAGG3′) and DypPpR (5′GTGTTTCTGTATCT**G′GATCC**TTAGAGATCAGGCCCGC3′), for PpDyp and the primers DypBsF (5′GGAGTTTTGTAAC**CA′T**<u>**ATG**</u>AGCGATGAACAGAAAAAGCC3′) and DypBsR (5′CGCTGAAA**G′GATCC**TGTAAAGGCTTCTTTTATGATTCC3′) for BsDyp. Nucleotides for restriction sites of NdeI and BamHI are given in bold and the start codons are underlined. The PCR products were digested with NdeI and BamHI and inserted between the respective restriction sites of plasmid pET-21a (+) to yield plasmids pRC-1 and pRC-2, respectively. These were transformed into the host expression strains *E. coli* BL21 (DE3, Novagen) and *E. coli* BL21 star (DE3, Novagen), respectively, in which the target genes were expressed under the control of the T7 *lac* promoter. The recombinant strains were grown in LB medium supplemented with ampicillin (100 μg mL^{-1}) at 37 °C. Growth was followed up to an OD_{600} of 0.6 and at that point 100 μM isopropyl-β-D-thiogalactopyranoside and 15 μM hemin were added to the culture medium, the temperature was lowered to 25 °C, and the incubation continued overnight. Cells were harvested by centrifugation (8,000 ×g, 10 min, 4 °C) after 24 h of growth. (Santos et al., 2014)

2.3.1.2 Purification of recombinant full length PpDyP and BsDyP (Santos et al., 2014)

This experiment was also performed by members of Professor Ligia Martins' group and has been described as in Santos et al., 2014. Cell pellets were suspended in 20 mM Tris–HCl buffer, pH 7.6, containing DNase I (10 μg mL^{-1} extract), $MgCl_2$ (5 mM), and a mixture of protease inhibitors, antipain, and leupeptin (2 μg mL^{-1} extract). Cells were disrupted in a French press. Cell debris was removed by centrifugation (18,000 × g, 2 h, 4 °C) and crude extracts were used for protein purification in an ÅKTA purifier (GE Healthcare, Bio-

Sciences, Uppsala, Sweden) at room temperature. For purification of PpDyP, the crude extract was loaded onto a 1 ml Q Sepharose FF column equilibrated with 20 mM Tris–HCl buffer, pH 7.6. Elution was carried out with 1 M NaCl in buffer. The active fractions were pooled and concentrated before applying on a Superdex 200 HR 16/60 column (GE Healthcare, Bio-Sciences) equilibrated with 20 mM Tris–HCl buffer, pH 7.6 with 0.2 M NaCl. The purified protein was stored at -20 °C until it was used. For purification of BsDyP, the crude extract was loaded onto a SP-Sepharose FF column (GE Healthcare) equilibrated with 20 mM Tris–HCl buffer, pH 7.6. Elution was carried out with 1 M NaCl in buffer. The active fractions were pooled, dialyzed to 20 mM Tris–HCl (pH 7.6), and applied to a Mono-STM 5/50(GE Healthcare, Bio-Sciences). Active fractions were pooled and concentrated before being applied onto a Superdex 75 HR16/60 column (GE Healthcare, Bio-Sciences) equilibrated with 20 mM Tris–HCl buffer, pH 7.6, with 0.2 M NaCl. The purified protein was stored at -20 °C until it was used. (Santos et al., 2014). The purified protein was then transported to me for structure determination

2.3.1.3 Cloning and overexpression of truncated BsDyp in *E.coli*

To obtain better crystals after failure of initial crystallisation trials, I excised some of the positively charged amino acids at the N-terminal of the full length BsDyp using PCR. The primers, forward (5'-GA**CCCATG**GAGCAGATTGTTCCGTTTTAC-3') and reverse (5'-GTA**CTCGAG**TGATTCCAGCAAACGCTGGG-3') were used for sub-cloning truncated versions of BsDyp with no His-tags and His_6 tags respectively. The full length BsDyp from Section 2.6.1 was used as a template and it was designed with the restriction sites for the enzymes NcoI and XhoI sites (in bold) and the two versions of the truncated BsDyp were inserted into the NcoI and XhoI sites of pET-28a (+). The resulting plasmids were then inserted into the expression hosts BL21 (DE3, Novagen) and BL21- AI, in which the target

genes were expressed under the control of the T7 *lac* promoter and both the T7 *lac* promoter and P_{BAD} promoters respectively. The recombinant strains were grown in LB medium supplemented with kanamycin (50 μg mL^{-1}) at 37 °C. Growth was followed up to an OD_{600} of 0.6 and at that point 100 μM IPTG, 0.2 % arabinose and 15 μM hemin were added to the culture medium, the temperature was lowered to 20 °C, and the incubation continued for another 48 hours. Cells were harvested by centrifugation (4,500 × g, 30 min, 4 °C) after 48 h of growth.

2.3.1.4 Purification of truncated BsDyP

I suspended the cell sediments nin 20 mM Tris–HCl buffer, pH 7.6 containing EDTA-free protease inhibitor cocktail tablets (Roche). Cells were disrupted in a French press. Cell debris was removed by centrifugation (50,000 × g, 1 h, 4 °C) and crude extracts were used for protein purification in an ÅKTA purifier (GE Healthcare Life Sciences) at 4 ºC. The crude extract was loaded onto a SP-Sepharose FF column equilibrated with 20 mM Tris–HCl buffer, pH 7.6. Elution was carried out with 1 M NaCl in buffer. The active fractions were pooled, desalted and buffer exchanged using a Vivaspin 20 10 KDa MWCO at 5,000 x g for 30 minutes to 20 mM Tris–HCl (pH 7.6) and applied to a Resource S column (GE Healthcare Life Sciences). The sample was eluted with loading buffer containing 1 M NaCl. Active fractions were pooled and concentrated before being applied onto a Superdex 200 HR 16/60 column (GE Healthcare Life Sciences) equilibrated with 20 mM Tris–HCl buffer, pH 7.6, with 0.2 M NaCl. The purified protein was flash frozen using liquid nitrogen and stored at -80 °C until further use.

2.3.1.5 Selenomethionine labelling of PpDyp [Adapted from (van den Ent et al., 1999)]

I added a single colony of freshly transformed PpDyp in BL21 Tuner™ (DE3) (Novagen) to M9 media containing 0.4% glucose, 2 mM $MgSO_4$ and 50 μg mL^{-1} ampicillin at 37 ºC

overnight. The overnight culture was then sub-cultured at 1:50 into 1 L M9 media containing 0.4% glucose, 2 mM $MgSO_4$, 50 μg mL^{-1} ampicillin, 1/100 trace elements. After 4-5 h at 20 ºC incubation, 100 mg L-selenomethionine, 100 mg L-lysine, 100 mg L-threonine, 100 mg L-phenylalanine, 50 mg L-leucine, 50 mg L-isoleucine and 50 mg L-valine and 15 μM hemin was added to the culture. The culture was then allowed to grow for 48 h at 20 ºC. Cells were harvested by centrifugation (4,500 × g, 30 min, 4 °C), the pellets were flash frozen in liquid nitrogen and stored at -80 ºC. The waste generated from harvesting the Se-Met labelled cells is toxic and was disposed of carefully.

2.3.1.6 Purification of the Selenomethionine labelled PpDyp

I re-suspended Se-Met labelled, Ppdyp containing, BL21 Tuner™ (DE3) (Novagen) cell pellets in 10% 20 mM Bis Tris–HCl buffer, pH 6.0 containing EDTA-free protease inhibitor cocktail tablets (Roche). The suspension of cells was mixed thoroughly until there were no solid particulates left and applied to a French press set at 25 kilopound per square inch (kPSI). Two passes through the French press were needed to completely lyse the cell pellets. Cell debris was removed from the cell extracts by centrifugation (50,000 × g, 1 h, 4 °C) and the crude extracts were used for protein purification in an ÅKTA purifier (GE Healthcare Life Sciences) at 4 ºC. Anion exchange chromatography (AEC) was the first step in the purification. The crude extract was loaded onto a 10 ml Q-Sepharose™ Fast Flow column equilibrated with 20 mM Bis Tris–HCl buffer, pH 6.0. Elution was carried out with 20 column volumes of 1 M NaCl in loading buffer. The fractions containing PpDyp as determined from the purification trace, were pooled, desalted and buffer exchanged using a Vivaspin 20, 10 KDa MWCO centrifugal filter (GE Healthcare) at 5,000 x g for 30 min to a final volume of 20 ml in 20 mM Bis Tris–HCl, pH 6.0 before being applied to a Resource Q column (GE Healthcare Life Sciences). The sample was eluted with 20 column volumes of

loading buffer containing 1 M NaCl. Eluents containing PpDyp, as determined from purification chromatogram were pooled and concentrated before being applied onto a Superdex 200 HR 16/60 column (GE Healthcare Life Sciences) equilibrated with 20 mM Bis Tris–HCl buffer, pH 7.6, with 0.2 M NaCl and a size exclusion chromatography (SEC) was carried out. The purified protein was flash frozen using liquid nitrogen and stored at -80 °C until further use.

2.3.2 Crystallisation, X-ray data collection and analysis of BsDyp and PpDyp

2.3.2.1 Crystallisation, screening and optimisation of BsDyp and PpDyp

I adjusted the concentrations of the purified fractions of BsDyp and PpDyp proteins previously purified by IMAC or ion exchange chromatography followed by SEC to 10 mg/ml using 1 M Tris for crystallisation trials. Both proteins and their various modified forms were screened using five different commercial protein crystallisation screens: - Index HT (Hampton Research), Structure 1 & 2 HT-96 (Molecular Dimensions), PEG/Ion HT (Hampton Research), JCSG plus HT-96 (Molecular Dimensions) and MIDAS (Molecular Dimensions). The Gryphon nanolitre pipetting robot (Art Robbins) was used to dispense 65 µl of each crystallisation screen into a 96-well standard polystyrene crystallisation plate (MRC). 0.1 µl reservoir solution was dispensed into both crystallisation wells for a specific screen's condition followed by 0.1 and 0.2 µl of BsDyp and PpDyp being dispensed into the top and bottom crystallisation wells by the nanodispenser respectively. When all the crystallisation wells had been filled for a particular plate, the plate was sealed by an X-Seal Manual Adhesive Sealer XCS-384 (FluidX) using transparent, self-adhesive polyolefin film. The plates were incubated at 18 ^{o}C. This setup of having the drops of protein and the screen on the bottom of the wells of the crystallisation well is known as the sitting-drop vapour-diffusion method (Rupp, 2010). The crystallisation plates were checked over the following

week for crystal formation using a M205 C stereo microscope (Leica Microsystems), and the best protein-screen combination ratio (hits) were digitally recorded using the Leica Application Suite (LAS) software. The hit conditions were optimised in Linbro 24-well plates. In these optimisation plates, the well solutions were set up to a final volume of 1 ml. The optimisation crystallisation drops were set up using the hanging drop vapour diffusion method. The drops were set up on glass coverslips in varying ratios of protein to well solution as follows: - 1 µl: 1 µl, 1 µl: 2µl and 2µl: 1µl. Vacuum grease (Corning) was applied to the edges of the coverslips before attaching them to the 24-well plates thus sealing up the wells. The plates were incubated at 18 ^{o}C and observed for crystal growth over the next few days to a week. The plates could be stored at this temperature for up to two months. Observed crystals over this period were harvested from both the 96, and 24 well plates using a LithoLoop (Molecular Dimensions), moved briefly to a cryo-protectant solution, comprising well solution and 20% v/v PEG 200 or 20% glycerol. The crystal was subsequently flash cooled in liquid nitrogen and transferred to uni-pucs for data collection at the Diamond Light Source (Didcot, UK).

2.3.2.2 X-ray diffraction data collection and its processing

I collected the crystallographic datasets for this project on the various macromolecular crystallography beamlines at the Diamond Light Source (Didcot, UK) at 100 K using Pilatus 6M detectors. The raw diffraction data collected were integrated and scaled using XDS (Kabsch, 2010). The crystallographic point and space groups were determined by CCP4 programmes *POINTLESS* and *CTRUNCATE* followed by a merging of their symmetry related reflections with *AIMLESS* (Evans, 2011, Evans and Murshudov, 2013). The structure determination and refinement was determined based on the resolution cut-off criteria as

follows: completeness (> 95%), I/sig I (> 1.5) and $CC_{1/2}$ (> 0.5) (Karplus and Diederichs, 2012).

2.3.2.3 Model building and refinement of crystals

The BsDyp data was initially phased by molecular replacement, using the dye-decolourising type peroxidase from *Thermobifida fusca* (PDB ID: 5fw4) as a search model. The search model's sequence was modified to match that of BsDyp's using *CHAINSAW* (Stein, 2008). An initial solution to the phase problem was sought by molecular replacement using Phaser MR (McCoy et al., 2007). The resulting solution from Phaser was used to rebuild the BsDyp model using *phenix.autobuild* (Adams et al., 2010). Multiple refinement iterations of automated refinement with *phenix.refine* (Afonine et al., 2012) and manual rebuilding and inspection of the model was done in *Coot* at various stages of the refinement to verify accuracy of the refinement process (Emsley and Cowtan, 2004). Every refinement iteration in *phenix.refine* included ten macrocycles of coordinate refinement, bulk solvent correction, anisotropic scaling, occupancy refinement and individual B-factors. Several refinement target weights including the following scale factors: X-ray/stereochemistry weight (wxc_scale) as 0.5; X-ray/ADP weight (wxu_scale) as 1.0; stereochemistry weight scale (wc) as 1.0; ADP weight scale (wu) as 1.0, were used. The refinement regime is ideally repeated on the model for several cycles until the R_{work}, R_{free} and stereochemical restraints have reached convergence. To complete the refinement, water molecules and hydrogen atoms were added automatically to the model in *Phenix*, while the model was further inspected in Coot manually (Emsley, 2017).

2.3.2.4 BsDyp crystallographic model analysis

The BsDyp crystallographic model was validated using the freely available programme, *MolProbity* (Davis et al., 2007, Chen et al., 2010b). *Coot* was used to calculate the structural

superimpositions (Emsley et al., 2010), by running the secondary-structure matching (SSM) algorithm (Krissinel and Henrick, 2004). The PDBePISA server was used to calculate the various protein interface interactions, and the crystallographic figures were generated using PyMOL (Krissinel and Henrick, 2007, Schrodinger, 2015).

2.3.3 Cloning and Expression of *Panus rudis* laccase in *Pichia pastoris*

2.3.3.1 Bioinformatics analysis

The gene for the *Panus rudis* laccase was synthesized and codon optimized for expression in *P. pastoris*. The gene sequence was put through BLAST for conserved domain identification (Altschul et al., 1990). Signal P 4.1 was used for detection of signal sequences (Petersen et al., 2011). Genscript rare codon analysis tool (https://www.genscript.com/tools/rare-codon-analysis) was used for codon usage analysis and Protparam (Gasteiger et al., 2003) used to identify properties of these enzyme (Done by Dr Takanori Furukawa).

2.3.3.2 Expression of *Panus rudis* laccase

The codon optimized sequence of *Panus rudis* laccase was cloned into *Pichia pastoris* by Dr. Takanori Furukawa. The colonies of the enzymes were inoculated into 100 ml of BMGY in a 500 ml flask at 30 °C, 220 rpm overnight to serve as a pre-culture. The cultures were collected and centrifuged at 1500 x g, 4 °C for 5 min. The cells were re-suspended into YPD media (5 ml). The resulting culture was inoculated into 500 ml of BMGY to an OD_{600} of 1.0 in a 2 L flask and incubated at 20 °C, 220 rpm, for several days with samples collected each day to test for expression and enzyme activity. The collected fractions were centrifuged at 1500 x g, 4 °C for 5 min. The supernatant was collected and filtered through a 0.2 µm filter unit and kept at 4 °C until use.

2.3.3.3 Enzyme activity of *Panus rudis* laccase

I tested the degrading ability of the fungal lignin degrading enzymes on solid plates and in solution. Plate assays using the five different substrates: ABTS, 2, 6-dimethoxyphenol (DMP), sinapic acid, syringaldehyde and acetosyringone, was done with varying concentrations of the enzymes on YPD agar plates at pH 3.0 and 5.0. The plates were left for 30 min after application of the laccase for colour development. For the solution assays, 250 µl of 0.2 M sodium tartrate buffer pH 3.0 and pH 5.0, 600 µl distilled water, 50 µl 10 mM ABTS and varying quantities of crude extracts of *Panus rudis* laccase were mixed together in solution. Absorbance was measured at 420 nm for 1 min to determine activity of the laccase. The optimum temperature and pH for *Panus rudis* laccase reaction with ABTS was also determined at pH 3.0.

2.3.4 Modification of Kraft Lignin by *Panus rudis* laccase

The experiments were carried out in 100 ml Erlenmeyer flasks that had been heated to 450 °C to remove all organic material and then autoclaved. The composition of the reaction mixtures is shown in the table below. Appropriate controls (lignin only, lignin and mediator, laccase only, lignin and laccase) were also set up in the same way, with the absent components in the controls being substituted with water.

Table 4: Composition of the reaction mixtures

	Final concentration	**need**
Kraft Lignin (50 g/L)	5 g/l	3.5 ml
Mediator (1 M)	200 µM	7 µl
200 mM ammonium acetate buffer pH = 4.0	20 mM	3.5 ml
Laccase	200 µM/min	355 µl
Distilled Water (Varying amounts)		
Total		35 ml

Mediators used were acetosyringone, guaiacol and HBT

15 ml of each reaction mixture was taken immediately (t = 0) and freeze-dried. The flasks containing the remaining reaction mixtures were sealed with a sponge bung and aluminium foil and the reaction allowed to progress at 20 °C and 200 rpm in an Infors HT Multitron Standard Shaker for one week.

2.3.5 Freeze Drying of Reaction Mixtures

15 ml of each sample was aliquoted into Thermo Scientific 40 ml glass vials with screw caps. The samples were frozen at -20 °C and then transferred to the -80 °C freezer overnight for further freezing. The frozen samples were finally freeze dried for 48 hours using a Lablyo mini freeze drier, until the samples were totally dry. The freeze-dried samples were then stored at room temperature for further assays.

2.3.6 Scanning Electron Microscopy

Small quantities of sample were mounted on a pin mount made of aluminium by using a self-adhesive carbon disc (C249/N 12 mm, TAAB Laboratories Equipment Ltd). Samples were then fixed to the mount using a jet duster (FALCON Dust-Off Plus) and coated with a gold/palladium mix using a sputter coater (model EMSCOPE SC500A). Analysis was performed using a Hitachi S4700 II cold Field-emission Scanning Electron Microscope, equipped with a Gatan Alto cryo-preparation system for high-resolution, low-temperature scanning electron microscopy and also a Yttrium Aluminium Garnet scintillator back-scattered electron detector capable of imaging 5 nm immunogold labels. The scans were done at multiple magnifications (x100 – x2500).

2.3.7 Infrared Spectroscopy Measurements

Attenuated total reflection Fourier transform infrared spectroscopy (ATR-FTIR spectroscopy) was performed using a PerkinElmer Spectrum 65 spectrometer with a Pike Technologies

diamond MIRacle ATR device. After recording spectra in the region from 4000 cm^{-1} to 600 cm^{-1} with a spectral resolution of 4 cm^{-1}, the spectra were processed by sequentially applying an ATR correction, a baseline correction and normalization of spectra to 50% transmittance at 1502 cm^{-1} (Kraft lignin) using the complementary PerkinElmer software. Two independent measurements were taken for each of the freeze-dried samples.

2.3.8 Electrospray Ionisation Fourier Transform Ion Cyclotron Resonance Mass Spectrometry (ESI FTICR-MS)

The samples were diluted in a 1:1 mixture of methanol and water to a final concentration of 0.1 mg/ml of reaction mix. The MS spectra measurements were carried out on a Bruker SolariX FT-ICR mass spectrometer (Bruker Daltonics, Bremen, Germany) with a 12 Tesla magnet using electrospray ionisation (ESI) as the ionisation method of choice. The nebulizer gas flow was set to 1.2 bar, drying gas was 6 L/min at 180 °C. Broadband spectra for each sample were collected over 200 summed scans between 150.0 m/z and 1000 m/z. The spectra were collected in negative-ion mode. Solvent blanks were included after every 6 samples and at the start and end of the experimental session. To prevent cross-contamination of consecutive sample readings, the syringe, capillary and sprayer were flushed with methanol: water before injecting the next sample onto the machine. The spectra obtained were recalibrated with a calibration list specific for Kraft lignin. Peaks that had a signal to noise ratio of more than 4 and surpassed a specific intensity threshold (2 million counts according to the spectrum) were selected and assigned by the software PetroOrg. A search criterion of 1 - 100 carbon atoms, 4 -200 hydrogen atoms, 1 - 30 oxygen atoms, 0 - 2 sulphur atoms, no nitrogen atoms and a maximum error of ± 0.5 ppm was chosen. The van Krevelen and DBE plots were plotted using python scripts from FTMS Vis Online (Kew et al., 2017a)

Chapter 3: Characterisation of *Panus rudis* laccase

3.1 Introduction

Panus rudis laccase (PrL) is a laccase secreted by the basidiomycetes, *Panus rudis*, as one of a number of lignin degrading enzymes that enables it to carry out its white rot decay of wood. PrL has a molecular weight of 58 KDa, an isoelectric point of 3.5 and is 8% glycosylated (Zhang et al., 2006). PrL has been shown to have the ability to decolourise several classes of dyes including the environmentally important anthraquinonic dyes such as Acid Green 27 (Zhang et al., 2006). Herein, I studied the ability of PrL to degrade Kraft lignin (Sigma-Aldrich) using various techniques and also examined some of the products produced from the degradation process. In the alignment in Figure 9, PrL shares all the 11 conserved residues (10 histidine residues and 1 cysteine residue) with the four other laccases it was aligned to. These 11 residues are important in coordinating the four Cu^{2+} ions present at positions T1, T2 and T3 at the active site of most laccases (Morozova et al., 2007). The residues corresponding to each position have been labelled with the appropriate position marker (T1, T2 or T3) on the alignment as well. It is important to note that even in RvL and MaL which have lower sequence identity to PrL, the 11 residues coordinating the Cu^{2+} are present showing how important they are to the activity of all laccases.

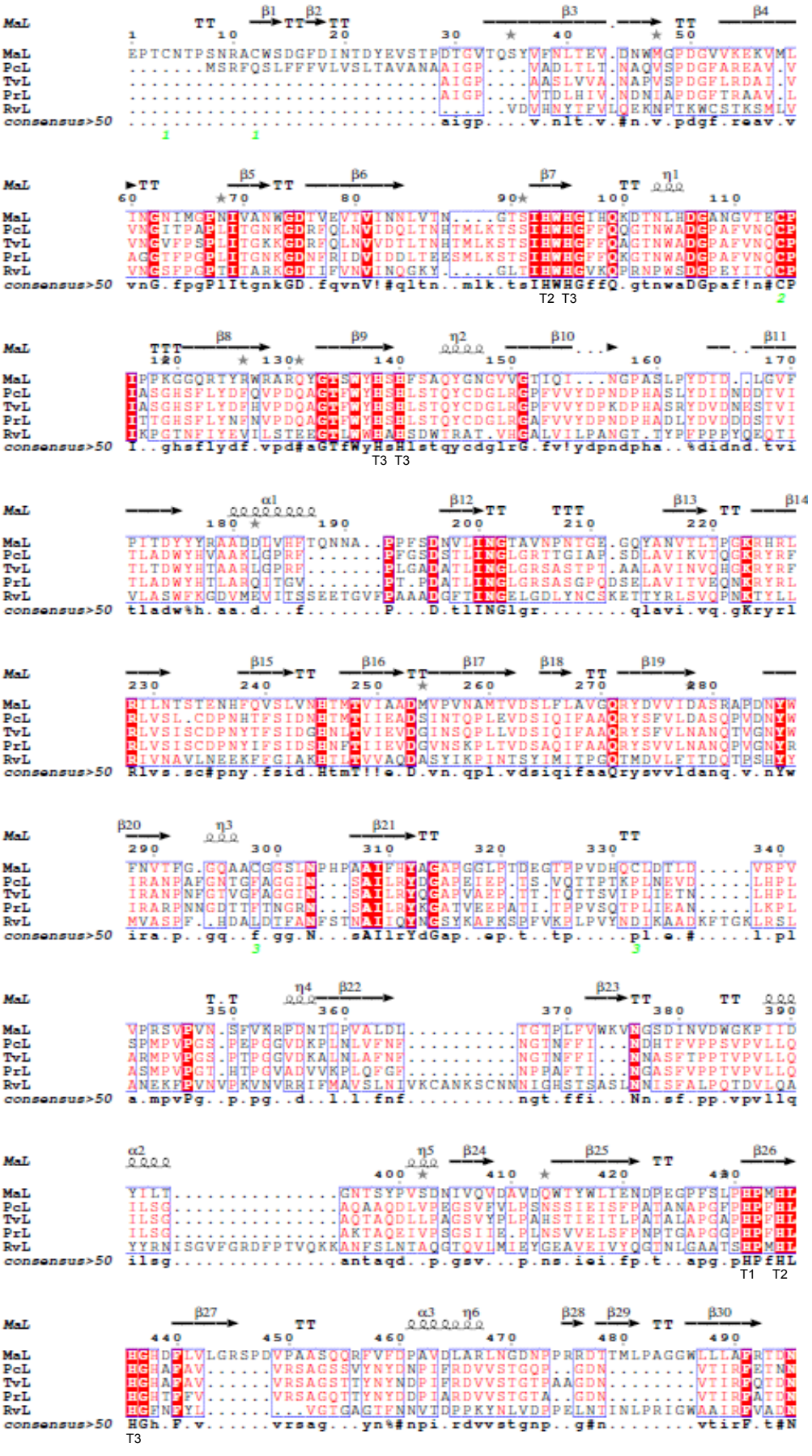

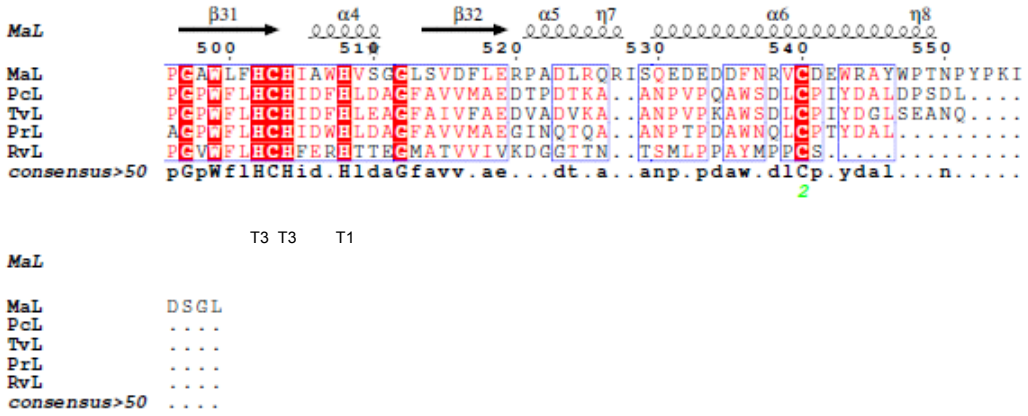

Figure 9. Multiple sequence alignment of *Panus rudis* laccase with four other laccases

Panus rudis laccase (PrL) was aligned with the fungal laccases from: - (a) *Melanocarpus albomyces* MaL, PDB ID: 2Q9O (Hakulinen et al., 2008); (b) *Pycnoporus cinnabarinus,* PcL (Otterbein et al., 2000); and (c) *Trametes versicolor*, TvL, PDB ID: 1GYC (PiontekAntorini and Choinowski, 2002b). The fourth laccase PrL was aligned with is the laccase from the Japanese lacquer tree, *Rhus vernicifera*, RvL (NittaKataoka and Sakurai, 2002). The alignment was done using Multalin and Clustal Omega (Corpet, 1988, Li et al., 2015) and the output displayed as an ESPript 3.0 file (Robert and Gouet, 2014). PrL's sequence identity to MaL is 32%, to PcL is 67%, to TvL is 70% and to RvL is 28% (Li et al., 2015). The output file shows consensus sequences in red boxes and shows the eight α-helices, thirty-two β-strands, eight 3_{10}-helices (η), twenty strict β-turns (TT) and two strict α-turns (TTT) present in MaL's secondary structure.

3.2 Cloning and expression of *Panus rudis* laccase

The cloning of the *Panus rudis* laccase was done by Dr Takanori Furukawa. The codon optimized DNA of the *Panus rudis* laccase was amplified by PCR. The PCR product was digested with restriction enzymes for cloning into a pPICZα-vector to add an alpha-factor (α-factor) secretion signal and the C-terminal tag-sequences (c-Myc and His_6 tags). A control construct was also made with no gene inserted. The vectors containing the appropriate gene insert were transformed into *P. pastoris* and this whole sequence of events is depicted in Figure 10. A resultant colony was used to inoculate into 100 ml of BMGY in a 500 ml flask at 30 °C, 220 rpm overnight to serve as a pre-culture. The cultures were collected and centrifuged at 1500 x g, 4 °C for 5 min. The cells were re-suspended in YP media (5 ml). The resulting culture was used to inoculate 500 ml of BMGY to an OD_{600} of 1.0 in a 2 L flask and incubated at 20 °C, 220 rpm for ten days. Samples were collected each day, centrifuged at 1500 x g and 4 °C for 5 min. The supernatants were collected and filtered through a 0.2 µm filter unit and kept at 4 °C until used to test for expression and activity of the laccase using ABTS. Figure 11 shows the time course of laccase expression as determined by ABTS assay.

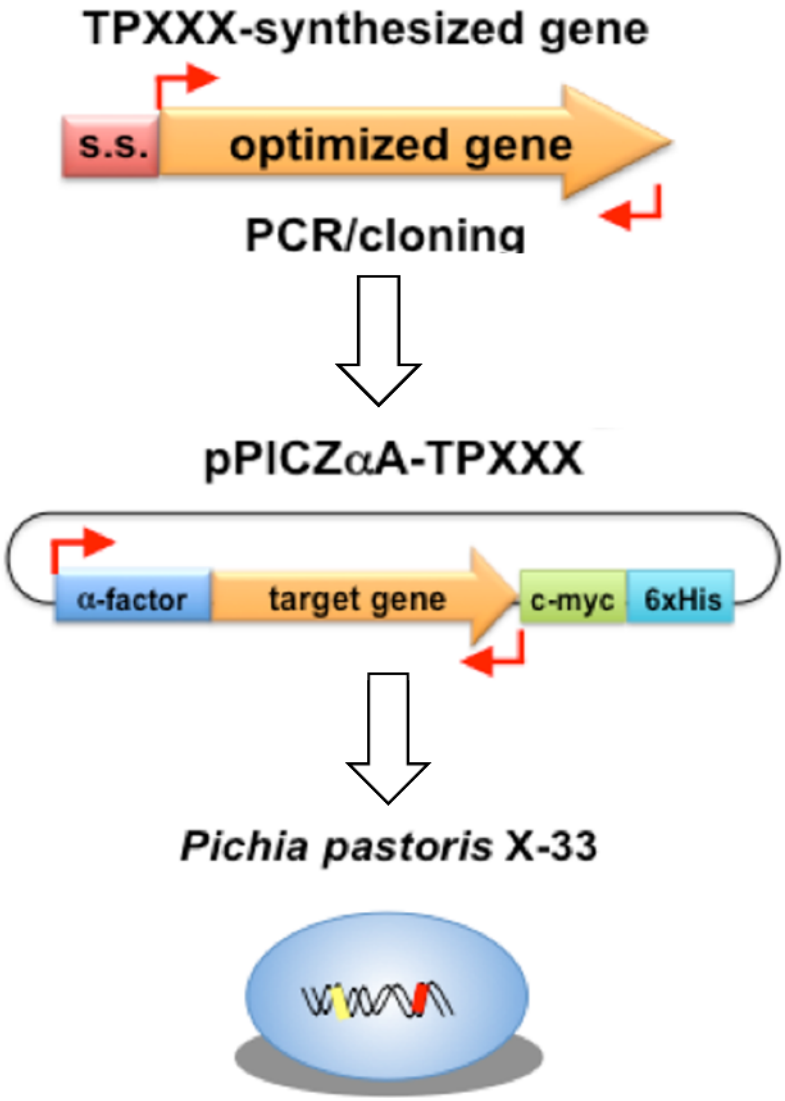

Figure 10. Construction of *Pichia pastoris* expression vectors for *Panus rudis* laccase
Codon-optimized cDNA of the *Panus rudis* laccase was amplified by PCR using appropriate pairs of primers represented by TPxxx-opt Fw (forward primer) and TPxxx-opt Rv (reverse primer) with the corresponding synthesized plasmid as a template. The PCR products from these were then digested with EcoRI and XbaI, and then cloned into the corresponding restriction sites on the pPICZ-alpha plasmid to yield a series of expression vectors for *P. pastoris.*

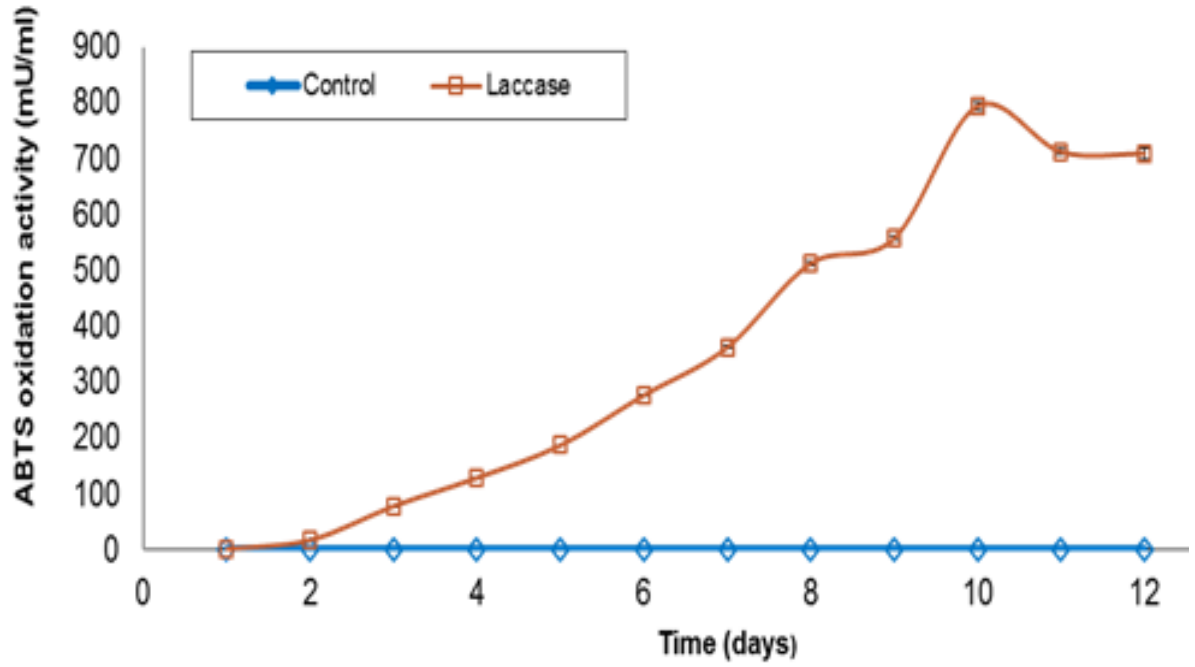

Figure 11. Time-course of heterologous expression of *Panus rudis* laccase.
The proportion of the secreted enzyme being produced in media on a daily basis was confirmed by 1 ml aliquots of the culture whose activities were then tested on 2,2'-azino-bis(3-ethylbenzothizoline-6-sulphonic acid) (ABTS), a substrate widely used for observing the reaction kinetics of lignin degrading enzymes.

3.3 Characterisation of *Panus rudis* laccase (Solid phase assay)

Substrate diversity of the laccase was tested on solid agar plates containing the two most common compounds used for testing laccase activity, the synthetic compound, ABTS and the naturally occurring DMP. Three S-type phenolic compounds which have all been identified as mediators in low potential laccases oxidation of non-phenolic portions of lignin (sinapic acid, syringaldehyde and acetosyringone) were also used in the plate assay. All five substrates are shown in Figure 12. The intensity of the halo around each substrate at varying laccase concentrations corresponds roughly to the ability of the enzyme to oxidise the substrate of interest (Pardo et al., 2013). Figure 13 shows that the laccase is easily able to oxidise the mediators ABTS and DMP at low concentrations and an increase in the intensity and circumference of the halo with increasing concentrations of laccase supernatant was observed. With the S-type phenolic compounds, more of the laccase supernatant is required before substrate oxidisation can be observed. The relationship between enzyme concentration and halo intensity and circumference is linear as with ABTS and DMP. The optimum pH of 3.0 for laccase activity is constant for all five substrates as a significant decrease in intensity and circumference of the halos was observed with the change of pH to 5.0.

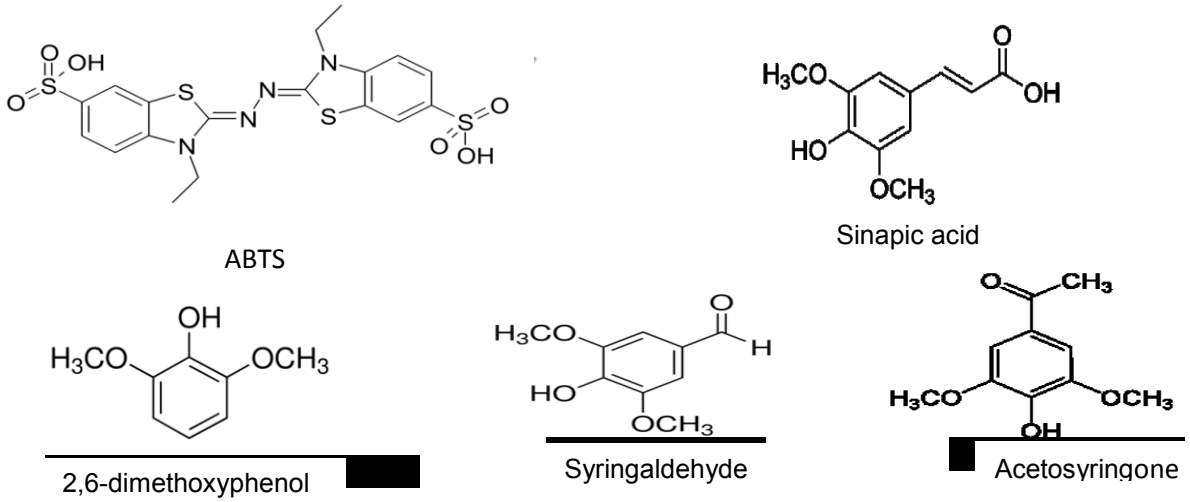

Figure 12. The five substrates used in the solid phase (plate) assay

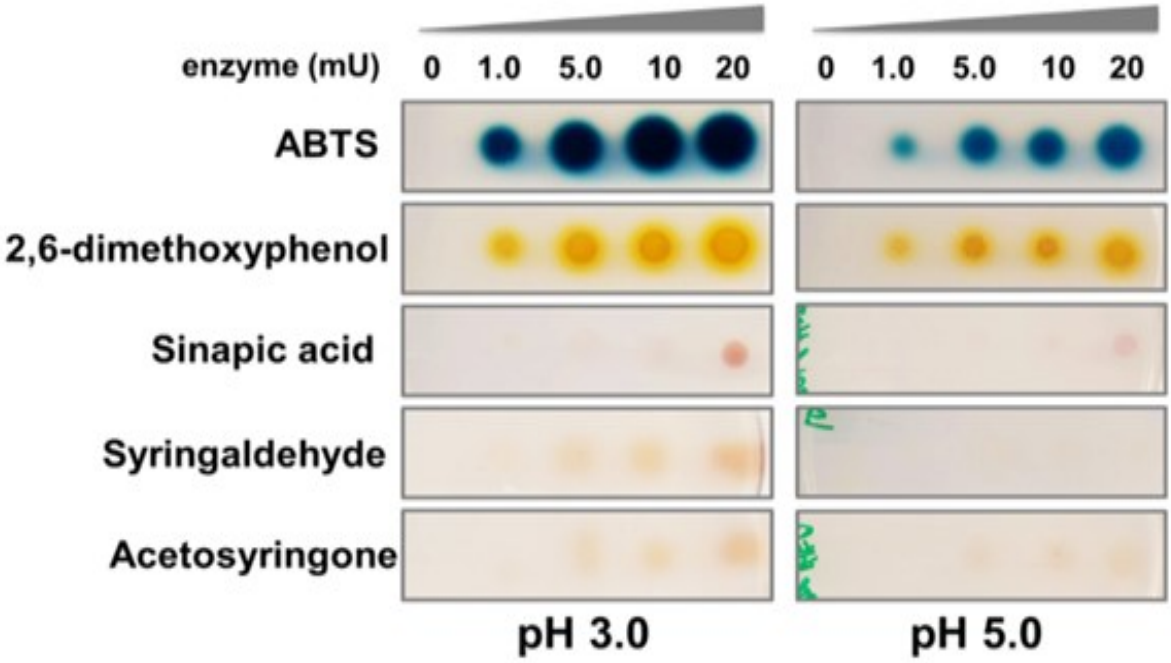

Figure 13. Plate assay for characterization of *Panus rudis* laccase

The substrate specificity of *Panus rudis* laccase was determined by using five different lignin model compounds. They include 2,2'-azino-bis(3-ethylbenzothizoline-6-sulphonic acid) (ABTS), 2,6 dimethoxyphenol (DMP), sinapic acid, syringaldehyde and acetosyringone. The halo intensity corresponds to the activity of the laccase with increasing concentrations of the enzyme leading to stronger reactions on the substrate. There is a dramatic reduction in the halo intensity when the pH is increased from 3.0 to 5.0 showing that pH 3.0 is better for the *Panus rudis* laccase's activity.

3.4 Characterisation of *Panus rudis* laccase (Liquid phase assay)

The optimum pH of the *Panus rudis* laccase was determined by examining the rate of enzyme activity (mole of ABTS oxidised per minute) and the results of which are presented in Figure 14. The pH determination was carried out at 20 °C in ammonium acetate buffer. It was observed that the *Panus rudis* laccase had its highest activity (0.127 ± 0.003 mM of ABTS oxidised/min) at pH 3.0. An increase in the reaction mixture's pH to 4.0 led to a 44% decrease in the laccase's activity (to 0.071 ± 0.006 mM of ABTS oxidised/min). An increase in the pH of the reaction mixture from 4.0 to 5.0 leads to a further 53% decrease in the activity of the laccase (0.033 ± 0.001 mM of ABTS oxidised/min). With a change in the pH of the reaction mixture from 3.0 to 5.0 there is a large decrease (74% decrease) in the laccase's ability to oxidise ABTS. A one-way ANOVA was performed on the optimum pH test and it showed that the differences in the mean values of the pH values (3.0, 4.0 and 5.0) are statistically significantly different ($P =< 0.001$) and that the differences are greater than would be expected by chance alone.

The optimum temperature for *Panus rudis* laccase activity was determined at pH 3.0 and the results are presented in Figure 15. It was observed that the activity of the laccase at 20 °C was 0.127 ± 0.003 mM of ABTS oxidised/min, an increase of 10 °C, to 30 °C, leads to a 7% increase in activity (0.136 ± 0.006 mM of ABTS oxidised/min). An increase of 20 °C to 40 °C leads to a 14% increase in activity (0.145 ± 0.004 mM of ABTS oxidised/min) and an increase of 30 °C, to 50 °C, leads to a 20% increase in activity (0.152 ± 0.009 mM of ABTS oxidised/min). An increase of 40 °C, to 60 °C, leads to a 22% increase in activity, whereas an increase of 50 °C, to 70 °C, leads to a 35% decrease in activity (0.082 ± 0.021 mM of ABTS oxidised/min). A one-way ANOVA was performed on the optimum temperature test and it showed that the differences in the rank sums of the temperature values from 20 °C to 60 °C

are not statistically significantly different ($P < 0.05$) but when each of the rank sums for the temperature values (20 ºC to 60 ºC) are compared to temperature 70 ºC, there is a statistically significant difference ($P < 0.05$).

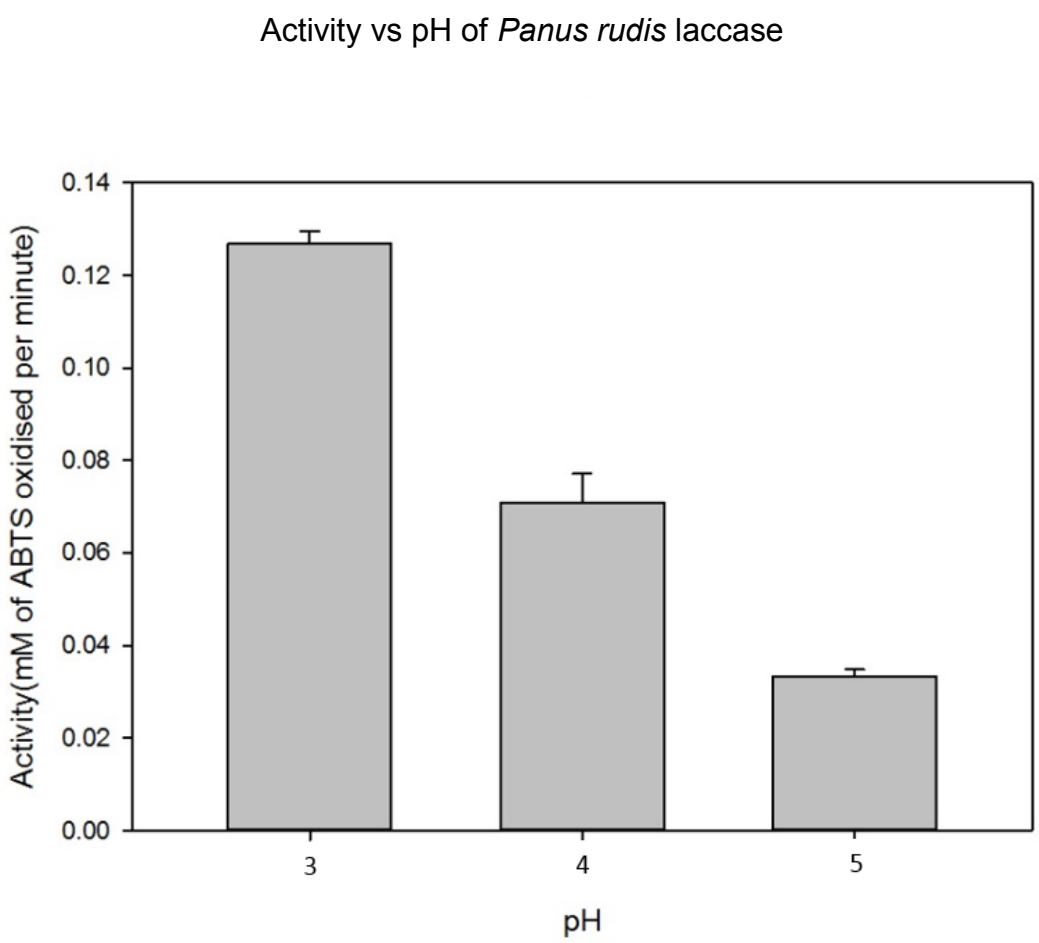

Figure 14. Effect of pH on the activity of the *Panus rudis* laccase
The effect of pH change on the activity of *Panus rudis* laccase (mM ABTS oxidised per minute) was determined using the substrate ABTS. This shows a statistically significant reduction in activity when the reaction pH is changed from pH 3.0 to pH 4.0 and the same statistically significant reduction in activity is observed when the pH is changed from pH 4.0 to 5.0.

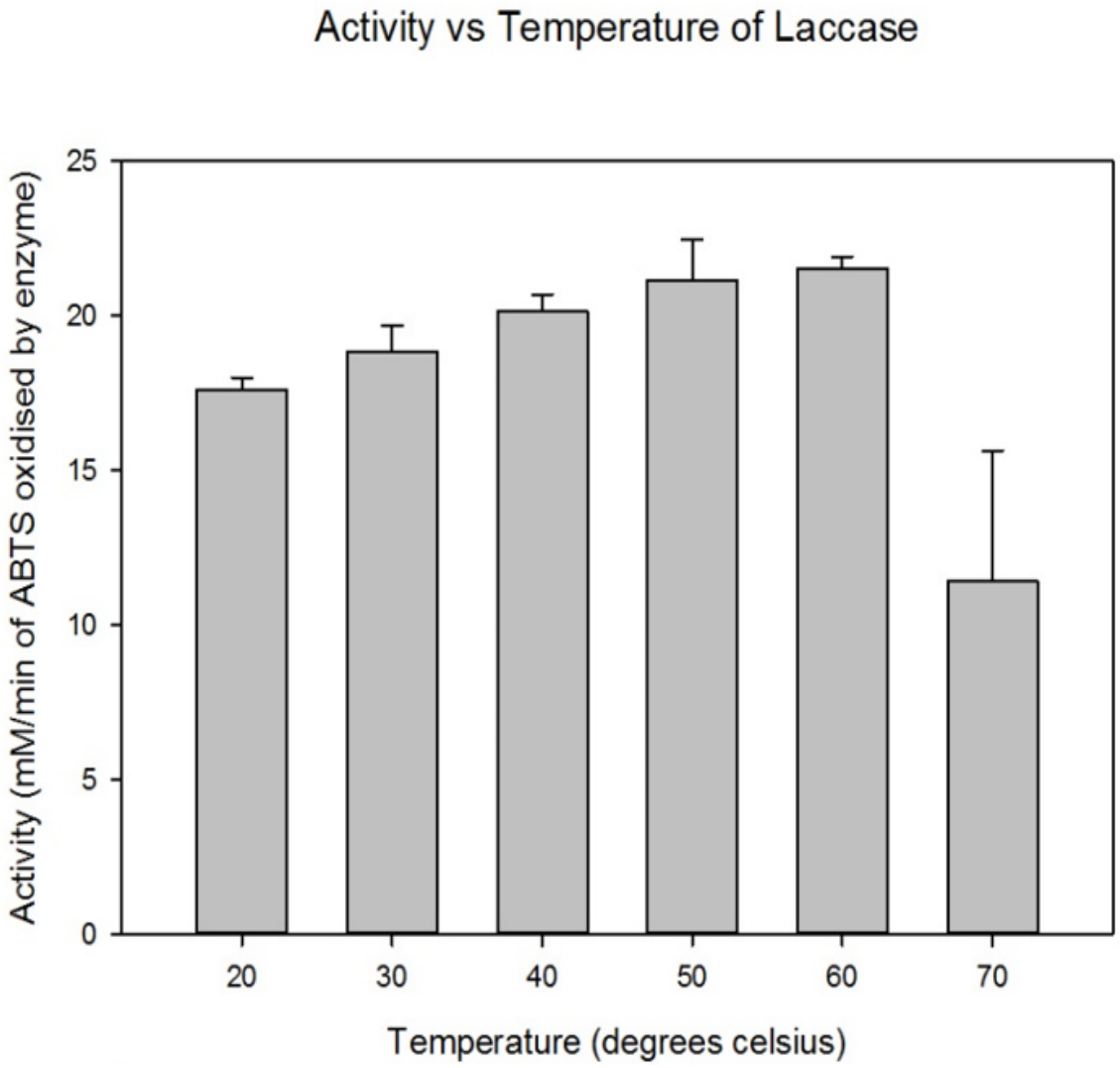

Figure 15. Effect of temperature on the activity of the *Panus rudis* laccase
The effect of temperature change on the activity of *Panus rudis* laccase was determined using the substrate, ABTS. A bar graph showing the activity of the *Panus rudis* laccase (mM ABTS oxidised per minute) at various temperatures (20 °C - 70 °C) shows that between 20 °C – 60 °C, there are slight increases in the activity of the laccase but on the increase of the temperature to 70 °C, there is a sharp drop in the *Panus rudis* laccase's activity.

3.5 Scanning Electron Microscopy

Scanning electron microscopy (SEM) has been used in previous studies to investigate the surface structures of the lignin molecule during enzymatic degradation and also to differentiate between different technical lignin classes (Mukhopadhyay and Banerjee, 2015, Ahvazi et al., 2016, Cheng et al., 2012). I used SEM to investigate the differences in the surface morphology of the Kraft lignin during a one-week reaction with the *Panus rudis* laccase. The major difference I observed was that the Kraft lignin (Sigma-Aldrich) that had not been mixed in solution with the enzyme and mediator then freeze-dried had an overall regular and well-defined morphology, whereas the lignin treated with the laccase and mediators when freeze-dried showed highly irregular surfaces as shown in Figure 16 below. This shows that physical processes like freeze-drying in themselves could be useful in lignin pre-treatment. SEM was used to observe the changes in lignin degraded by *Pseudomonas sp.* Q18 and also pine, kraft lignin and paper pulp degraded by *Bacillus subtilis* WB800 in which gluthathione-S-transferase, laccase and lignin peroxidase had been over-expressed. (Yang et al., 2018, Ozer et al., 2017). SEM was useful in monitoring the progress of delignification and hemicellulose removal from various biomass material pretreated with xylanase and alkaline solution for nanocellulose extraction (Vanitjinda, Nimchua and Sukyai, 2019) and to compare the effect of different commercial xylanases with endoglucanase on softwood and hardwood bleached Kraft pulp for the production of nanofibrillated cellulose (Long et al., 2017). SEM has also been used to study the morphological effect on lignin when it is blended into thermoplastic or biocomposite materials to improve their thermostability and mechanical properties to enhance their use in the bioplastics and construction industry. (Sailaja and Deepthi, 2010, Maldhure, Ekhe and Deenadayalan, 2012).

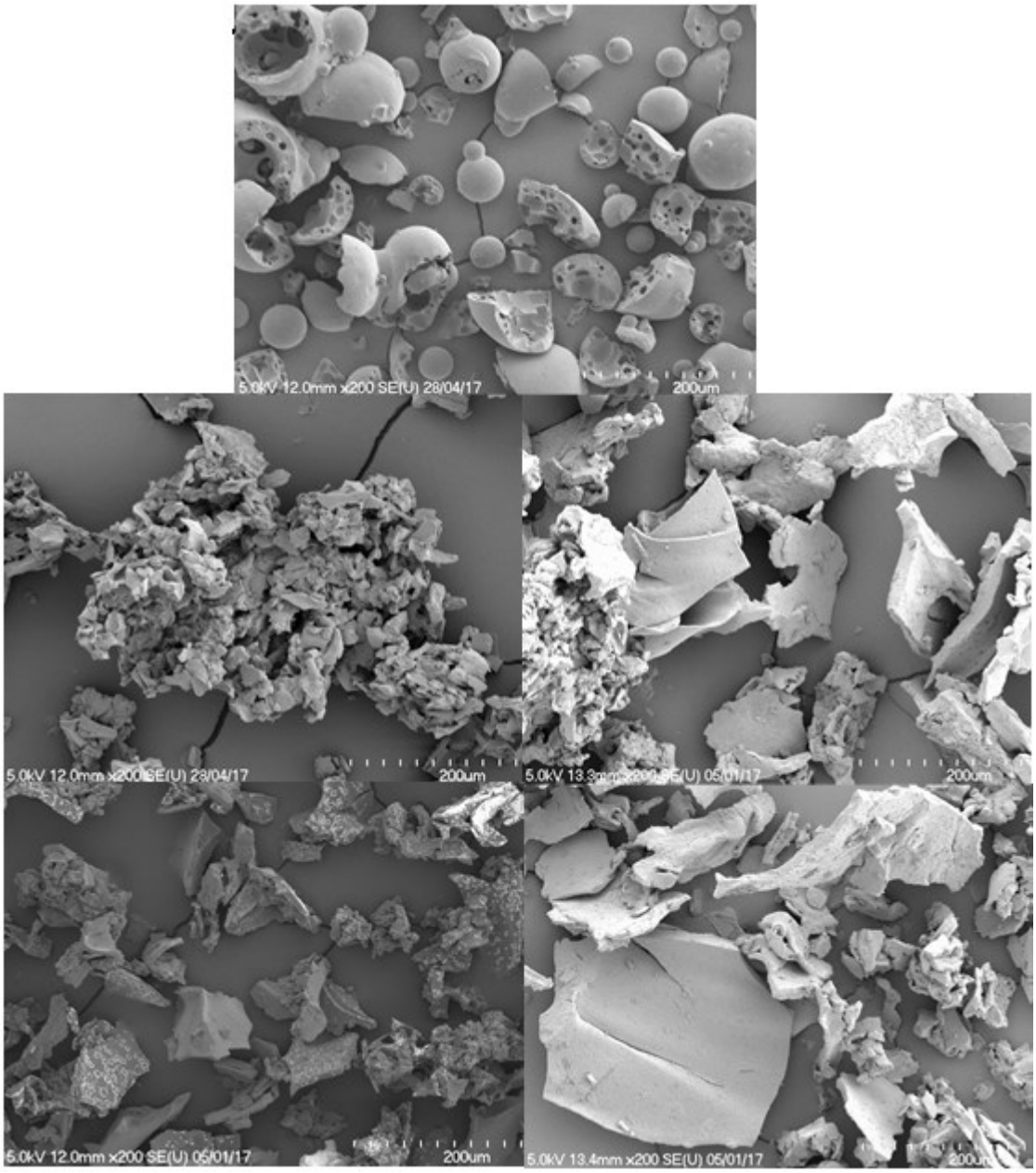

Figure 16. SEM micrographs of untreated and treated Kraft lignin

The figure above shows: (A) untreated Kraft lignin at the beginning of the experiment time, t = 0, before adding it to the reaction mixture and the lignin molecules have well defined and round looking surfaces with some depressions and holes present as well; (B) and (C) are freeze-dried Kraft lignin samples which have been degraded by *Panus rudis* laccase at time, t = 0 and t = 7 days respectively; while (D) and (E) are freeze-dried Kraft lignin samples which have been degraded by *Panus rudis* laccase with the aid of the mediator, acetosyringone at time, t = 0 and t = 7 days respectively. The samples were magnified 200 fold.

3.6 Fourier Transform Infrared (FTIR) Spectroscopy

FTIR spectroscopy is a technique used for analysing and determining the functional properties of lignin samples (Boeriu et al., 2004). This allows researchers to differentiate between technical lignins extracted from different species of plants and those from one plant that have been isolated using different extraction methods (Ahvazi et al., 2016). The regions in a typical IR spectra in relation to lignin degradation are divided into two with the region between 4000 and 1450 cm^{-1} called the functional group region, whereas the region between 1450 and 500 cm^{-1} due to a combination of complex vibrations is called the fingerprint region (Ferrer et al., 2016).

FTIR spectroscopy (4000cm^{-1} to 400cm^{-1}) in combination with principal component analysis (PCA) was used in this study to examine the effect of *Panus rudis* laccase (PrL) on Kraft lignin in the presence and absence of the mediator, acetosyringone over a one-week period. The most important peaks from the spectra obtained in the FTIR study of Kraft lignin are shown in the Table 3.6.

Table 3.6:- Stretching and vibration modes associated with lignin and their interpretation

Peak	Kraft lignin cm^{-1}	Interpretations (Popescu et al., 2007, Lupoi et al., 2015, Huang et al., 2012, Schwanninger et al., 2004, Boeriu et al., 2004)
1	3394	OH vibration and intra-molecular hydrogen bonds
2	2937	Symmetric CH stretching in aromatic methoxyl groups and in methyl and methylene groups of side chains
3	1590	aromatic skeletal vibrations plus C=O stretch
4	1502	aromatic skeletal vibration
5	1462	CH_2 of pyran ring symmetric scissoring and OH plane deformation vibration
6	1419	aromatic skeletal vibrations combined with C-H in plane deformation
7	1263	G ring plus C=O stretch
8	1213	OH plane deformation
9	1135	aromatic C-H in plane deformation
10	1081	C-O deformation in secondary alcohols and aliphatic ethers
11	1041	C*alkyl*-O ether vibrations
12	653	C-S stretch

3.6.1 Effect of Freeze-drying on Kraft lignin

To carry out the FTIR analysis, I had to freeze-dry all of the samples to remove the water and obtain a very dry specimen. Figure 17 shows the differences in the spectra of the Kraft lignin and the lignin dissolved in buffer and freeze-dried. There is a general reduction in the percentage transmittance in the freeze-dried lignin when compared to the untreated lignin. Another difference is the spectra of the untreated Kraft lignin at 3394 cm^{-1} and its shift to 3172 cm^{-1} in the freeze-dried lignin which indicates a change in the intramolecular hydrogen bonds and vibration of hydroxyl bonds. Both changes could be explained by the fact that the H_2O removed by the freeze-drying process is both a hydrogen donor and acceptor. Its

removal would therefore lead to the hydrogen bonds it was a part of being broken and this could explain the shift in the peak at 3394cm^{-1}. The other noticeable difference is the appearance of a curve at 1697 cm^{-1} in the freeze-dried lignin and also a depression at 1416 cm^{-1}. Both changes are not present in the untreated Kraft lignin and correspond to vibrations in the aromatic skeleton and stretching of the carbonyl bonds. The changes could also be due to the withdrawal of water from the lignin causing exposure of bonds that were formerly bound to water before it was removed.

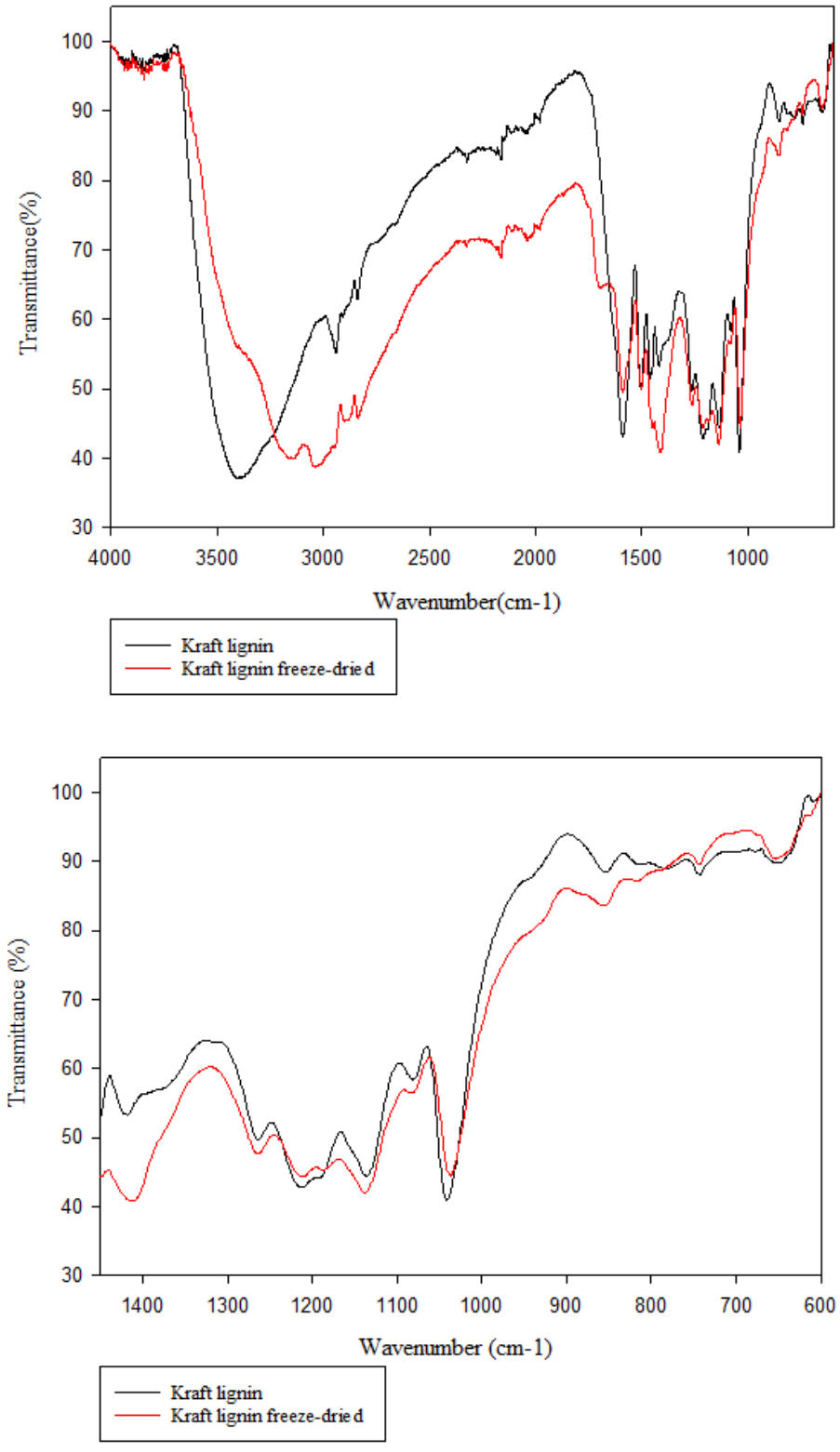

Figure 17. FTIR spectra of untreated Kraft lignin and freeze-dried lignin.

3.6.2 Effect of *Panus rudis* laccase on Kraft lignin using FTIR:-

The effect of PrL on Kraft lignin was determined by FTIR and is shown in Figures 18 (a) and (b), any major changes observed are discussed below. FTIR spectra are made up of the interaction of the infrared radiation with a lot of different bonds present in the test samples and this provides a lot of information that needs to be disentangled to obtain useful information from the spectra generated. The plots reveal slightly different shifts at several wavelengths but to truly understand the overall impact of the PrL on Kraft lignin, a multivariate analysis known as principal component analysis needs to be performed.

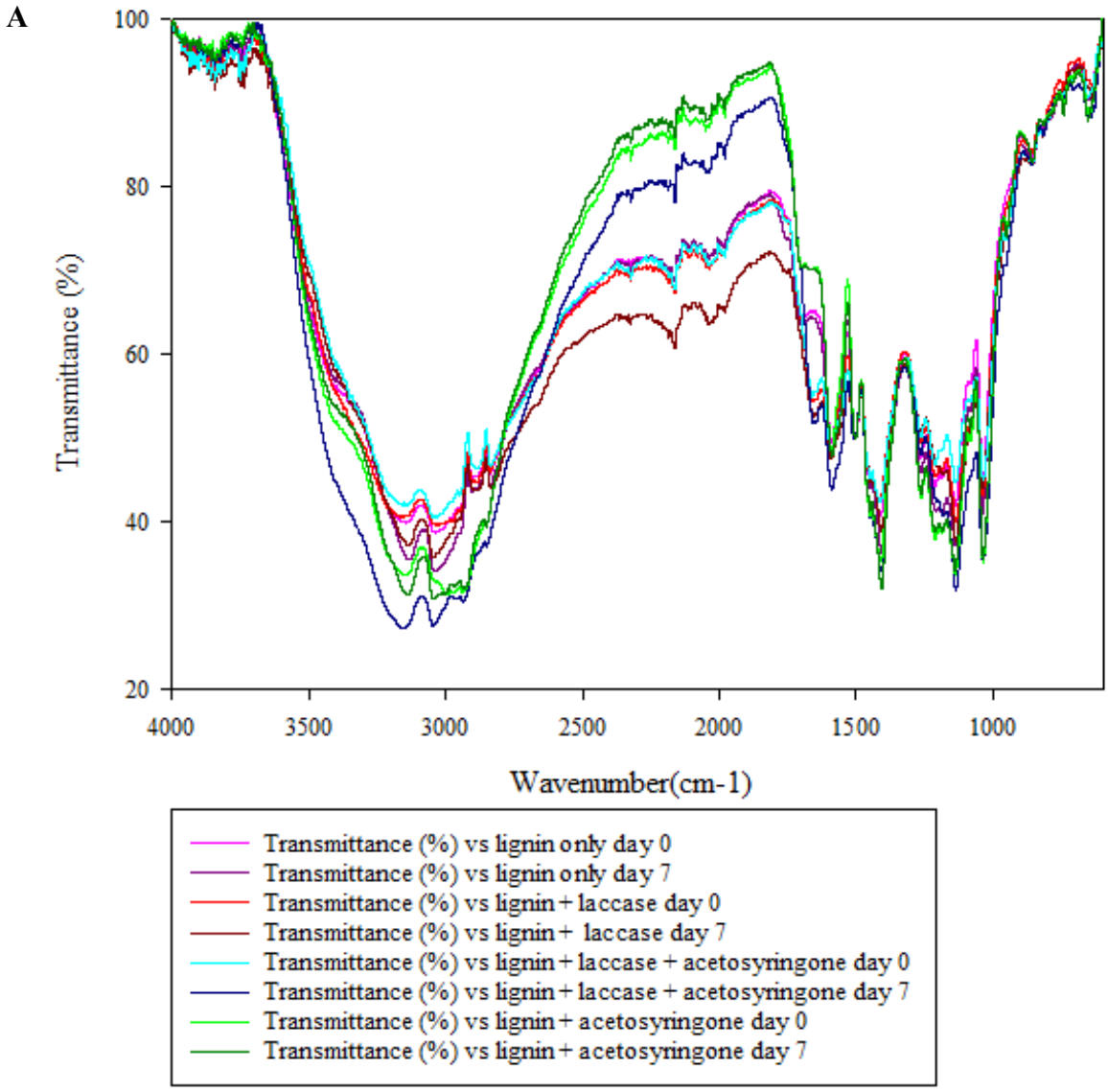

B

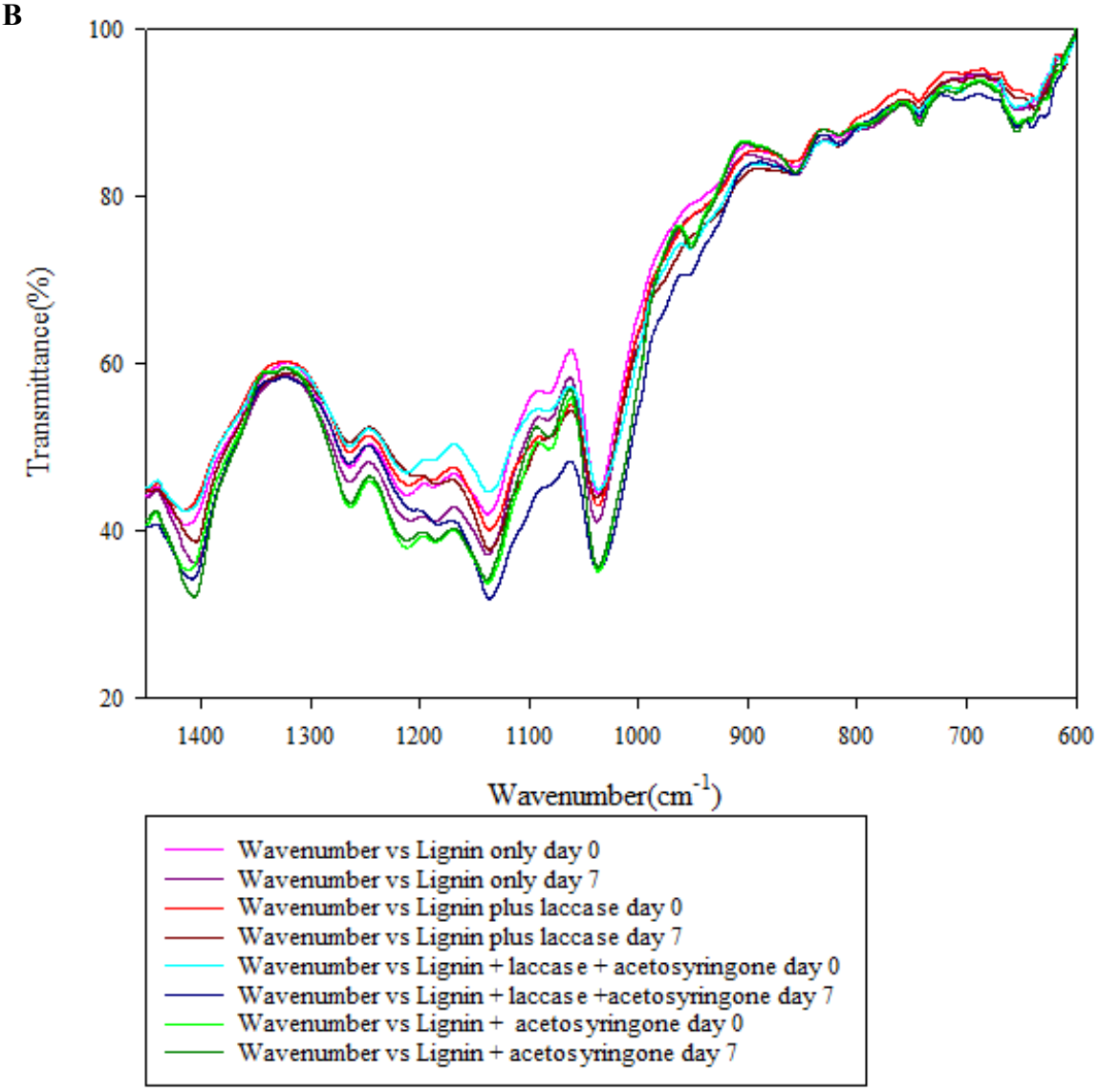

Figure 18. FTIR spectra of untreated Kraft lignin and freeze-dried lignin after a seven day period.

The rest of the graphs show all of the Kraft lignin treatments (a) laccase only,(b) laccase and acetosyringone and (c) acetosyringone only at the beginning of the incubation at 25^0C (day 0) and after seven days of incubation at 25^0C (day 7). The first figure shows the entire spectra from 4000cm^{-1} and the second figure is focused on the more complex fingerprint region from 1450cm^{-1} to 600cm^{-1}.

3.6.3 Principal component analysis (PCA) of the effect of laccase on Kraft lignin

Principal component analysis aids the understanding of the changes taking place during the degradation of the Kraft lignin by the laccase and mediator by reducing the spectral information to a few principal components. These principal components are plotted against each other to give a synopsis of the major qualitative information present in the infrared spectra (Chen et al., 2010a). The PCA was carried out using SigmaPlot 13.0 (Systat Software, San Jose, CA). To perform this, first the percentage transmittances obtained from the raw FTIR spectra were examined for changes around the wavenumbers of interest in Table 3.6. The percentage transmittances were collated and percentage absorbance calculated as (100 - %T) was obtained for each of the selected wave numbers. From the results, the absorbance ratios: 3394/1502, 2937/1502, 1590/1502, 1462/1502, 1419/1502, 1263/1502, 1213/102, 1135/1502, 1081/1502, 1041/1502 and 653/1502 were determined, and SigmaPlot was used to generate a correlation matrix for the data. A chi-square test performed on the eigenvalues of the correlation matrix showed that there is a significant difference in the eigenvalues ($P<0.001$) and the data was suitable for PCA. Any similarity in any of the eigenvalues would mean that a PCA could not be performed on the FTIR data. There are several plots that can be generated from the PCA results and the first of these is the scree plot, which is a plot of the components (x axis) against the component numbers. This is shown in Figure 19 and enables the determination of the minimum number of principal components that would best describe all of the variations present in the FTIR data

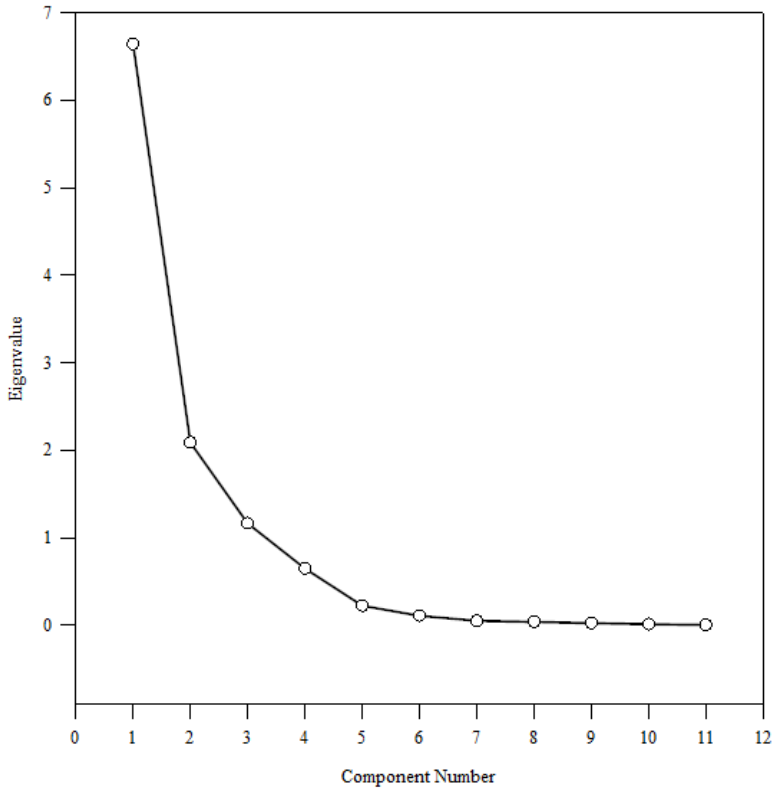

Figure 19. A scree plot of the eigenvalues of the component number.
There are 11 component numbers indicating the number of wavelength ratios entered for the principal component analysis (PCA). The eigenvalues correspond to the variance in each of the principal components.

From the scree plot above, the number of principal components that have an eigenvalue above 1, is 3 and this means that the minimum number of principal components that can be used to correctly describe the differences observed between all samples at the beginning (day 0) and end (day 7) is 3 main principal components (PC1, PC2 and PC3) with PC1 accounting for 60.42%, PC2 for 18.98% and PC3 for 10.58% which adds up to 89.98% and this covers the majority of the variance observed in the dataset while the remaining 10.02% difference cannot be clearly determined using the PCA. All of the absorbance ratios used are assigned a component score dependent on which of the principal components they show their major differences with. The component scores are determined from the coefficient of each principal

component. The component scores of the principal components are in are then plotted as shown in Figures 20 (a) and (b) as plots of PC1 against PC2 and PC1 against PC3.

Table 3.6.1. Component scores of the principal components

Absorbance ratios	**PC1**	**PC2**	**PC3**
3394/1502	0.405	0.857	- 0.133
2937/1502	0.921	- 0.236	0.153
1590/1502	0.0526	0.902	0.296
1462/1502	0.891	- 0.324	0.0643
1419/1502	0.830	- 0.470	0.154
1263/1502	0.852	- 0.133	- 0.421
1213/1502	0.857	0.151	- 0.364
1135/1502	0.860	0.0598	0.336
1081/1502	0.782	0.0770	0.594
1041/1502	0.941	0.285	- 0.0517
653/1502	0.671	0.158	0.479

(A)

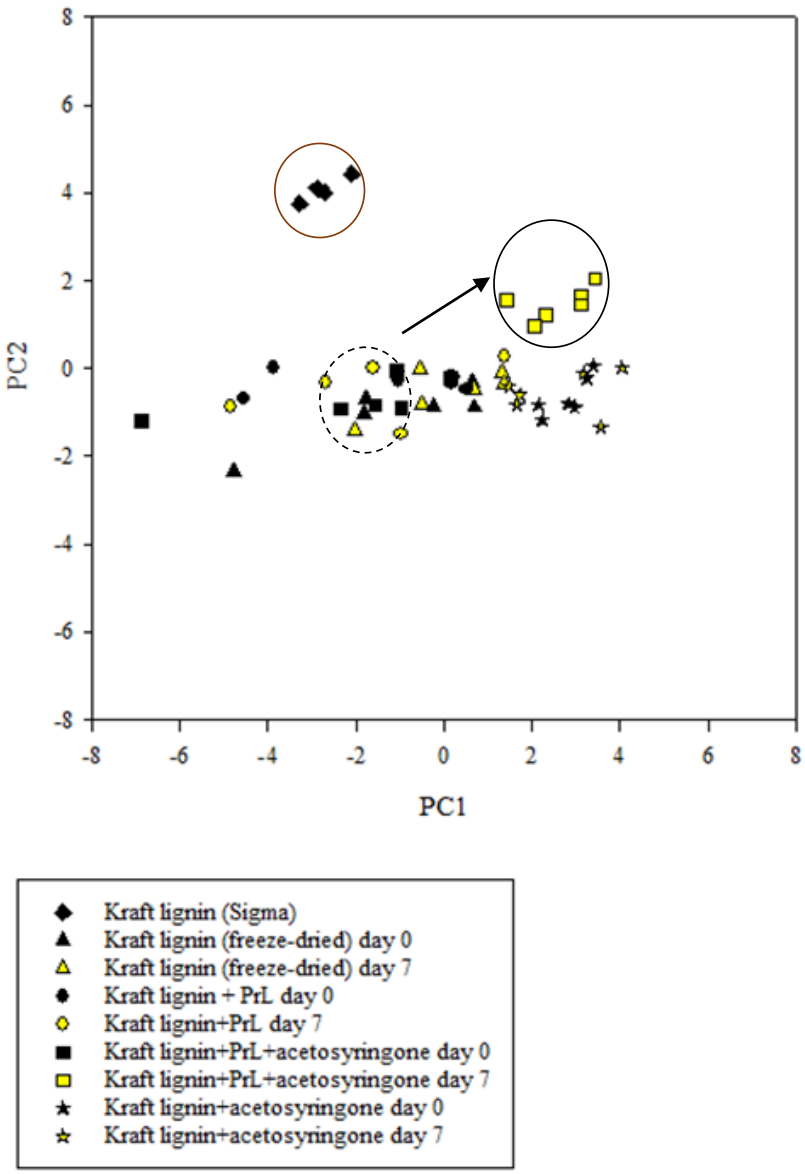

Figure 20a. Plot of the first principal component against the second principal component (PC1 vs PC2)

The figure above shows the relationship between the first two component scores. These two account for 79.4% of the variance between the various treated samples. The most distinct clustering is that between three main groups: (a) the non-degraded Kraft lignin (Sigma-Aldrich); (b) the Kraft lignin non-degraded with *Panus rudis* laccase and acetosyringone at time, t = 0 days (black squares) and (c) the Kraft lignin degraded by *Panus rudis* laccase and acetosyringone at time, t = 7 days (yellow squares).The downward shift from the untreated Kraft lignin to the freeze-dried pre-degraded Kraft lignin could be due to the changes in the OH bonds due to removal of water during the freeze-drying process while the shift to the right could be due to changes in the various bonds of the lignin after being degraded by *Panus rudis* laccase and acetosyringone.

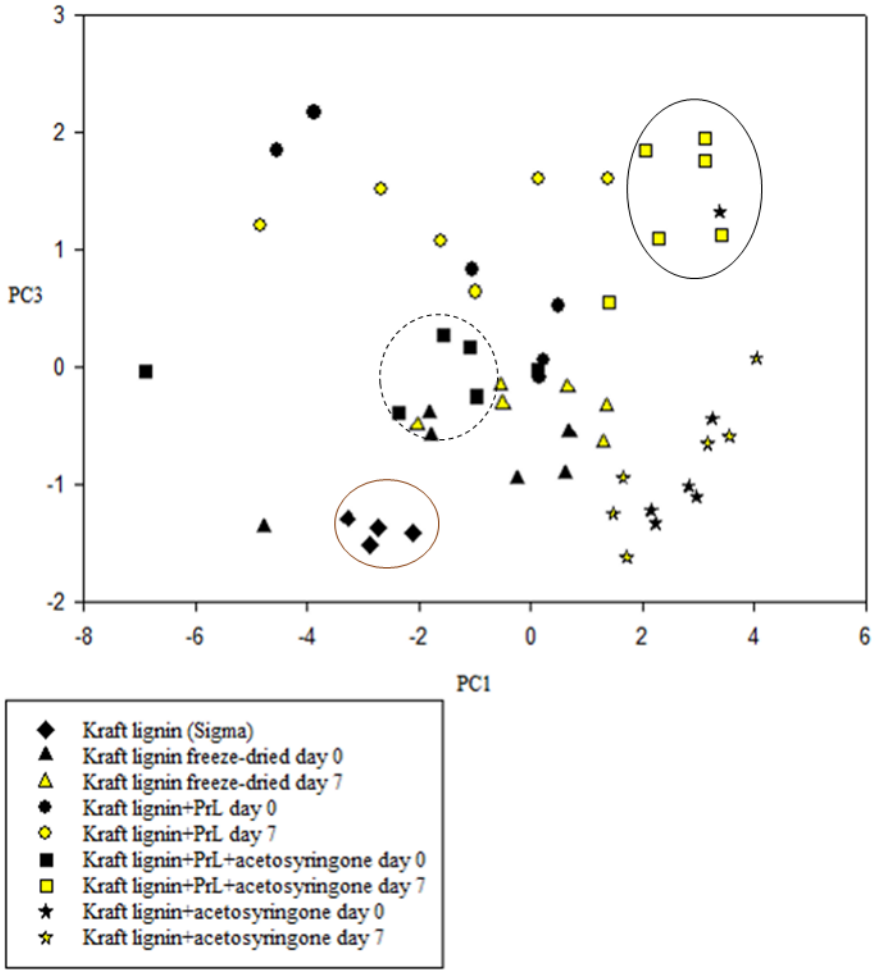

Figure 20b. Plot of the first principal component against the second principal component (PC1 vs PC3)
The figure above shows the relationship between the first and third principal component scores. These two account for 71% of the variance between the various treated samples. The most distinct clustering is that between three main groups: (a) the non-degraded Kraft lignin (Sigma-Aldrich); (b) the Kraft lignin non-degraded with *Panus rudis* laccase and acetosyringone at time, t = 0 days (black squares) and (c) the Kraft lignin degraded by *Panus rudis* laccase and acetosyringone at time, t = 7 days (yellow squares).The upward shift from the untreated Kraft lignin to the freeze-dried pre-degraded Kraft lignin is mainly due to the changes in the OH bonds linked to water removal during the freeze-drying process while the shift to the right could be due to changes in the stretching and vibration of the various bonds present in the lignin as listed in Table 3.6 after being degraded by *Panus rudis* laccase and acetosyringone.

The principal component plot enables the differentiation of the different samples based on their loadings on each axis and by plotting PC1 against both PC2 and PC3, it enables a clear visualisation of the difference between the Kraft lignin degraded by just the *Panus rudis*

laccase alone and when both the *Panus rudis* laccase and acetosyringone are used. The major differences in both plots is notably along the PC1 axis where all of the loadings are positive while on the PC2 and PC3 axis there are various negative loadings. The loadings plot indicate that the three most important wavelengths involved in the changes involved are 1041cm^{-1}, 1213cm^{-1} and 653cm^{-1}, i.e. showing that the major differences in the use of the laccase and acetosyringone and just laccase alone on the lignin are vibrations of the alkyl C-O ether bonds, deformations of the OH planes and stretching of the C-S bonds present throughout the Kraft lignin molecule.

3.7 Summary and discussion

Panus rudis laccase (PrL) was expressed using the *Pichia pastoris*, a methylotropic eukaryotic organism. The major advantage to doing this is the fact that any post-translational modifications, particularly the glycosylation, which is important to laccase activity (Wong, 2009) could be done and the active enzyme was successfully expressed into the media.

The use of SEM enables a close morphological examination of the lignin macromolecule and all of the changes it undergoes during degradation. FTIR was used to further buttress these observations by showing that the degradation process in lignin takes places by the stretching and vibration of the numerous bonds that are present in lignin. FTIR also enables the monitoring of the functional groups that are most likely to be degraded by the *Panus rudis* laccase (Faix, 1991, Faix, 1992).

By combining FTIR with PCA, I was able to show through the distinct clustering on the principal component plots that the combination of the *Panus rudis* laccase and acetosyringone was able to significantly modify the Kraft lignin by modifying the C-O ether bonds, the OH bonds and the C-S bonds present within it. The distinct clustering of this group and their sideways shift indicated the presence of a group that had been acted on by a similar set of reactions. This illustrates the ability of the PCA to simplify very complex data (Chen et al., 2010a)

Chapter 4: Determination of the Effect of *Panus rudis* laccase on Kraft lignin by Electrospray Ionisation Fourier Transform Ion Cyclotron Resonance Spectroscopy (ESI-FTICRMS)

4.1 Introduction

I utilised Electrospray Ionisation Fourier Transform Ion Cyclotron Resonance Spectroscopy (ESI-FTICRMS) to monitor the 1-week degradation of Kraft lignin by *Panus rudis* laccase, and various mediator compounds (acetosyringone, HBT and guaiacol). The reaction mixtures at the end of each laccase-mediator reaction were sampled after one week (t = 7 days) and compared to the reaction mixture before the start of lignin degradation (t = 0). ESI was utilised because it is a gentle ionisation technique, and has been utilised in the identification of the degradation products from other organic compound mixtures such as humic acid and fulvic acid (Stenson, Marshall and Cooper, 2003, Kujawinski et al., 2002). ESI-FTICRMS also allows detailed screening of the degradation products (Marjasvaara, Torvinen and Vainiotalo, 2005). This is especially important because of the sheer number and complexity of the spectra of lignin and its degradation products.

A.

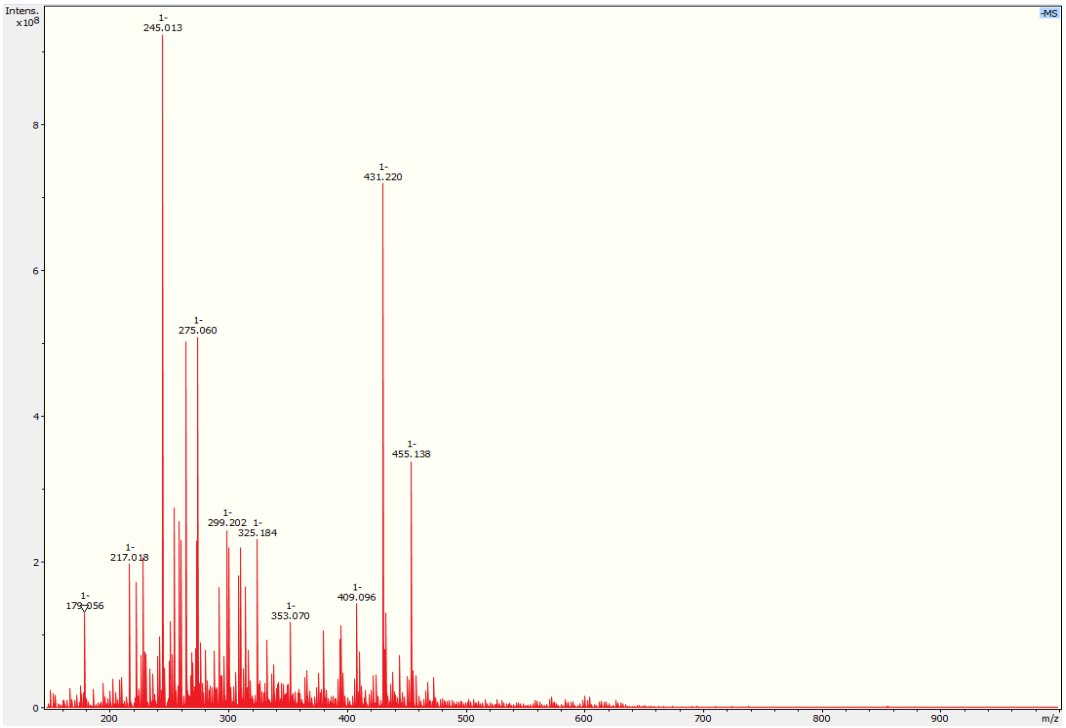

B.

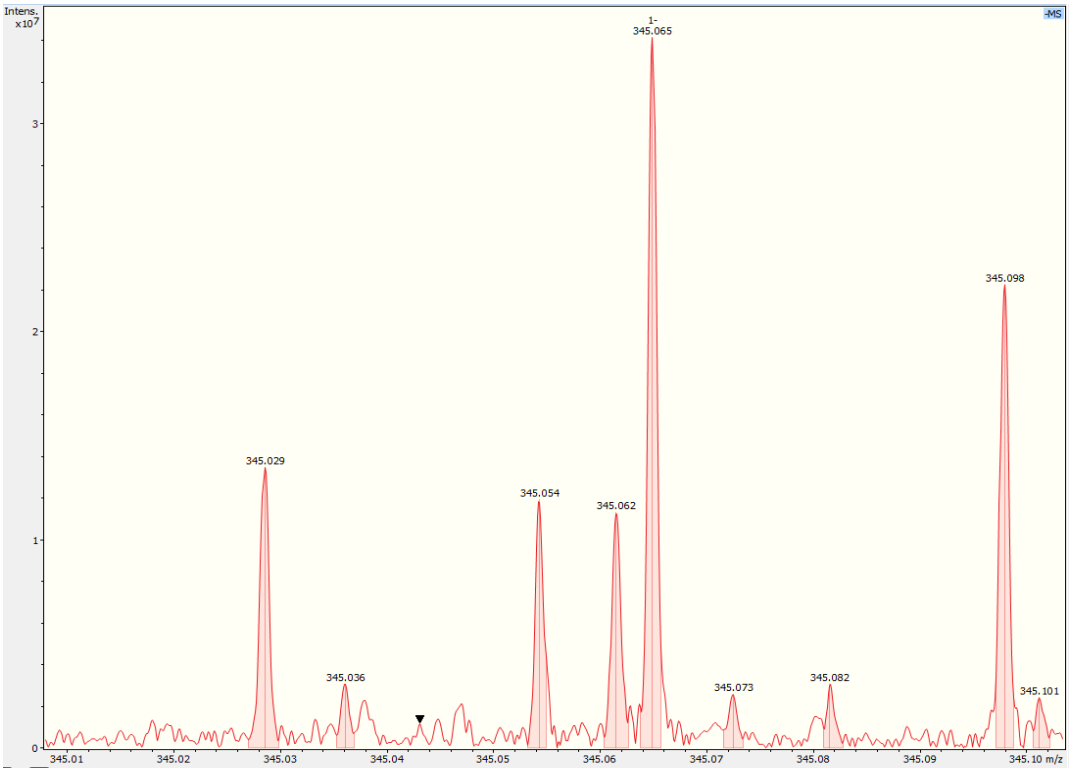

Figure 21 (a) and (b). Mass spectra of Lignin
The figures above represent - (a) the processed spectra of undegraded lignin showing the large number of peaks that are present at each mass/charge (m/z) position on the x-axis, and (b) which shows the nine peaks that are present between 345.01 and 345.10 m/z. Both illustrate the complexity of lignin as a substrate and the sensitivity of ESI-FTICRMS to detect all of these compounds.

4.2 Calibration of Spectra

Due to the complexity of the spectra obtained for each sample from the ESI-FTICR mass spectrometer, there is need to calibrate the resulting spectra to enable an accurate comparison of the various classes of samples. A well calibrated spectra ensures that the chemical formula determination of the lignin degradation products is highly accurate. The calibration list used for this project was developed by Dr David Clarke, Mattias Tinzl and Dr Virginia Echavarri-Bravo and is shown in Table 4.1. I carried out the calibration using the Compass DataAnalysis software (Bruker Daltonic). I selected peaks with a signal to noise ratio higher than 4 were and ran the data through the PetroOrg software for the assignment of peaks.

Table 4.1. Calibration list for Kraft lignin (Jarrell et al., 2014, Miettinen et al., 2015, Tessarolo et al., 2016)

Number	Ion Formula	Monoisotopic mass (Da)
1	$C_8H_7O_3$	151.04007
2	$C_9H_{11}O_2$	151.07645
3	$C_8H_9O_3$	153.05572
4	$C_9H_7O_3$	163.04007
5	$C_{10}H_{13}O_2$	165.09210
6	$C_8H_7O_4$	167.03498
7	$C_9H_{11}O_2$	167.07137
8	$C_{10}H_9O_4$	193.05063
9	$C_{11}H_{11}O_4$	207.06628
10	$C_{16}H_{17}$	209.13357
11	$C_{12}H_{13}O_4$	221.08193
12	$C_{15}H_{17}N_2$	225.13972
13	$C_{13}H_{11}O_4$	231.06628
14	$C_{15}H_{13}O_5$	273.07685
15	$C_{16}H_{17}O_4$	273.11323
16	$C_{18}H_{29}O_2$	277.21730
17	$C_{18}H_{31}O_2$	279.23295
18	$C_{18}H_{33}O_2$	281.24860
19	$C_{18}H_{35}O_2$	283.26425
20	$C_{18}H_{17}O_4$	297.11323
21	$C_{20}H_{27}O_2$	299.20165
22	$C_{16}H_{15}O_6$	303.08741
23	$C_{19}H_{19}O_4$	311.12888
24	$C_{17}H_{13}O_6$	313.07176
25	$C_{20}H_{21}O_4$	325.14453
26	$C_{18}H_{15}O_6$	327.08741
27	$C_{19}H_{35}O_4$	327.25408
28	$C_{18}H_{19}O_6$	331.11871
29	$C_{22}H_{42}NO$	336.32719
30	$C_{21}H_{23}O_4$	339.16018
31	$C_{22}H_{43}O_2$	339.32685
32	$C_{19}H_{17}O_6$	341.10306

33	$C_{22}H_{25}O_4$	353.17583
34	$C_{20}H_{19}O_6$	355.11871
35	$C_{23}H_{27}O_4$	367.19148
36	$C_{24}H_{47}O_2$	367.35815
37	$C_{20}H_{19}O_7$	371.11363
38	$C_{18}H_{19}O_7S$	379.08570
39	$C_{20}H_{21}O_8$	389.12419
40	$C_{22}H_{17}O_7$	393.09798
41	$C_{18}H_{19}O_8S$	395.08061
42	$C_{25}H_{25}O_5$	405.17075
43	$C_{23}H_{19}O_7$	407.11363
44	$C_{24}H_{27}O_6$	411.18131
45	$C_{24}H_{21}O_7$	421.12928
46	$C_{28}H_{55}O_2$	423.42075
47	$C_{19}H_{21}O_9S$	425.09118
48	$C_{27}H_{27}O_5$	431.18640
49	$C_{25}H_{23}O_7$	435.14493
50	$C_{26}H_{31}O_6$	439.21261
51	$C_{27}H_{29}O_6$	449.19696
52	$C_{25}H_{23}O_8$	451.13984
53	$C_{24}H_{22}O_9$	454.12693
54	$C_{26}H_{27}O_8$	467.17114
55	$C_{23}H_{21}O_9S$	473.09118
56	$C_{23}H_{23}O_9S$	475.10683
57	$C_{23}H_{25}O_{10}S$	493.11739
58	$C_{28}H_{29}O_8$	493.18679
59	$C_{26}H_{23}O_{10}$	495.12967
60	$C_{27}H_{27}O_9$	495.16606
61	$C_{28}H_{29}O_9$	509.18171
62	$C_{30}H_{27}O_8$	515.17114
63	$C_{29}H_{31}O_9$	523.19736
64	$C_{26}H_{27}O_{10}S$	531.13304
65	$C_{30}H_{33}O_9$	537.21301
66	$C_{31}H_{25}O_{10}$	557.14532
67	$C_{27}H_{27}O_{11}S$	559.12796
68	$C_{31}H_{31}O_{11}$	579.18719
69	$C_{30}H_{29}O_{10}S$	581.14869
70	$C_{32}H_{31}O_{11}$	591.18719
71	$C_{30}H_{35}O_{11}S$	603.19056
72	$C_{33}H_{29}O_{12}$	617.16645
73	$C_{30}H_{35}O_{12}S$	619.18547
74	$C_{35}H_{29}O_{12}$	641.16645
75	$C_{31}H_{33}O_{13}S$	645.16474
76	$C_{36}H_{31}O_{13}$	671.17701
77	$C_{38}H_{31}O_{13}$	695.17701
78	$C_{37}H_{31}O_{14}$	699.17193
79	$C_{37}H_{35}O_{12}S$	703.18547
80	$C_{38}H_{33}O_{14}$	713.18758
81	$C_{39}H_{31}O_{15}$	739.16684
82	$C_{40}H_{39}O_{15}$	759.22944
83	$C_{41}H_{37}O_{16}$	785.20871

4.3 Class distribution of the lignin degradation products

To get a quick idea of the changes taking place in the myriad of degradation products being generated during the degradation of lignin, I generated a plot of the heteroatomic classes at the beginning (day 0) and at the end (day 7) of the degradation experiment.

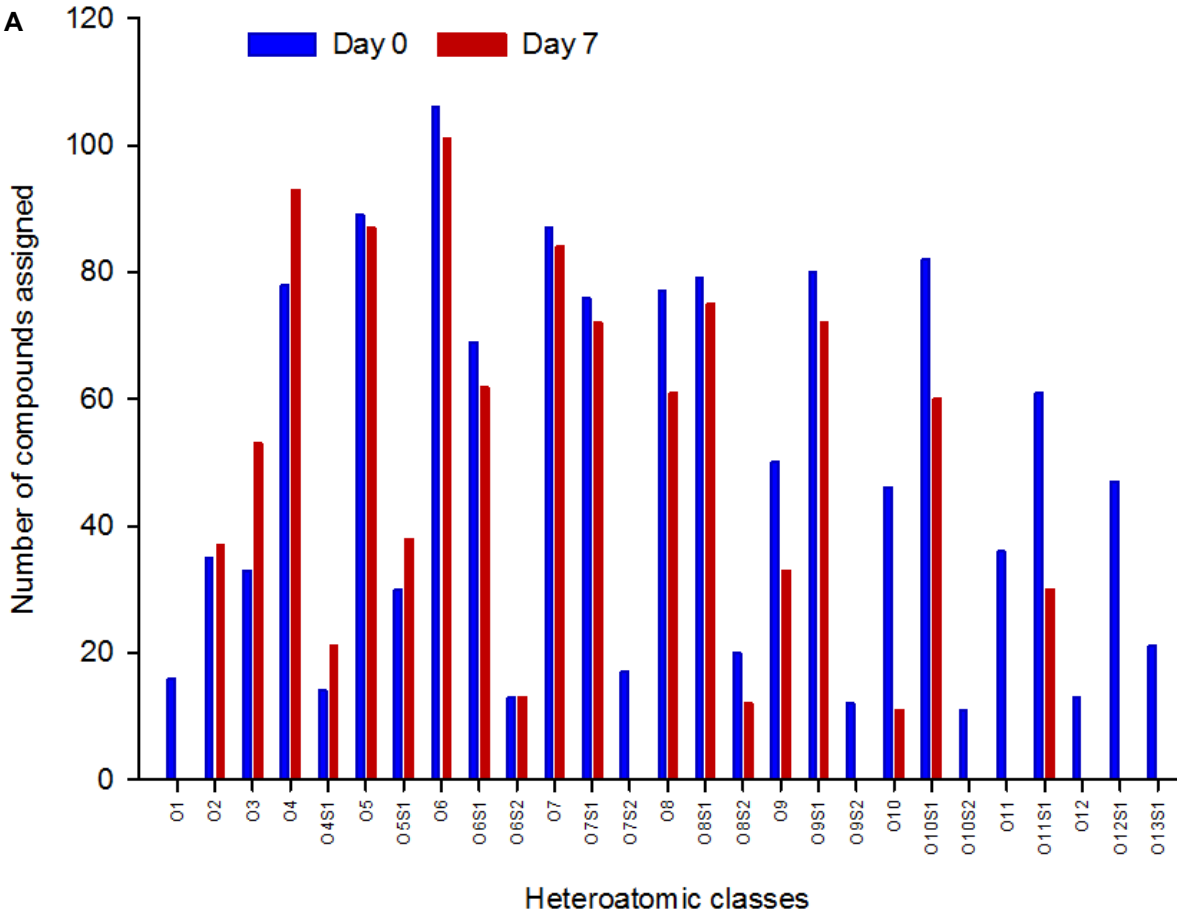

Figure 22a. Comparison of the heteroatomic classes for Kraft lignin treated with laccase only. The figure above shows 27 different heteroatomic classes with some changes observed in the classes of compounds over the 7-day reaction period. There are some groups that do not appear after seven days but further examination of the spectra showed that it was not due a total degradation of these classes of compounds but a low presence of their ions after seven days.

B

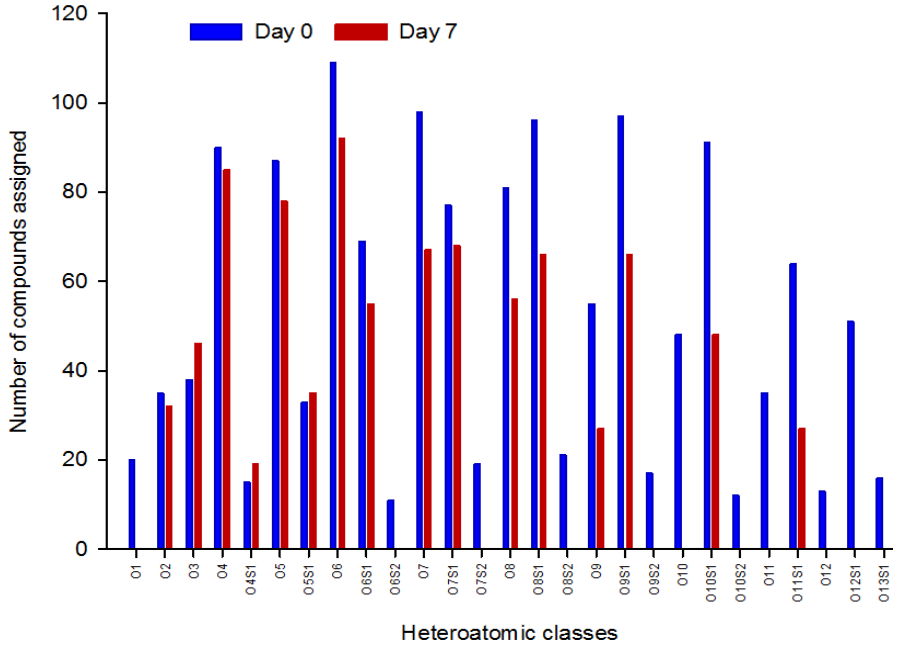

Figure 22b. Comparison of the heteroatomic classes for Kraft lignin treated with laccase and acetosyringone.

The figures above shows 27 different heteroatomic classes with some changes observed in the classes of compounds over the 7-day reaction period. There are some groups that do not appear after seven days but further examination of the spectra showed that it was not due a total degradation of these classes of compounds but a low presence of their ions after seven days. Compared to the laccase alone, the figure shows that there is a higher degree of degradation of the compounds taking place.

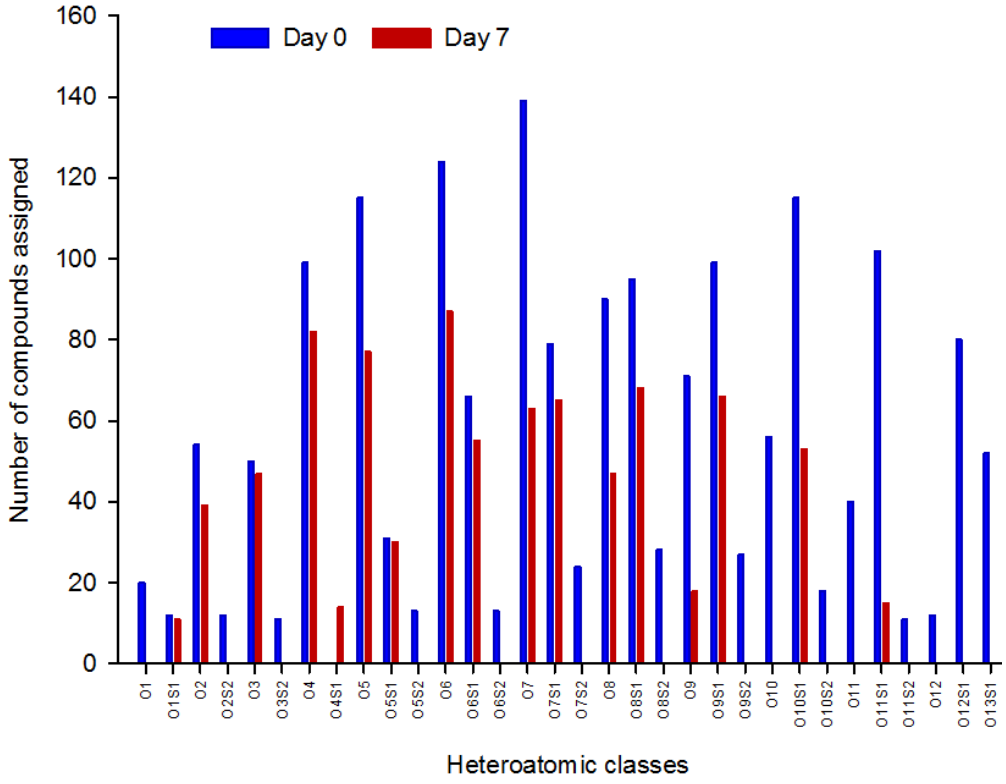

Figure 22c. Comparison of the heteroatomic classes for Kraft lignin treated with laccase and 1-hydroxybenzotriazole (HBT).
The figures above shows 27 different heteroatomic classes with some changes observed in the classes of compounds over the 7-day reaction period. There are some groups that do not appear after seven days and one group (O_4S_1) only present after seven days but further examination of the spectra showed that it was not due a total degradation of these classes of compounds but a low presence of their ions after seven days. Compared to the laccase, the figure shows that there is a higher degree of degradation of the compounds taking place.

(D) Heteroatomic class distribution changes in Kraft lignin treated with *Panus rudis* laccase and guaiacol

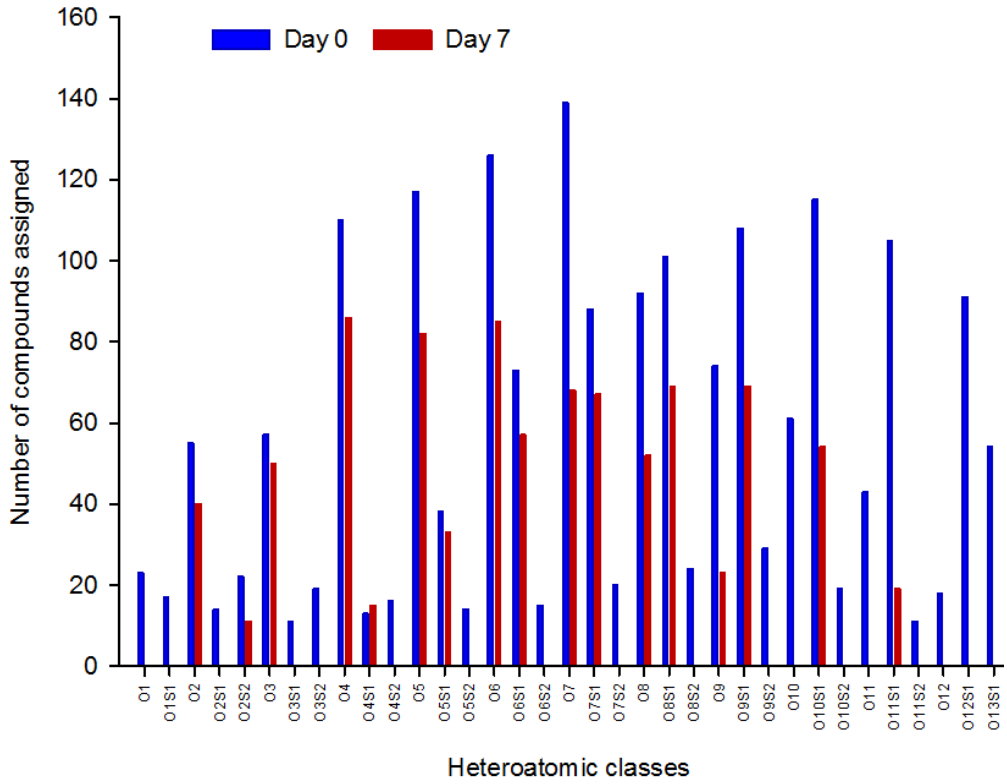

Figure 22d. Comparison of the heteroatomic classes for Kraft lignin treated with laccase and guaiacol.

The figures above shows 27 different heteroatomic classes with some changes observed in the classes of compounds over the 7-day reaction period. There are some groups that do not appear after seven days but further examination of the spectra showed that it was not due a total degradation of these classes of compounds but a low presence of their ions after seven days left them below the cut-off point for the sensitivity of the Data Analysis software (Bruker Daltonics). Compared to the laccase, the figure shows that there is a higher degree of degradation of the compounds taking place.

4.4 Van Krevelen plots of the Kraft lignin degradation products

The van Krevelen plot is a projection onto two axis of each elemental composition in a complex mixture according to their H/C and O/C atomic ratios (Wu, Rodgers and Marshall, 2004). The H/C ratio shows the degree of unsaturation of a compound while the O/C ratio separates according to their oxygen classes (Wu et al., 2004). The van Krevelen plot allows the distribution of the complex mixture components into various compound classes as shown in Figure 23 below.

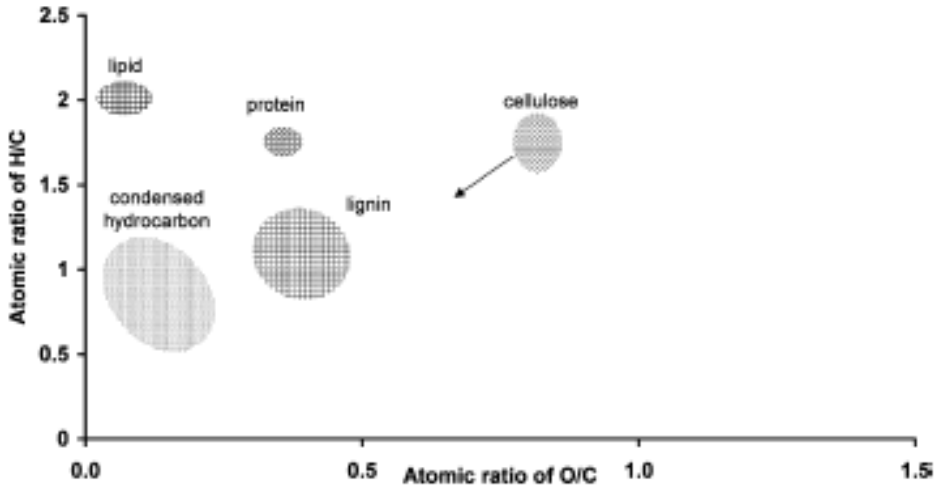

Figure 23. An example of a van Krevelen diagram showing different compound classes (Kim et al., 2003).

The van Krevelen plot for the 7-day lignin degradation reactions are shown in Figures 24a-h

A.

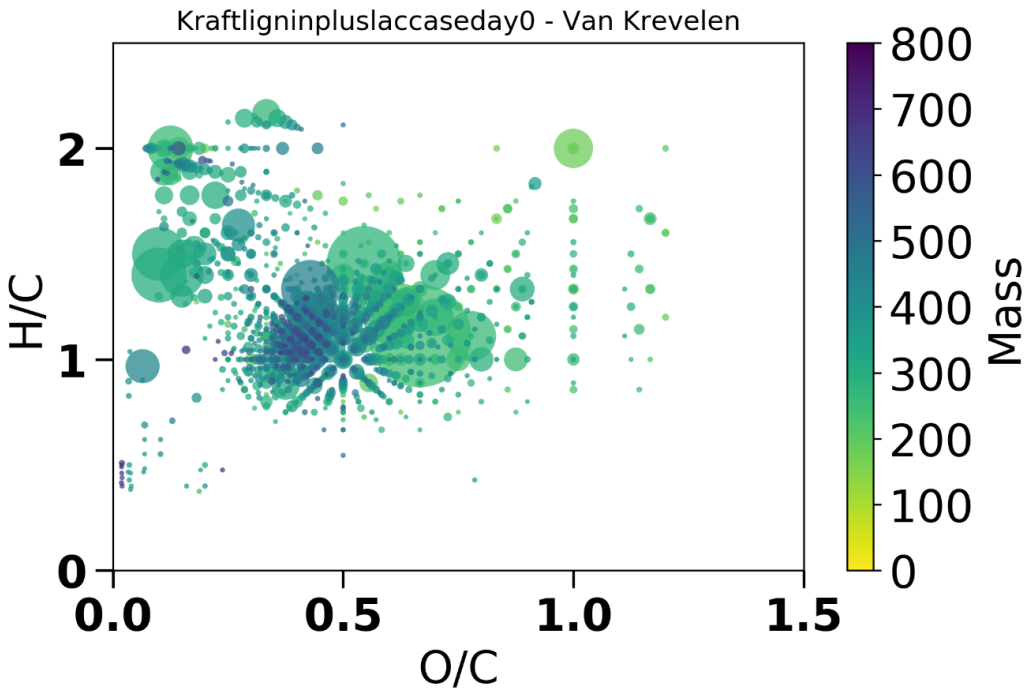

B.

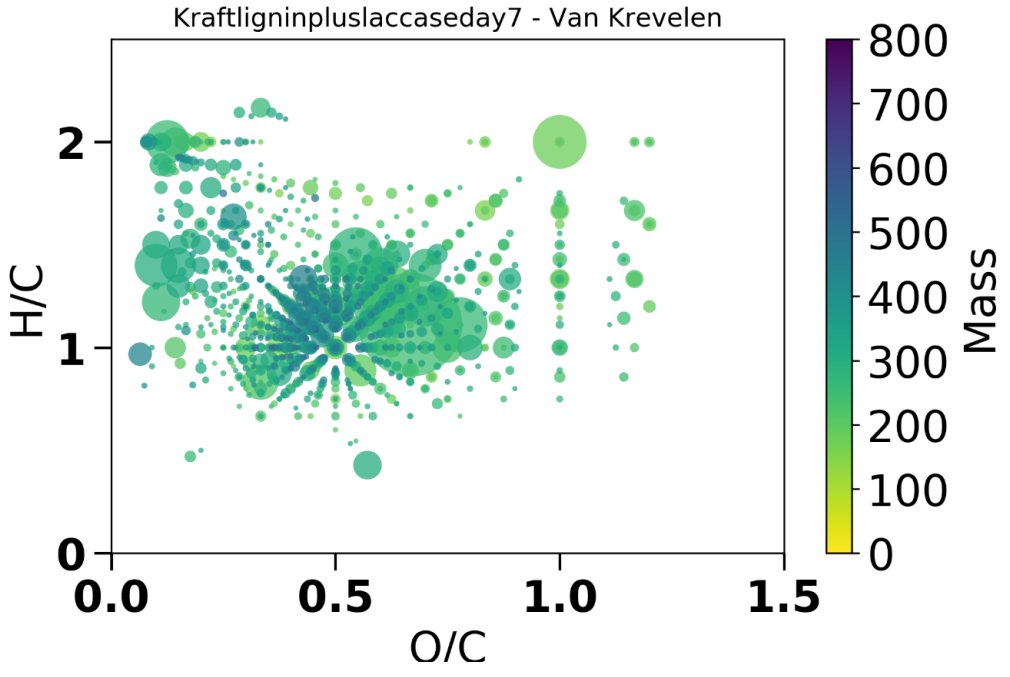

Figure 24(a) and (b). Van Krevelen plot for Kraft lignin degraded by laccase alone.
Figs. 24(a) and (b) above show the van Krevelen plot for Kraft lignin degraded by PrL only at the beginning and end of the 7-day experiment respectively. The lignin region (H/C=0.2-0.6 and O/C=0.7-1.4) of the plot shows a change in the size of the intensity of the circles from the high mass to low mass which could indicate that degradation has taken place. The size of the circles in the plot corresponds to the relative abundance of a particular chemical species in the spectrum.

C.

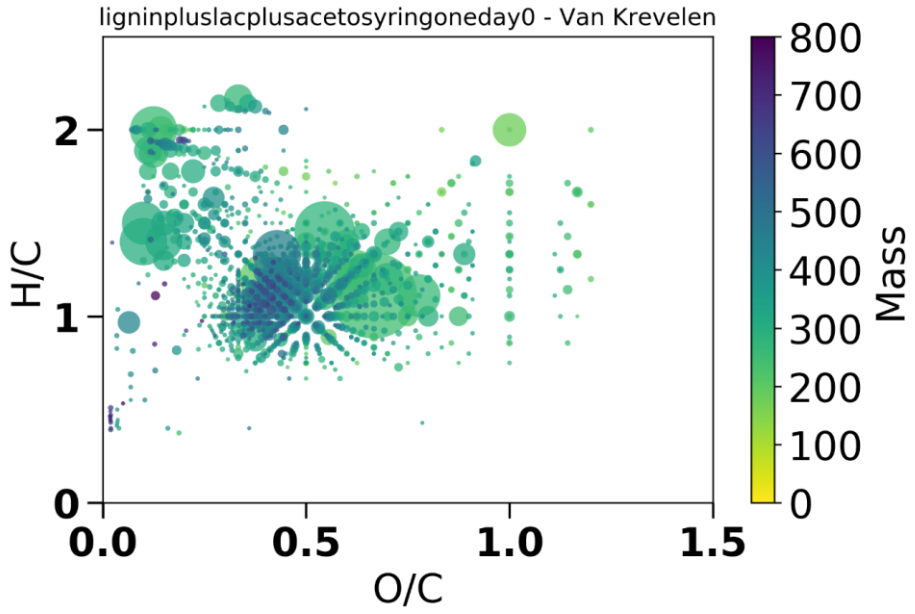

D.

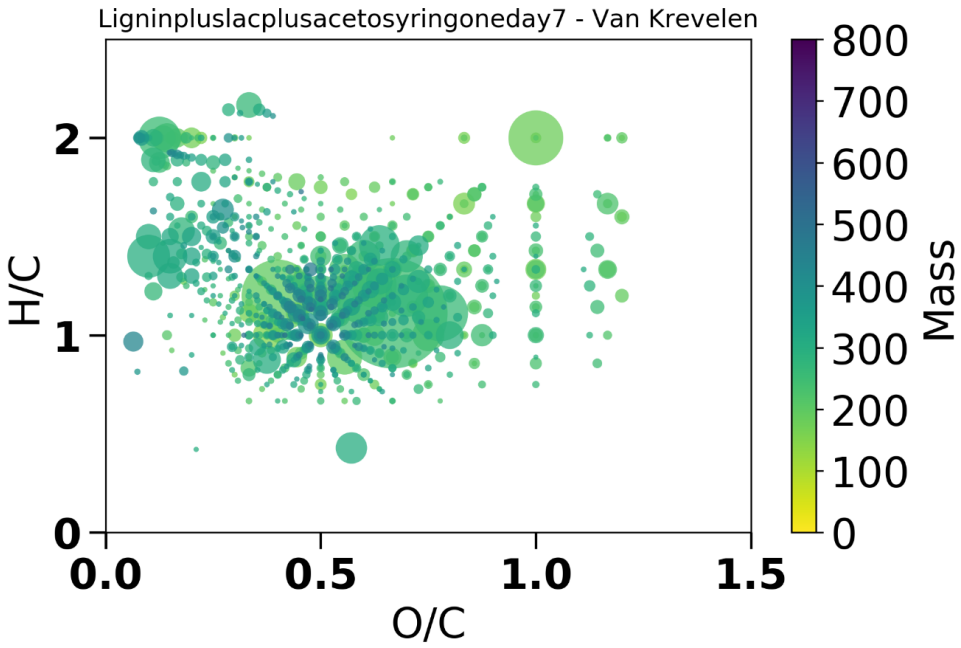

Figure 24(c) and (d). Van Krevelen plot for Kraft lignin degraded by laccase and acetosyringone.

Figs. 24(c) and (d) above show the van krevelen plot for Kraft lignin degraded by PrL and acetosyringone at the beginning and end of the 7-day experiment respectively. The lignin region (H/C=0.2-0.6 and O/C=0.7-1.4) of the plot shows a change in the intensity of the circles from the high mass to low mass which indicate that degradation or a change in the heteroatomic classes present in the media has taken place after the 7-day reaction. The size of the circles in the plot corresponds to the relative abundance of a particular chemical specie in the spectrum.

E.

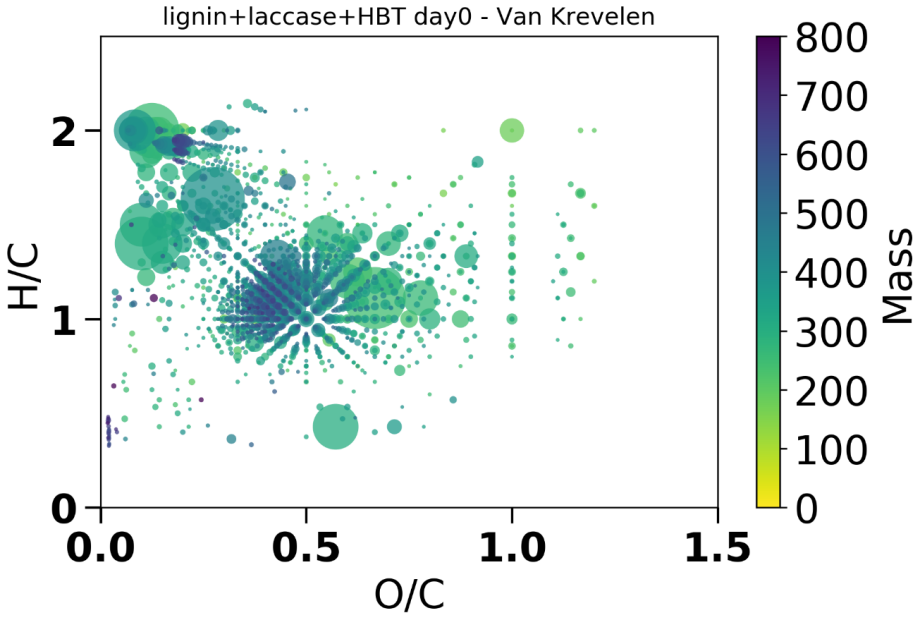

F.

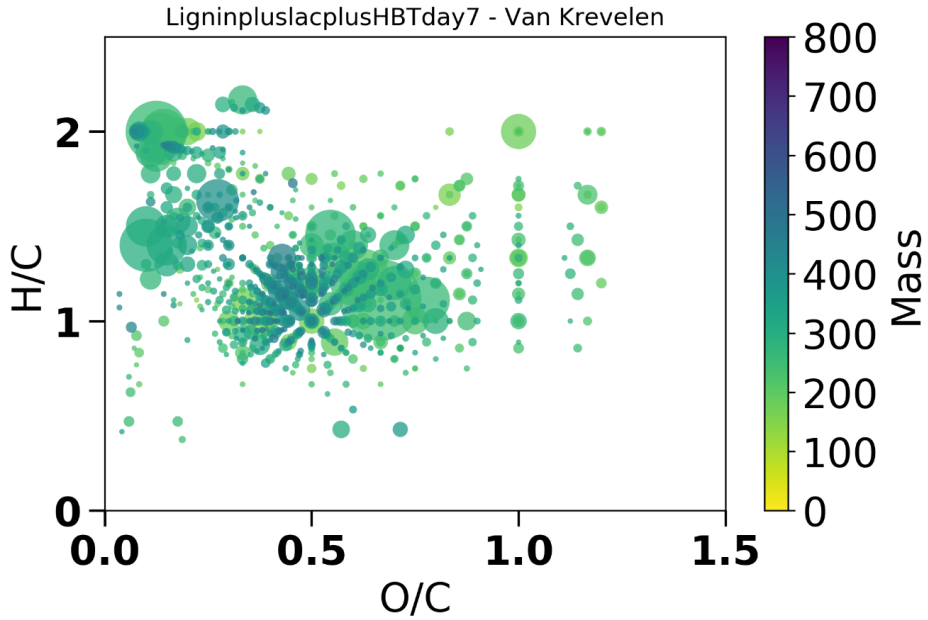

Figure 24(e) and (f). Van Krevelen plot for Kraft lignin degraded by laccase and HBT.
Figs. 24(e) and (f) above show the van krevelen plot for Kraft lignin degraded by PrL and HBT at the beginning and end of the 7-day experiment respectively. The lignin region (H/C=0.2-0.6 and O/C=0.7-1.4) of the plot shows a change in the intensity of the circles from the high mass to low mass which indicate that degradation or a change in the heteroatomic classes present in the media has taken place after the 7-day reaction. The size of the circles in the plot corresponds to the relative abundance of a particular chemical specie in the spectrum.

G.

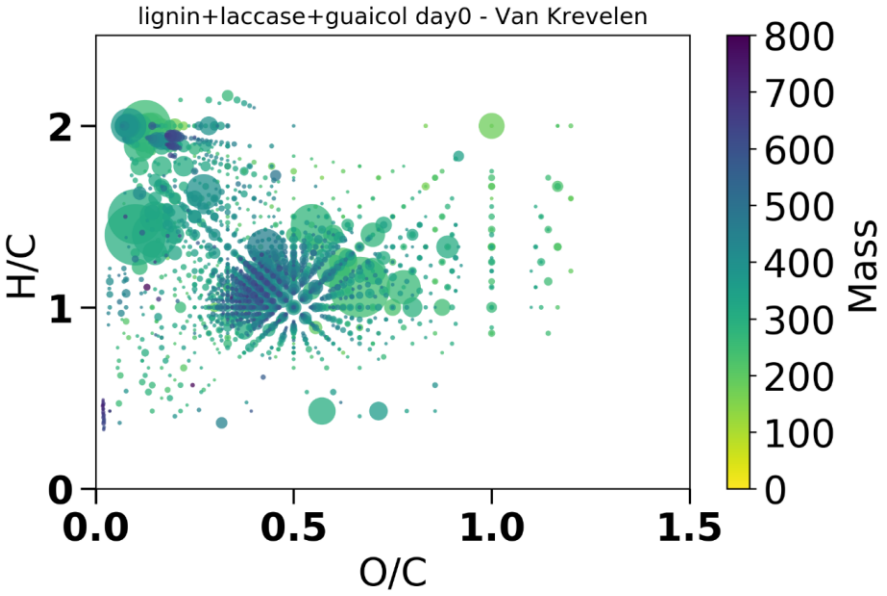

H.

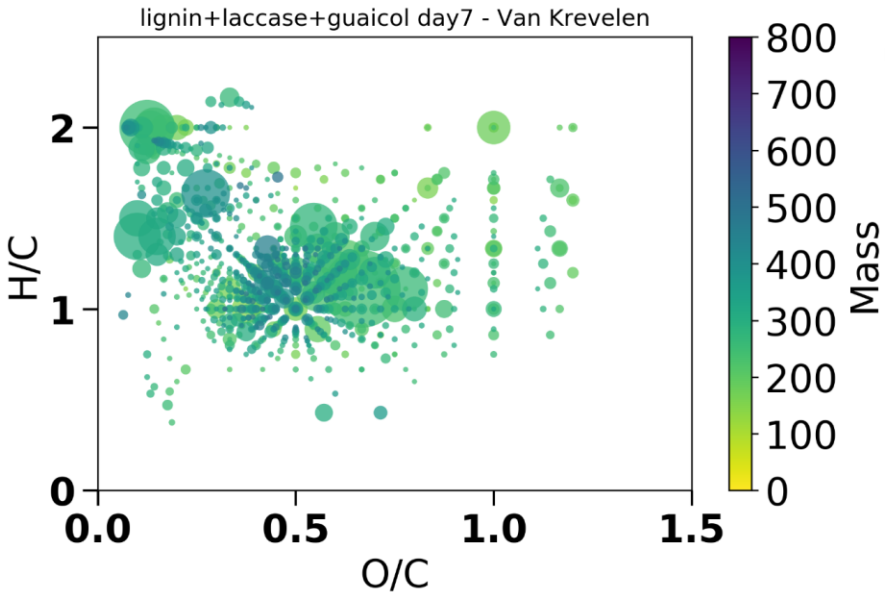

Figure 24(g) and (h). Van Krevelen plot for Kraft lignin degraded by laccase and guaiacol. Figs. 24(g) and (h) above show the van krevelen plot for Kraft lignin degraded by PrL and guaiacol at the beginning and end of the 7-day experiment respectively. The lignin region (H/C=0.2-0.6 and O/C=0.7-1.4) of the plot shows a change in the intensity of the circles from the high mass to low mass which indicate that degradation or a change in the heteroatomic classes present in the media has taken place after the 7-day reaction. The size of the circles in the plot corresponds to the relative abundance of a particular chemical specie in the spectrum.

4.5 Double-Bond Equivalent (DBE) plots of the Kraft lignin degradation products

The double-bond equivalent of a molecule is a measure of the degree of unsaturation or the density of the C-C double bonds in a molecule (Koch and Dittmar, 2006). It is independent of the number of oxygen and sulphur atoms in a molecule and is calculated from the number of atoms and the valencies of the elements present in a molecule (Koch and Dittmar, 2006). The less the number of hydrogen atoms in a molecule, the higher its degree of unsaturation and hence its DBE (Koch and Dittmar, 2006). The DBE plot can provide information about the degree of unsaturation of the compounds within the complex degradation mixture and the changes observed in the 7-day laccase only and laccase-mediated reactions are shown in Figure 25 (a) – (h).

A.

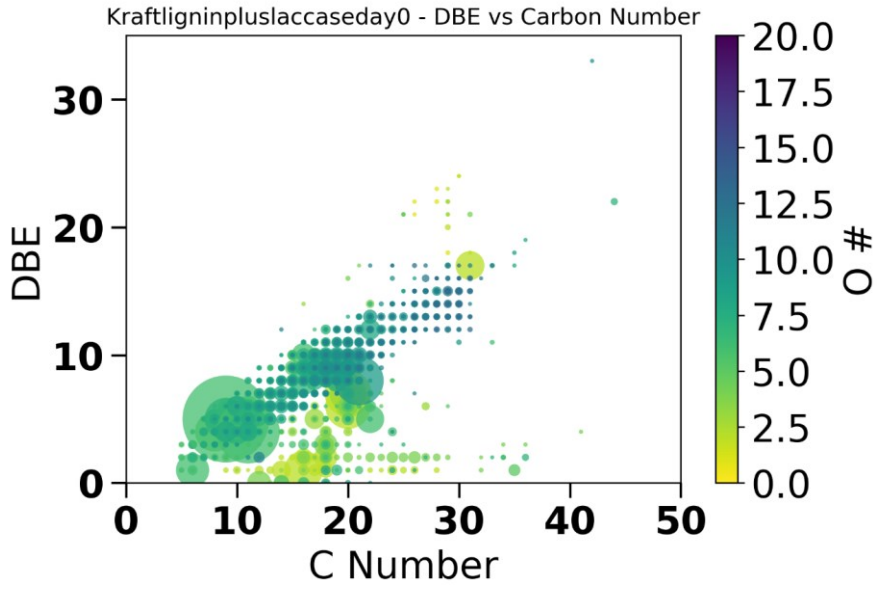

B.

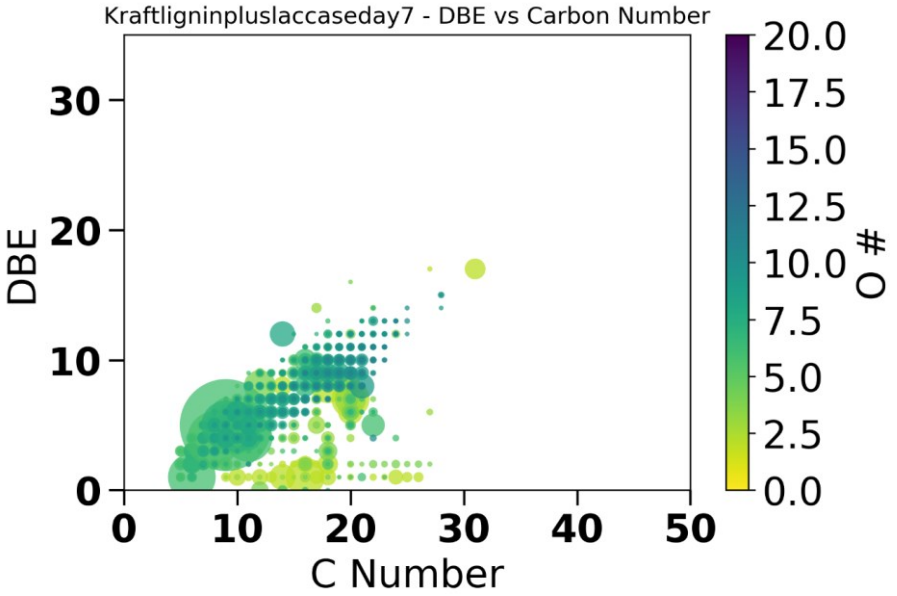

Figures 25 (a) and (b). Double-bond Equivalent plot for Kraft lignin degraded by laccase alone.
The figure above shows the double bond equivalents plotted against number of C atoms at the beginning and end of the 7-day period respectively. The size of the circles indicate the number of oxygen atoms bound to a particular number of C atoms. There is a decrease in the number of carbon atoms which might indicate a degree of degradation.

C.

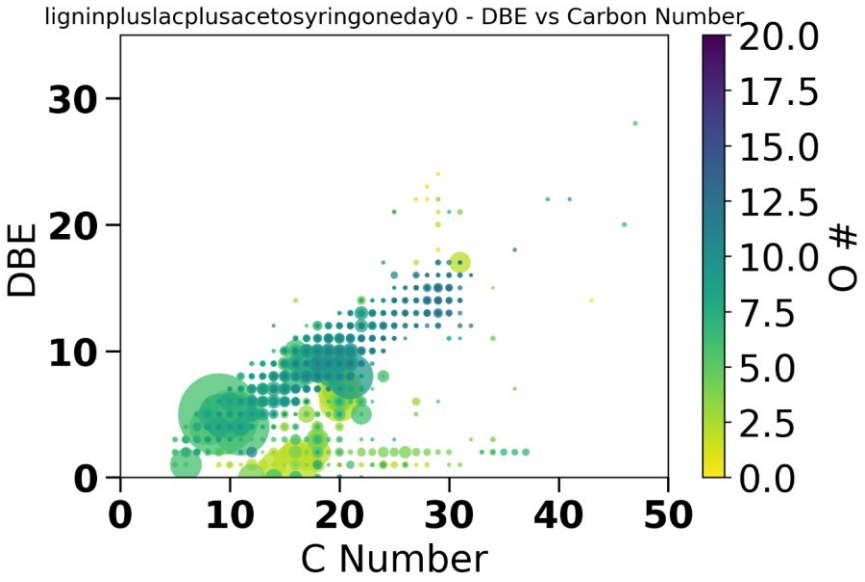

D.

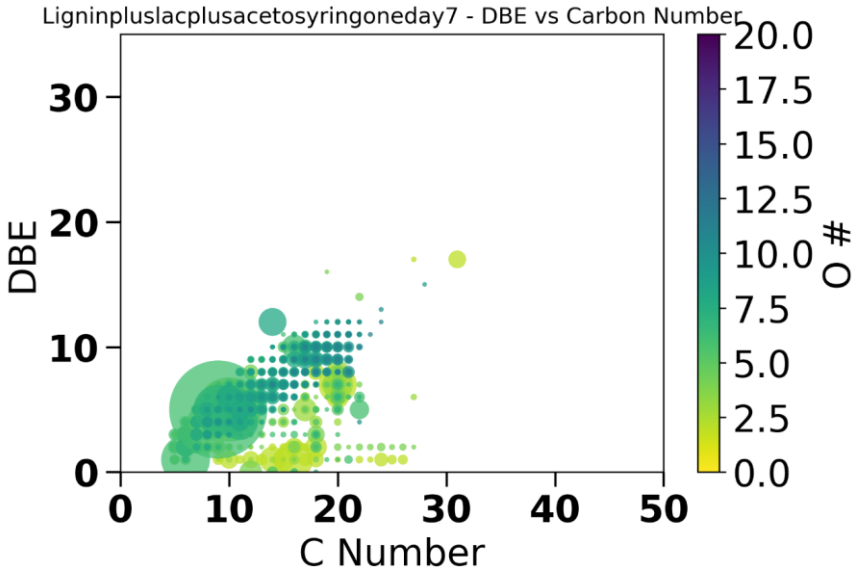

Figures 25 (c) and (d). Double-bond Equivalent plot for Kraft lignin degraded by laccase and acetosyringone.
The figure above shows the double bond equivalents plotted against number of C atoms at the beginning and end of the 7-day period respectively. The size of the circles indicate the number of oxygen atoms bound to a particular number of C atoms. There is a reduction in the number of carbon atoms which might indicate a degree of degradation.

E.

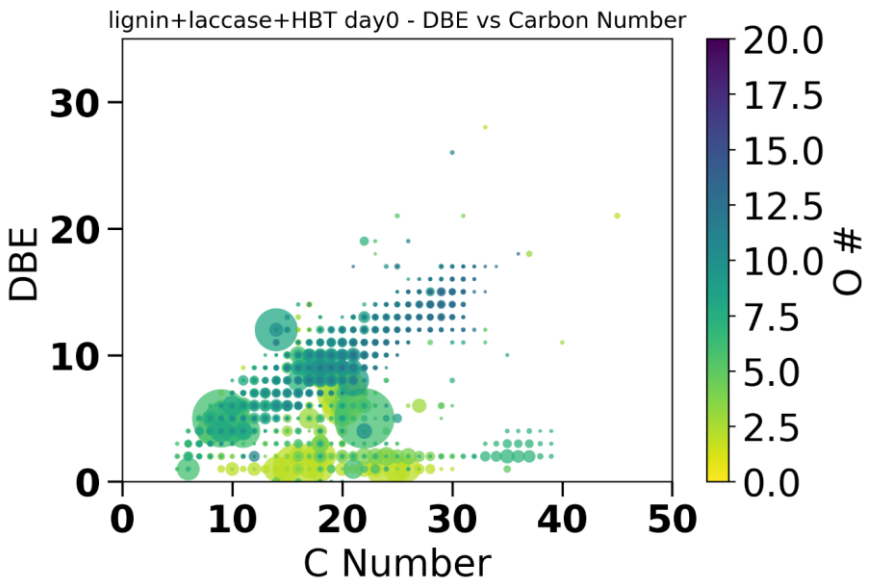

F.

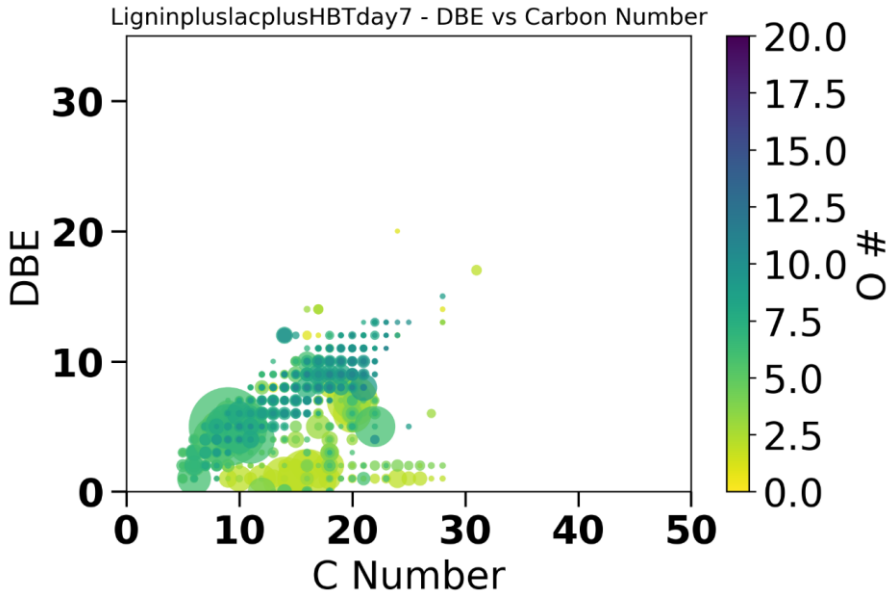

Figures 25 (e) and (f). Double-bond Equivalent plot for Kraft lignin degraded by laccase and HBT.

The figure above shows the double bond equivalents plotted against number of C atoms at the beginning and end of the 7-day period respectively. The size of the circles indicate the number of oxygen atoms bound to a particular number of C atoms. There is a reduction in the number of carbon atoms which might indicate a degree of degradation.

G.

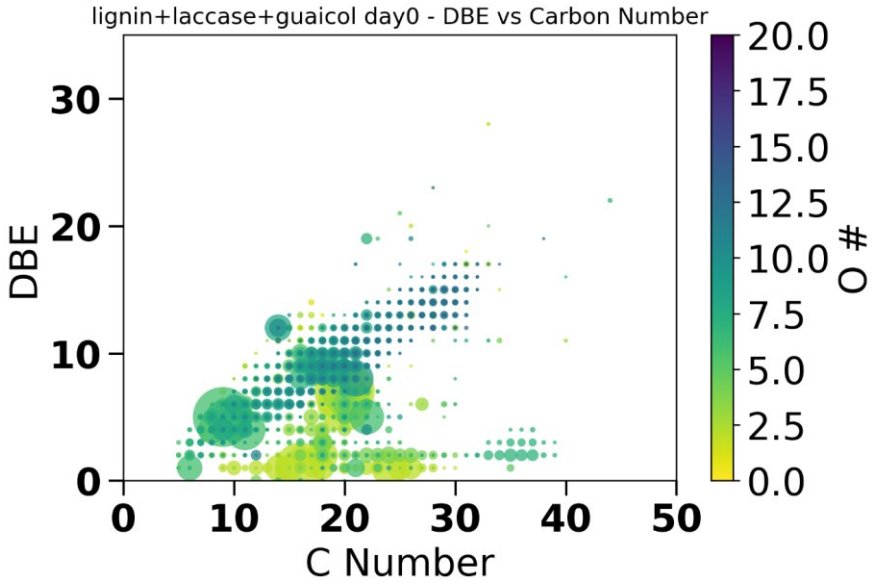

H.

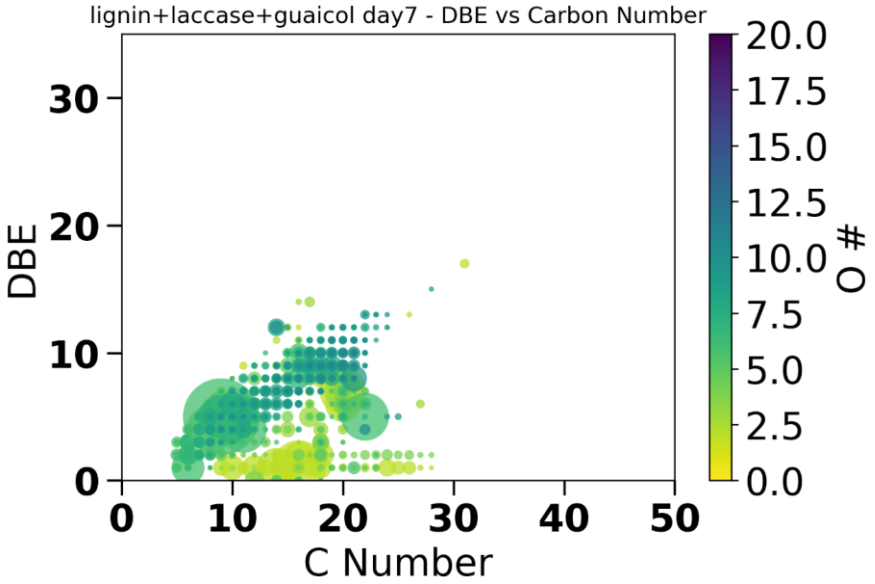

Figures 25 (g) and (h). Double-bond Equivalent plot for Kraft lignin degraded by laccase and guaiacol.

The figure above shows the double bond equivalents plotted against number of C atoms at the beginning and end of the 7-day period respectively. The size of the circles indicate the number of oxygen atoms bound to a particular number of C atoms. There is a reduction in the number of carbon atoms which might indicate a degree of degradation.

4.6 Summary and discussion

The degradation products from the reaction of *Panus rudis* laccase (PrL) and acetosyringone with lignin are numerous and of varying sizes. FT ICR-MS, in the negative ion mode has been chosen in previous studies of similarly complex mixtures, like the degradation product mix in this study, to shed light on their numerous chemical components (Araújo et al., 2005, Sivalingam et al., 2013). By using FT ICR-MS, assigning the peaks in the resulting spectra and then using the FTMS Vis tool which uses the Bokeh Python plotting library (Kew et al., 2017a), the data can be used to generate plots based on heteroatomic classes, double bond equivalent plots and the van Krevelen plots which helps groups the data based on the number of carbon, hydrogen and oxygen atoms that are present within a particular class of degradation products. The van Krevelen plot also enables a quick visualisation of the degradation of the lignin macromolecule as a function of colour intensity in the region corresponding to lignin in the plot.

The heteroatomic plots indicates a general reduction in the overall amounts of majority of the heteroatomic classes particularly in those where the mediator compounds, acetosyringone, HBT and guaiacol have been added to the laccase. This could indicate that the presence of the mediators increases the likelihood of depolymerisation of the lignin polymer and inhibits re-polymerisation. The overall trend towards degradation is also confirmed by the DBE plots, where there is a decrease in the carbon number of the species in the degradation products present after the 7-day reaction compared to the initial reaction period but it is not clear from the DBE plots which mediator was most effective in the degradation process. The van Krevelen plots of all the degradation plots and these clearly shows that in the region of the plot corresponding to lignin (H/C = 0.2-0.6 and O/C = 0.7-1.4), there is a decrease in the mass of the lignin species present over the 7-day period, as indicated by the colour intensity

and an examination of the individual species showed that new chemical species had been generated during the degradation process.

Although FT ICR-MS is very good for identifying chemical formulae of complex mixtures, but there is an inability to correctly determine the structural formulae of the chemical compounds identified (Kew et al., 2017b) , hence the inability to produce such a list from this study.

Chapter 5: Structural determination of *Bacillus subtilis* dye-decolorizing peroxidase (BsDyp) and *Pseudomonas putida* MET94 dye-decolorizing peroxidase (PpDyp) using X-ray crystallography

5.1 Introduction

Bacillus subtilis and *Pseudomonas putida* MET94 dye-decolorizing peroxidases, are peroxidases of the classes A and B of the dye-decolorizing peroxidase (Dyp) family of enzymes (Santos et al., 2014). About 1 ml of both enzymes in purified form, as well as the plasmid constructs labelled pRC1 and pRC-2 were gifts from Professor Ligia O. Martins' lab at the New University of Lisbon, for X-ray crystallisation to determine their three-dimensional structure, and to elucidate the residues responsible for any similarities and differences in their enzyme activities. They were discovered by BLAST searches of their respective organisms of origin, initiated by the template sequences from the crystal structures of several bacterial dye decolorizing peroxidases in the protein databank (Santos et al., 2014). Their sequences were cloned into pET-21a (+) to yield the plasmids pRC-1 and pRC-2 and expressed in E.coli BL21 (DE3) and BL21 star (DE3) competent cells (Novagen) under the promoter T7*lac* (Santos et al., 2014). Both enzymes needed the addition of 0.1 mM IPTG and 15 μM hemin for proper expression, and pure enzymes were obtained via a 3-stage purification process of two ion exchange steps followed by size exclusion chromatography (Santos et al., 2014).

5.2 *Pseudomonas putida* MET 94 dye-decolorizing peroxidase (PpDyp)

PpDyp shares a 30% sequence identity with the dye-decolourising peroxidase YfeX (PDB ID: 5GT2) from *Escherichia coli* O157 (Liu et al., 2017). YfeX, like PpDyp is located in the cytoplasm, as it lacks any of the signal peptides associated with being translocated to the periplasm or out of the cell (Liu et al., 2017, Santos et al., 2014). The reason for the cellular localisation of dye-decolourising peroxidases, as well as how this affects their activities and

influences their substrate preferences are not well understood. PpDyp is a diverse enzyme in terms of substrates which would suggest potentially important industrial uses for it (Santos et al., 2014). The most important use of oxidative enzymes in industry is in bio-transformations and potential target chemicals that could be synthesised by PpDyp could be modified lignins, diols, α-naphthol, drug metabolites, polyaniline, modified cellulosic fibres, cyclic ketones, epoxides, catechol, 2,5-diaminobenzene sulphonic acid (DABSA) polymer, chiral alcohols and 2,5-furandicarboxylic acid (FDCA) (Martínez et al., 2017). A structural investigation into this enzyme could be useful in determining the functionally important amino acid residues, and explain how it is able to oxidise so many substrates, as well as which of its residues would be most suitable to mutate to target them towards breaking down specific bonds within the lignin polymer and also making them more suitable for industrial use.

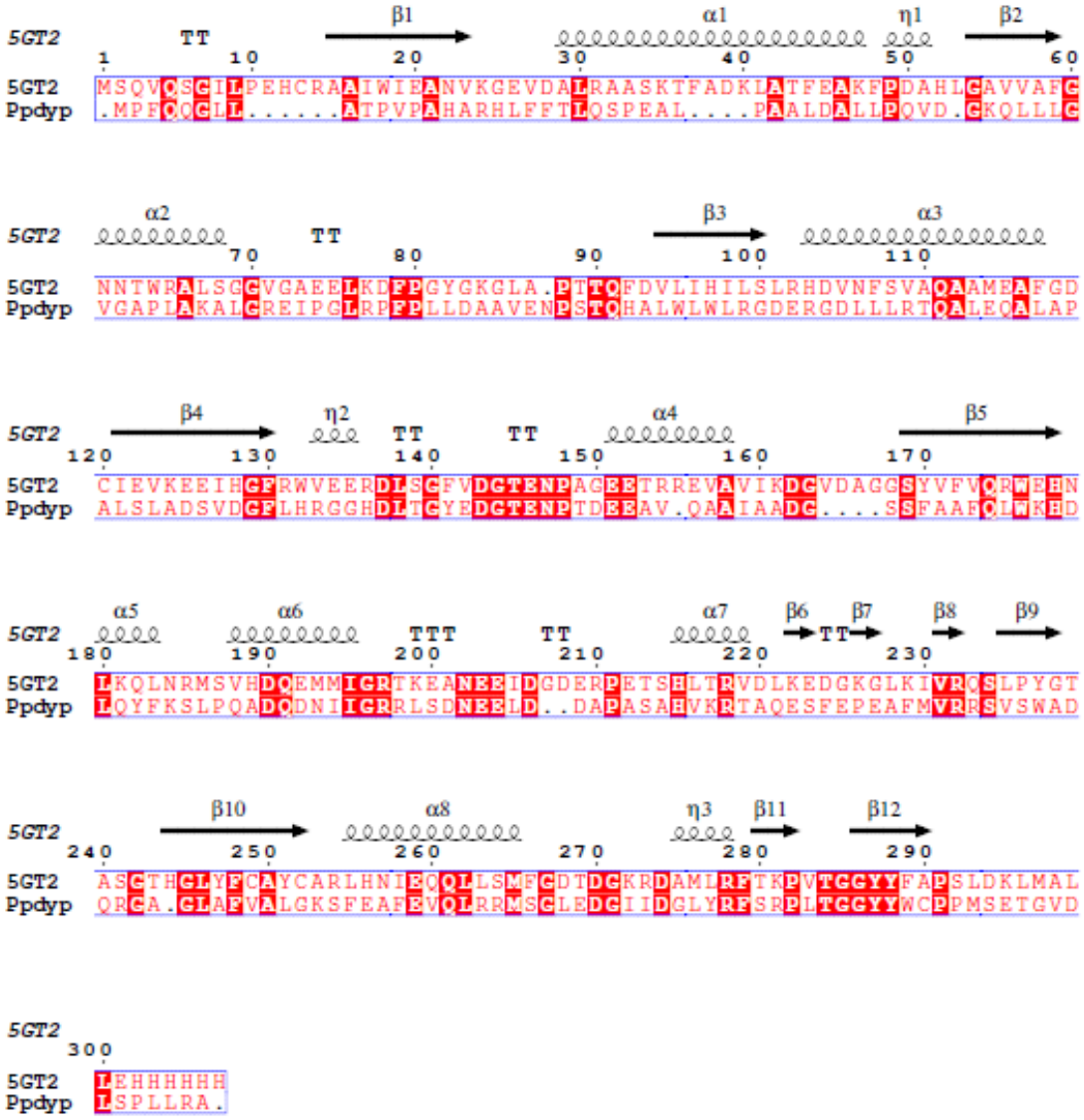

Figure 26. Sequence alignment of the PpDyp with *Escherichia coli O157* YfeX.
Pseudomonas putida MET94 dye-decolorising peroxidase, PpDyp was aligned with the *Escherichia coli* O157 dye-decolorising peroxidase, YfeX (PDB ID: 5GT2). The alignment was performed using Multalin (Corpet, 1988) and the output displayed as an ESPript 3.0 file (Robert and Gouet, 2014). The output file shows the consensus sequences shaded in red boxes and shows the various secondary structural elements present in the YfeX structure: eight α-helices, twelve β-strands, three 3_{10}-helices (η), six strict β-turns (TT) and one strict α-turn (TTT), on top of each row in the alignment. PpDyp is made up of 287 amino acids and has a molecular weight of approximately 31.3 KDa and an isoelectric point (pI) of 4.82 as determined by Protparam (Gasteiger et al., 2003)

5.3 Crystallisation and structural determination of *Pseudomonas putida* MET 94 dye-decolourising peroxidase (PpDyp)

5.3.1 Screening for initial crystallisation conditions

The purified PpDyp obtained from Professor Ligia's laboratory was subjected to crystallisation trials at a concentration of 26.1 mg/ml. I adjusted its concentration to concentration of 10 mg/ml using Tris buffer and set up crystallisation trays using the sitting drop vapour diffusion method on a nanoscale (100 nanolitres). Only two of the screens, JCSG and PEG/Ion were conducive for the formation of crystals of PpDyp. The crystals observed on the initial screening plates are shown in Figure 27 below.

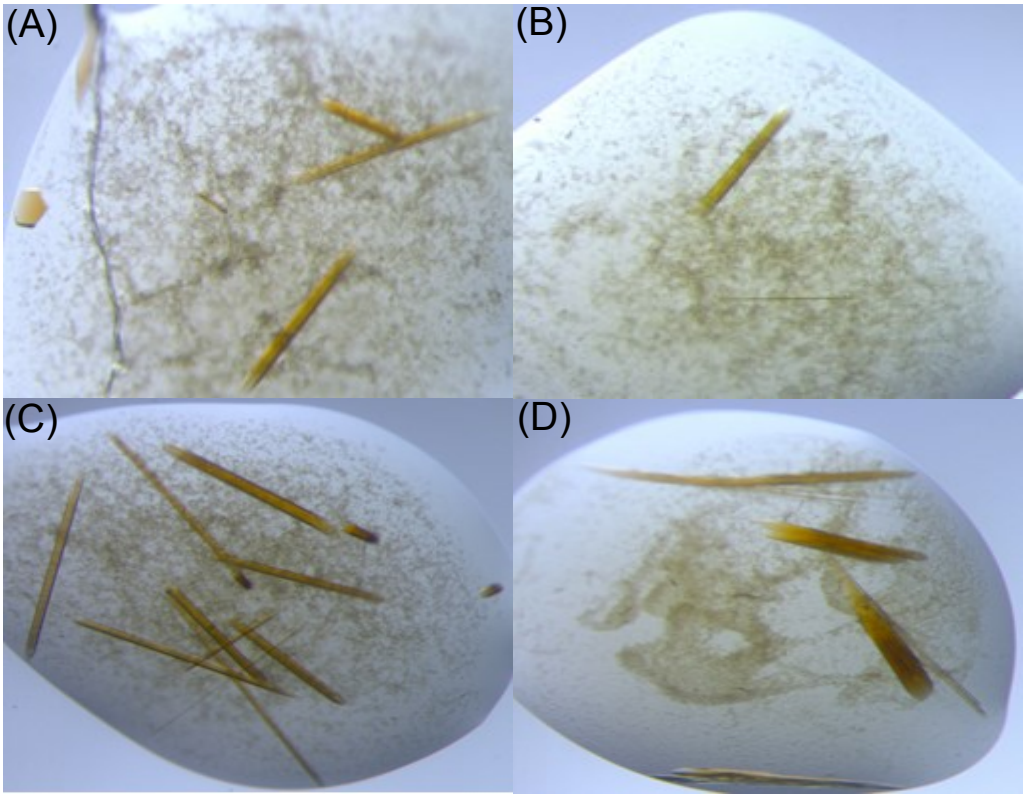

Figure 27. Crystals from initial screening plates of PpDyp.
These are the crystals observed within the hanging drops suspended above different well solutions. The purified PpDyp (100 or 200 nanolitres) was added to the salt droplets on cover slips next to a 100 nl well solution of a specific salt solution in a 96 well plate. Four commercial screens; JCSG-plus (Molecular Dimensions), PEG/Ion (Hampton), Structure screen 1 & 2 and MIDAS (Molecular Dimensions) were used. The crystals above are as follows: (A) PEG/Ion A5 – 0.2 M magnesium chloride hexahydrate, 20% w/v PEG 3,350, pH 5.9; (B) PEG/Ion B8 – 0.2 M magnesium formate dihydrate, 20% w/v PEG 3,350, pH 7.0; (C) PEG/Ion C1 - 0.2 M magnesium acetate tetrahydrate, 20% w/v PEG 3,350, pH 7.9 and (D) JCSG E11 – 0.16 M calcium acetate, 0.08 M sodium cacodylate, 14.4% w/v PEG 8,000 and 20% v/v glycerol, pH 6.5. The plates were viewed under the Leica M 205 C stereo microscope and the crystals were observed after 72 hours. The conditions under which they appeared were recorded and used in setting up optimisation plates and the resulting crystals are shown in Figure 5.3.2 below. The crystals exhibit a brownish appearance due to presence of haem iron in purified PpDyp and are mostly needle-shaped. There was also a hexagonal (edge of drop A) crystal as well. The crystals were all quite fragile and had a tendency to fragment whenever an attempt was made to collect them for data collection.

5.3.2 Optimisation and initial structural determination attempts

Optimisations of the conditions observed during initial screening were set up using the hanging-drop vapour method manually, using 24-well Linbro tissue culture plates with well solutions increased to 1 ml and droplet solution increased to 1 μl. I did this to promote the formation of bigger and more stable crystals of PpDyp. The initial screen showed that a combination of various magnesium and calcium salts, together with polymers such as PEG 3,350 and 8,000, resulted in the formation of PpDyp crystals and the optimisation was performed by varying these initial conditions in terms of pH of final solution and also changing the percentage composition of either the PEG or the salt or both in the final well solution. The drops with successful crystal growth are shown in Figure 28 and a summary of all the conditions are shown in Table **5.3.1**. I harvested the crystals from the drops in which they were present using a mounted nylon loop (Molecular Dimensions), quickly transferred to a cryo-protectant solution (containing all of the components of the particular well solution a crystal was growing in, plus 20% PEG 200), and flash-cooled in liquid nitrogen). The major purpose of the cryoprotectant is to prevent the formation of ice crystals within the crystal of interest. The ice crystals could either physically damage the crystal we are interested in, or obscure diffraction information, corresponding to resolution ranges around the secondary structure elements in the crystallographic datasets of the crystals of interest. The crystals were transferred via uni-pucs to the Diamond Light Source (Didcot, UK) and multiple datasets were collected on the beamline, I04-1. The images collected showed multiple overlapping crystal lattices with high levels of anisotropy in the diffraction pattern as the crystal was rotated in the beam. The best dataset collected diffracted to only 3.3 Å resolution and it was not possible to determine the phases by molecular replacement.

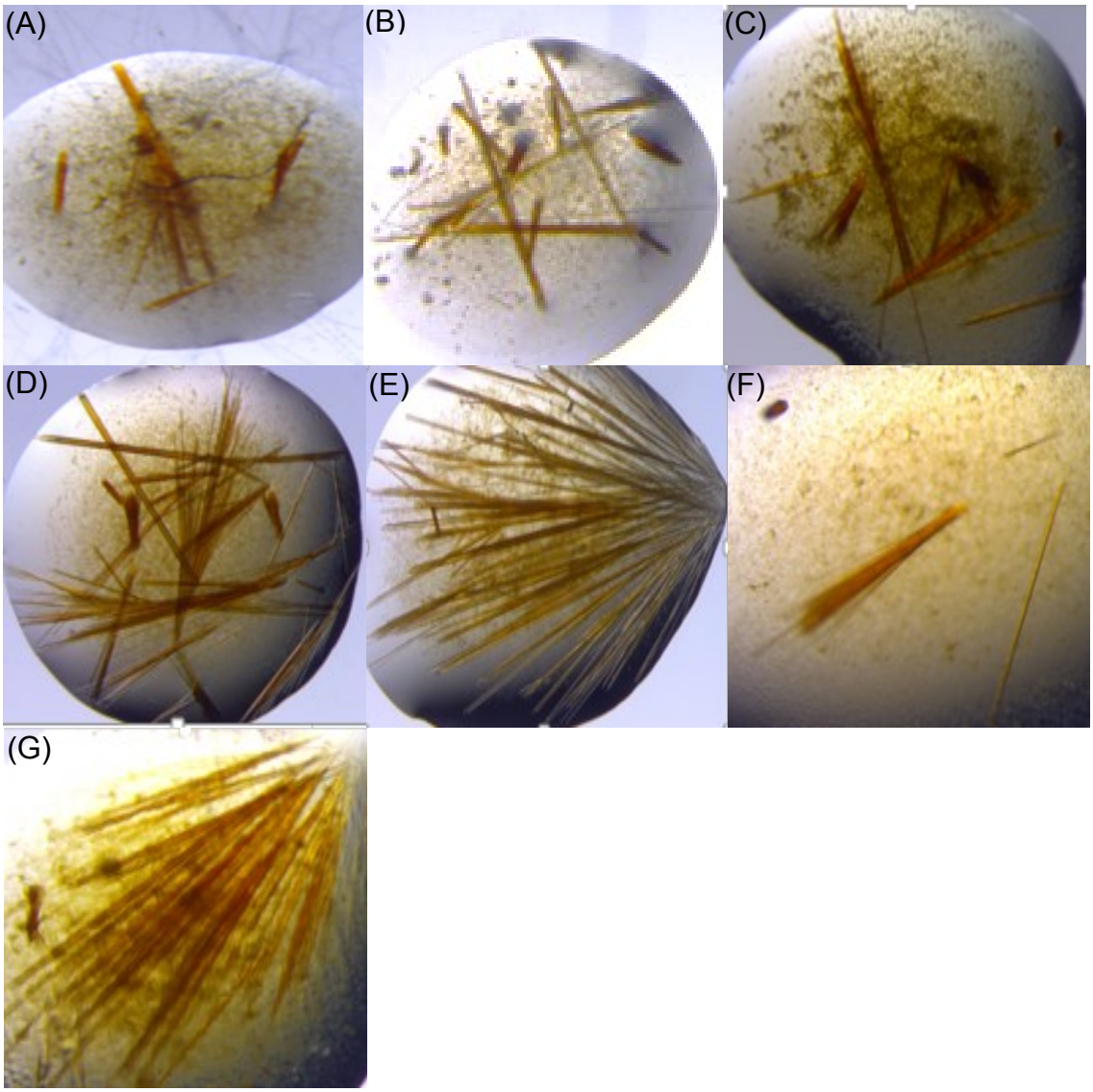

Figure 28. Crystals from the optimisation plates of PpDyp.
These are the crystals observed within the drops of the surface of the optimisation plates that had been set up based on the results obtained in Figure 27. The crystals are still the same brown colour (due to haem iron) and the same needle shape as in the screening plates in Figure 27**.** Although the optimisation plates are set up in bigger drops, the majority of the crystals are thinner and grow out of a similar point of origin, a phenomenon known as twinning. Twinning produces crystals that are of poor quality for gathering structural data on a protein via X-ray crystallography. The crystals were also all very fragile and broke up very easily with the most minimal of contact or agitation.

Table 5.3.1. Summary of the crystallisation conditions of PpDyp. Except where stated, the pH was adjusted with either HCl or NaOH depending on pH of the initial well solution.

SCREENING PLATES	**SALT**	**POLYMER**	**pH**
A	0.2 M magnesium chloride hexahydrate	20% w/v PEG 3,350	5.9
B	0.2 M magnesium formate dihydrate	20% w/v PEG 3,350	7.0
C	0.2 M magnesium acetate tetrahydrate	20% w/v PEG 3,350	7.9
D	0.16 M calcium acetate,pH adjusted to 6.5 with 0.08 M sodium cacodylate	14.4% w/v PEG 8K/20% v/v glycerol	6.5
OPTIMISATION PLATES	**SALT**	**POLYMER**	**pH**
A	0.2 M magnesium chloride hexahydrate	10% w/v PEG 3,350	5.9
B	0.2 M magnesium chloride hexahydrate	10% w/v PEG 3,350	5.9
C	0.2 M magnesium chloride hexahydrate	10% w/v PEG 3,350	5.9
D	0.2 M magnesium chloride hexahydrate	10% w/v PEG 3,350	7.0. The pH was adjusted to 7.0 with HEPES
E	0.25 M magnesium chloride hexahydrate	10% w/v PEG 3,350	5.0. The pH was adjusted to 5.0 with MES.
F	0.25 M magnesium chloride hexahydrate	10% w/v PEG 3,350	5.9
G	0.15 M magnesium formate dihydrate	15% w/v PEG 3,350	7.0

5.3.3 Selenomethionine (Se-Met) labelling of PpDyp

Incorporation of selenomethionine (Se-Met) into proteins to replace their normal methionine residues is a widely used technique for improving structure determination of proteins (Kelly, Graham and Owen, 2016). The Se-Met serves to aid phasing by providing a heavy atom with sufficient anomalous X-ray scattering at synchrotron radiation wavelengths to allow experimental phasing of the data, while preserving the structural integrity of the protein (Rupp, 2010). PpDyp is composed of 286 amino acids and has a molecular weight of approximately 32 KDa, an isoelectric point (pI) of 4.82 and it possesses four methionine residues which would be substituted by Se-Met (Gasteiger et al., 2003, Santos et al., 2014). I labelled PpDyp with Se-Met and purified it via a three-step purification strategy which involved two ion exchange steps, followed by a size exclusion chromatography (SEC) step. The first step in the purification was an anion exchange chromatography (AEC) process, done by passing the crude cell extract through a 10 ml Q Sepharose™ Fast Flow column (GE Healthcare Life Sciences). Figure 29 shows the purification trace (a) and the SDS-PAGE gel (b) of this process.

(A)

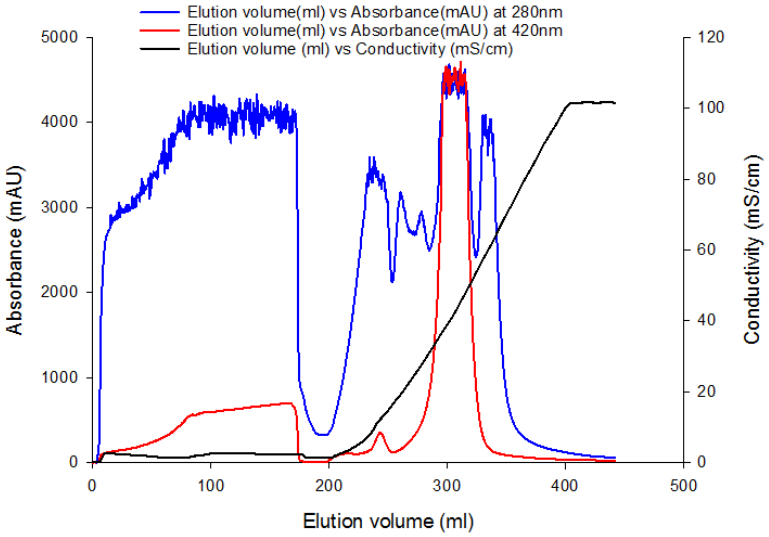

(B)

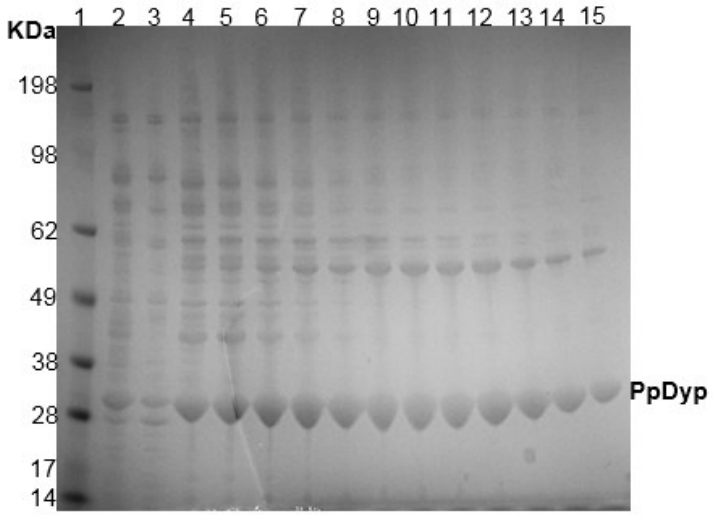

Figure 29. Q Sepharose™ Fast Flow purification chromatogram of PpDyp.
The purification trace shown in (A) shows the absorbance at 280 nm which monitors the presence of protein in the eluted fractions and the absorbance at 420 nm which monitors the presence of the Fe^{3+} at the haem centre of the PpDyp. The conductivity on the right hand y-axis corresponds to the linear gradient from 0 – 1 M NaCl that was used to elute the Se-Met labelled PpDyp. The fractions of PpDyp collected over 20 column volumes. SDS-PAGE was carried out to visualise the collected fractions. Lane 1 had SeeBlue™ Plus2 pre-stained protein standard, lane 2 was loaded with the original extract of the cell extract of the PpDyp applied to the column, lane 3 represented the flow-through from the purification run that had never bound to the column and had come off during the washing step, while lanes 4-15 were loaded with fractions that were eluted before, at the centre, and just after the rough peak around 300 ml on the elution volume axis. These were very bright red fractions. The PpDyp label on the right y-axis corresponds to the approximately 32 KDa size of the PpDyp being purified.

The fractions with the PpDyp, determined by the points in the chromatogram in Figure 29 where the absorbances at 280 nm and 420 nm merge and the presence of bands on SDS-PAGE at approximately 32 KDa for these fractions, showed the incorporation of Fe^{3+} from the hemin into the active site of the PpDyp. These fractions were pooled, desalted and applied

to a GE 6 ml Resource™ Q (GE) column, a second anion exchange column and the chromatograph and SDS-PAGE gel is shown in Figure 30 below.

(A)

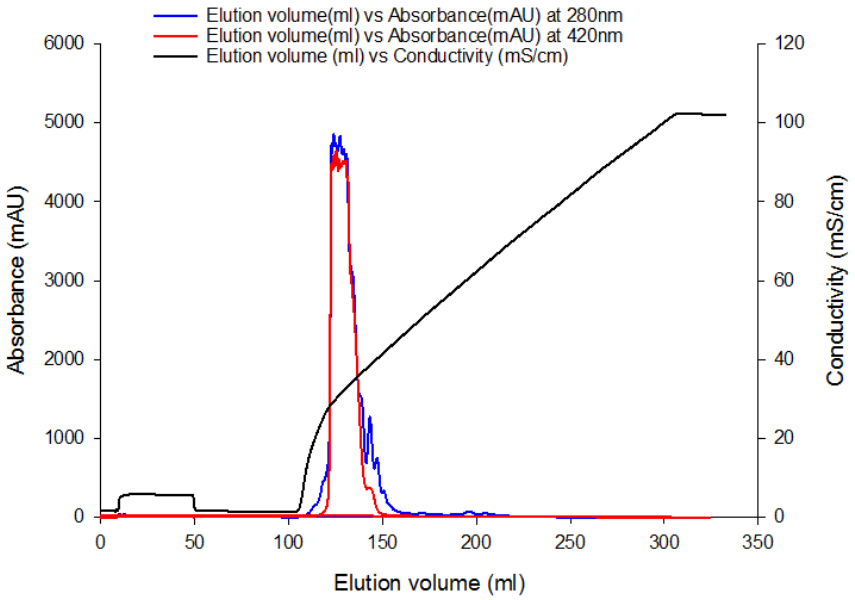

(B)

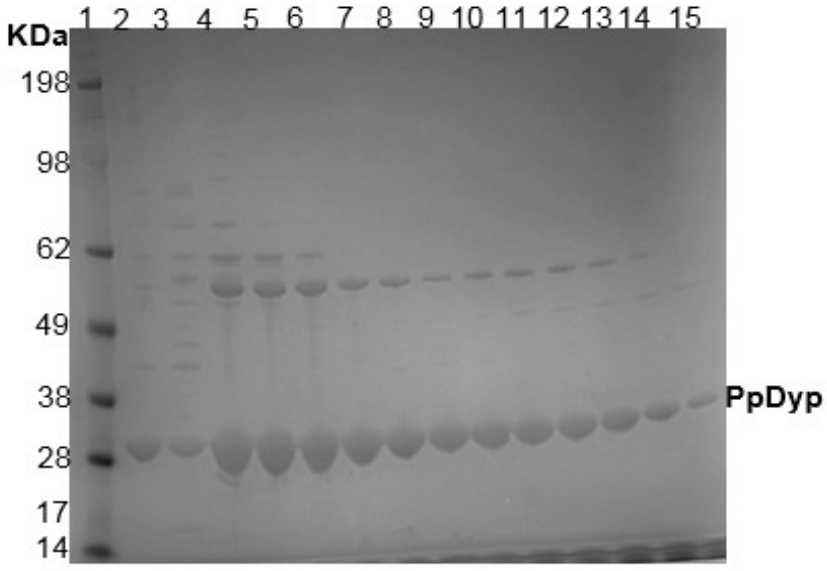

Figure 30. Resource™ Q purification chromatograph of PpDyp.
The purification trace shown in (A) shows the absorbance at 280 nm which monitors the presence of protein in the eluted fractions and the absorbance at 420 nm which monitors the presence of the Fe^{3+} at the haem centre of the PpDyp. The conductivity on the right hand y-axis corresponds to the linear gradient from 0 – 1 M NaCl that was used to elute the Se-Met labelled PpDyp. The fractions of PpDyp collected over 20 column volumes. SDS-PAGE was carried out to visualise the collected fractions. Lane 1 had SeeBlue™ Plus2 pre-stained protein standard, lane 2 was loaded with the pooled and desalted fraction of the Se-Met applied to the Resource™ Q column, lane 3 represented the flow-through from the purification run, while lanes 4 – 15 were loaded with fractions that were eluted before, at the centre, and just after the rough peak around 130 ml on the elution volume axis.The PpDyp label on the right y-axis corresponds to the approximately 32 KDa size of the PpDyp being purified. The gels showed fewer species when compared to that in **Fig 29** indicating increased purity of the PpDyp sample.

After the second ion exchange chromatography (IEC) step with the Resource™ Q (GE) column, the PpDyp fractions as determined from both the purification chromatogram and the SDS-PAGE gel, pooled, buffer-exchanged, and concentrated to a final volume of 1.5 ml before being applied to a HiLoad Superdex 200 pg 16/60 column (GE) for a size exclusion chromatography, which is the final polishing step of the purification (Figure 31).

(A)

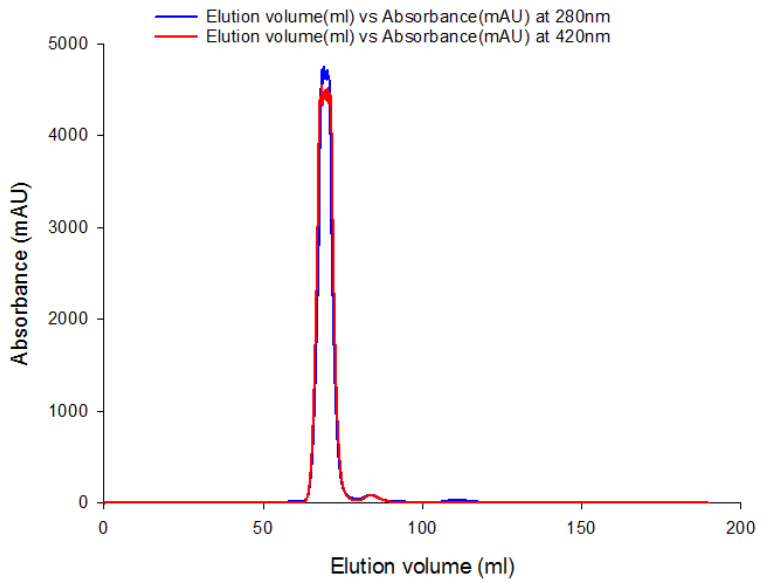

(B)

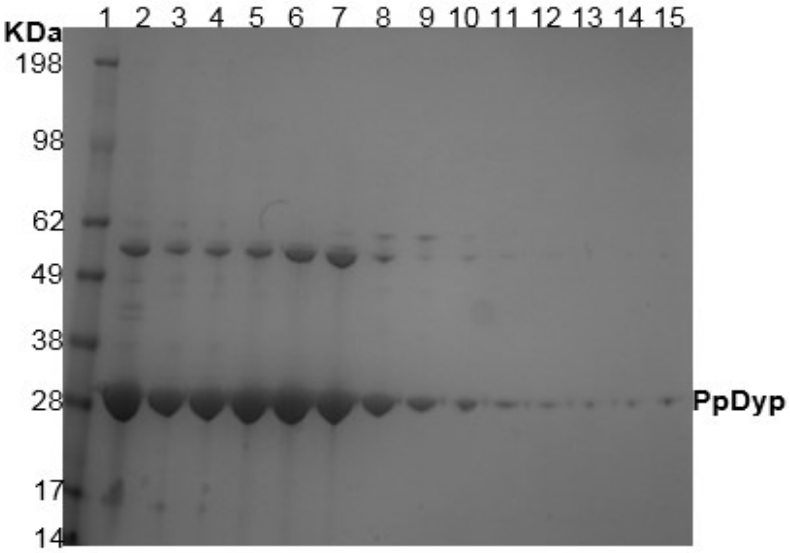

Figure 31. Size exclusion purification chromatogram of PpDyp.
The purification trace shown in (A) shows the absorbances at 280 nm and at 420nm. The fractions of PpDyp were collected and shown Lane 1 had SeeBlue™ Plus2 pre-stained protein standard, lane 2 the pooled, buffer-exchanged and concentrated sample of the Se-Met labelled PpDyp applied to the HiLoad Superdex 200 pg 16/60 column, lane 3 represented the flow-through from the size exclusion run, while lanes 4-15 were loaded with fractions that were eluted before, at the centre, and just after the rough peak around 70 ml on the elution volume axis. The PpDyp label on the right y-axis corresponds to the approximately 32 KDa size of the pure PpDyp. The second band on the gel is around 60KDa which would make it a dimer of PpDyp.

I pooled the Se-Met labelled PpDyp that emerged from the SEC column and used it to set up new crystallographic screens as in section 5.3.1 and from the results observed, going on to set up optimisation plates as in section 5.3.2**.** The best crystals obtained were from the PEG/Ion and Index HT™ (Hampton Research) screens (Figure 32). Most of the crystals were of the thin needle-like and fragile variety as in Figures 32 (B-E) apart from 32 (A) which had a corkscrew-like rectangular crystal. However, repeated optimisation failed to recreate this particular crystal shape and the only morphology seen was the needle-like crystals as in Figures 32 (F) and (G).

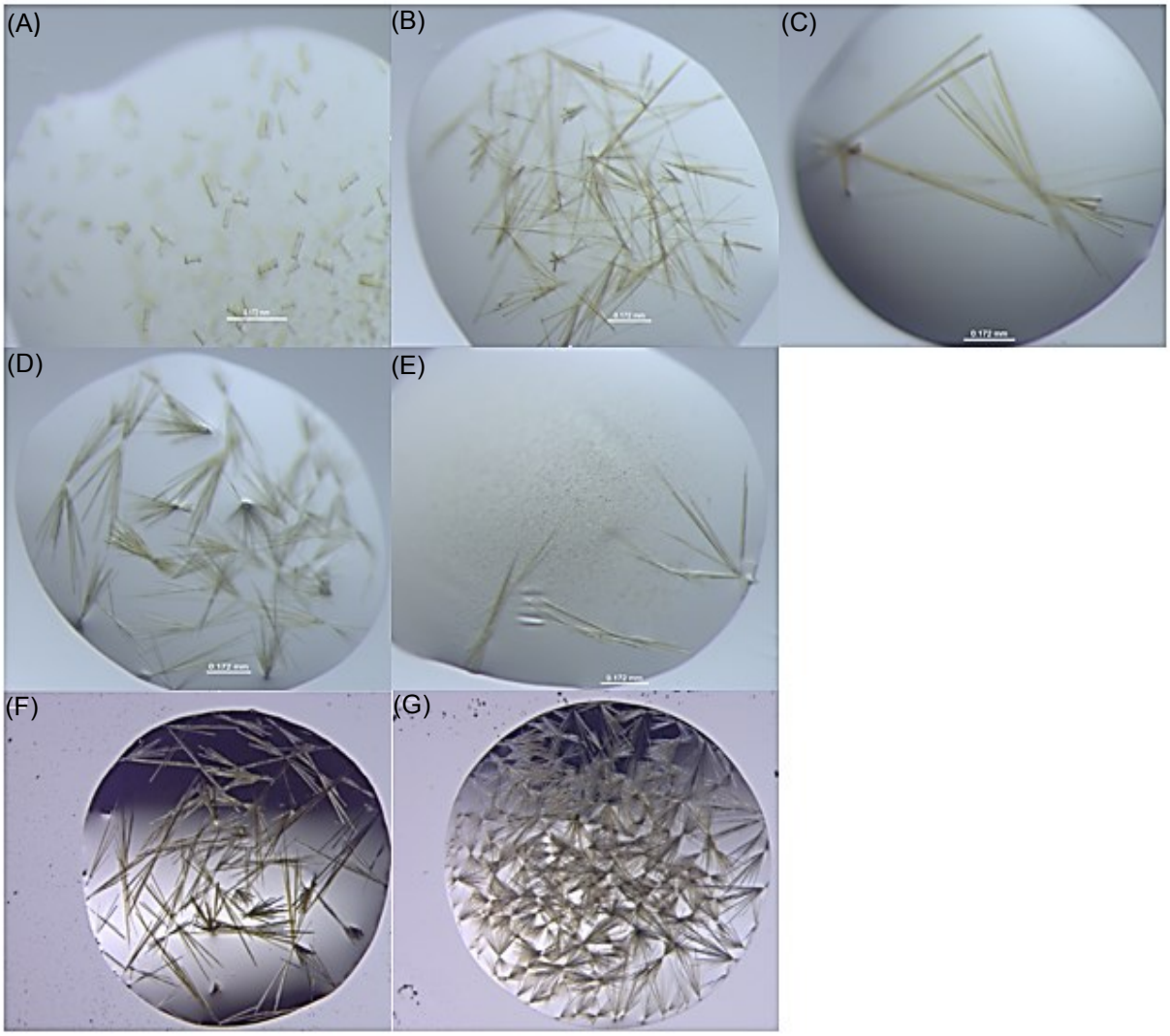

Figure 32. Crystals from screening and optimisation plates of selenomethionine labelled PpDyp.
All of the crystals show the same slight reddish-brown colour due to Fe^{3+} in the haem at the active site of the PpDyp. The first five crystal droplets (A-E) of the PpDyp observed and recorded with the Leica M205 C stereomicroscope are from the initial screening plates. The well conditions for each of the screens are: (A) PEG/Ion H2 – 0.05 M citric acid, 0.05 M Bis – Tris propane/ pH 5.0 and 16% w/v PEG 3,350; (B) and (C) PEG/Ion H3 – 0.04 M citric acid, 0.06 M Bis – Tris propane/ pH 6.4 and 20% w/v PEG 3,350 with the difference between both being the addition of 1 nanolitre (B) and 2 nanolitres (C) of PpDyp respectively; (D) PEG/Ion B8 – 0.2 M Magnesium formate dihydrate and 20% w/v PEG 3,350, pH 7.0; (E) Index G11 – 0.2 M Magnesium chloride hexahydrate, 0.1 M Bis – Tris pH 6.5 and 25% w/v PEG 3,350. The last two crystal drops (F and G) are from the only two drops that produce any crystals of all the conditions set up based on the screening conditions in (A) – (E). The composition of the drops are: (F) 0.1 M Magnesium formate dihydrate, 15% PEG 3,350 and 5% glycerol; (G) 0.1 M Magnesium formate dihydrate and 15% PEG 3,350. For the optimisation plates, the well solutions were made up to 1 ml with deionised water.

An inability to produce crystals yielding good quality diffraction using the selenomethionine labelling (Section 5.3.3) meant that I was not able to determine the three-dimensional structure of the PpDyp during the course of this project.

5.4 *Bacillus subtilis* dye-decolorizing peroxidase (BsDyp)

Bacillus subtilis Dyp (BsDyp) has a 42% sequence identity to the dye-decolorizing peroxidase (PDB ID: 5fw4) from *Thermobifida fusca* (Rahmanpour et al., 2016). The *Thermobifida fusca* Dyp, a Type-A Dyp like BsDyp, has the ability to oxidise Kraft lignin, lignin-model compounds (Rahmanpour et al., 2016) and would be a good model for determining the structure of BsDyp. Determination of the structure of BsDyp could provide an insight into why it is much more active than other types of Type A peroxidases (Santos et al., 2014); whether this extends to its ability to degrade Kraft lignin and other types of technical lignins; the amino acid residues essential in its activity and present in its active site besides aspartate and asparagine; and its general ability to oxidise such a wide range of substrates (Mendes et al., 2015). This would make it possible to engineer this peroxidase to carry out lignin degradation more efficiently. This would also mean that focus could be placed on BsDyp as an industrial workhorse for the production of a vast array of useful industrial final products or platform chemicals that can be fed into other industrial pathways.

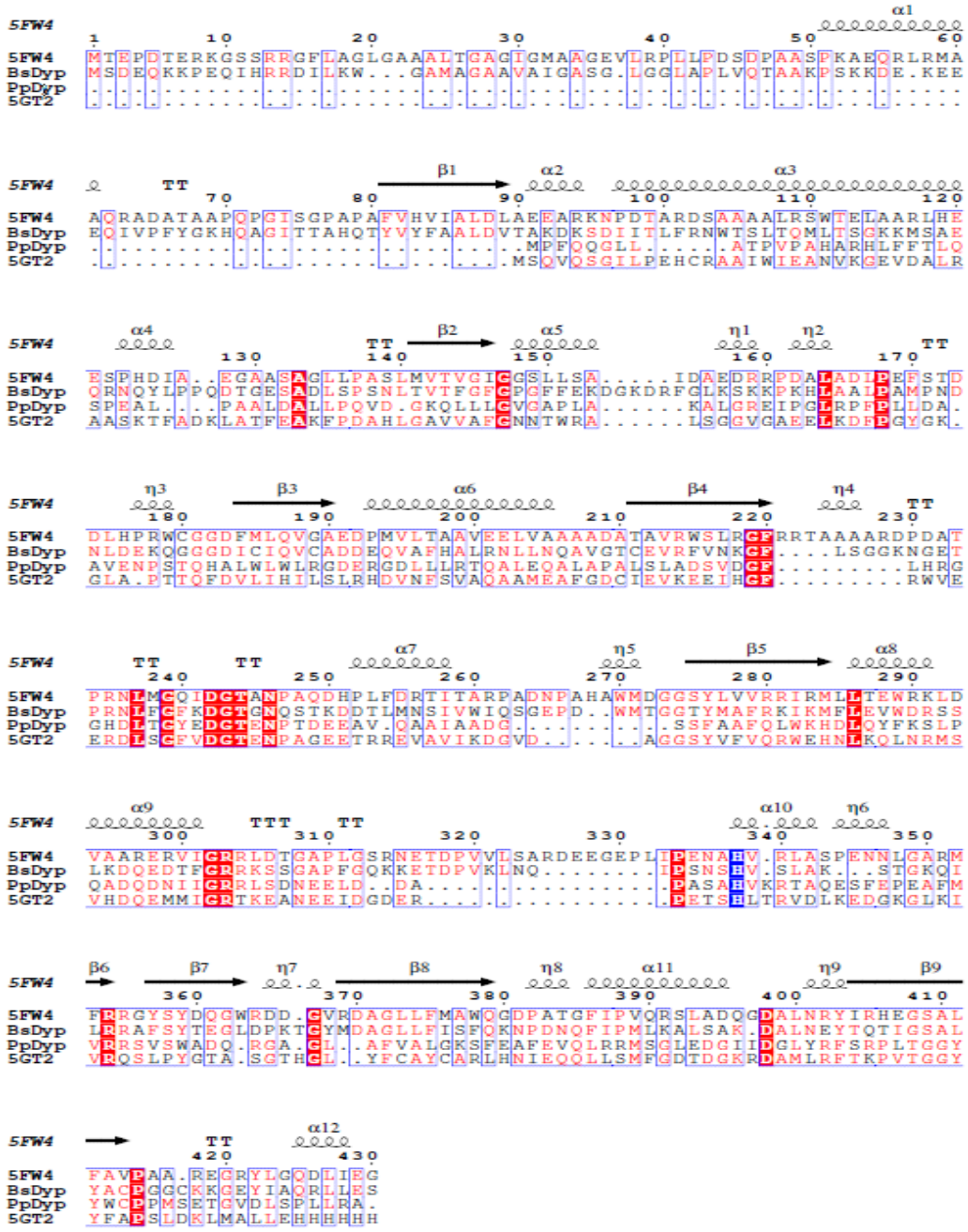

Figure 33. Multiple sequence alignment of BsDyp with PpDyp and their two closest homologues.

Bacillus subtilis dye-decolourising peroxidase was aligned with the dye-decolourising type peroxidase from *Thermobifida fusca* (PDB ID: 5FW4), the *Escherichia coli* O157 dye-decolourising peroxidase, YfeX (PDB ID: 5GT2) and the *Pseudomonas putida* MET94 dye-decolourising peroxidase. The alignment was done using Multalin and Clustal Omega (Corpet, 1988, Li et al., 2015) and the output displayed as an ESPript 3.0 file (Robert and Gouet, 2014). The distal haem coordinating residue, Histidine-326 in BsDyp and conserved in all the residues is highlighted in the blue box. Sequence identity to BsDyp is 42% for 5FW4, 19.87% for 5GT2 and 21.86% for PpDyP. The output file shows consensus sequences in red boxes and shows the twelve α-helices, nine β-strands, nine 3_{10}-helices(η), seven strict β-turns(TT) and one strict α-turn(TTT). The twin arginine motif (RR-motif) at residues 13 and 14 for both proteins indicate that the BsDyp was originally translocated fully folded with haem at its active site through the Twin arginine translocation (TAT) pathway. The predicted cut site is between residues 44 and 45 of the BsDyp sequence according to the TatP 1.0 server (Bendtsen et al., 2005). The conserved GxxDG sequence around Aspartic acid 240 common to all dye-decolourising peroxidases is present in all four peroxidases (Sugano, 2009)

5.4.1 Crystallisation and structural determination of *Bacillus subtilis* dye-decolourising peroxidase (BsDyp)

5.4.1.1 Screening of crystallisation conditions of BsDyp

The purified BsDyp obtained from Professor Ligia Martins' laboratory was at a concentration of 11.6 mg/ml. This was used to set up crystallisation trials via the sitting-drop vapour diffusion method on the Gryphon nanolitre pipetting robot (Art Robbins). Two of the screens, JCSG-plus™ HT-96 and PEG/Ion HT™, were the most conducive for the formation of BsDyp crystals. The crystals from the initial screening are shown in Figure 34**.**

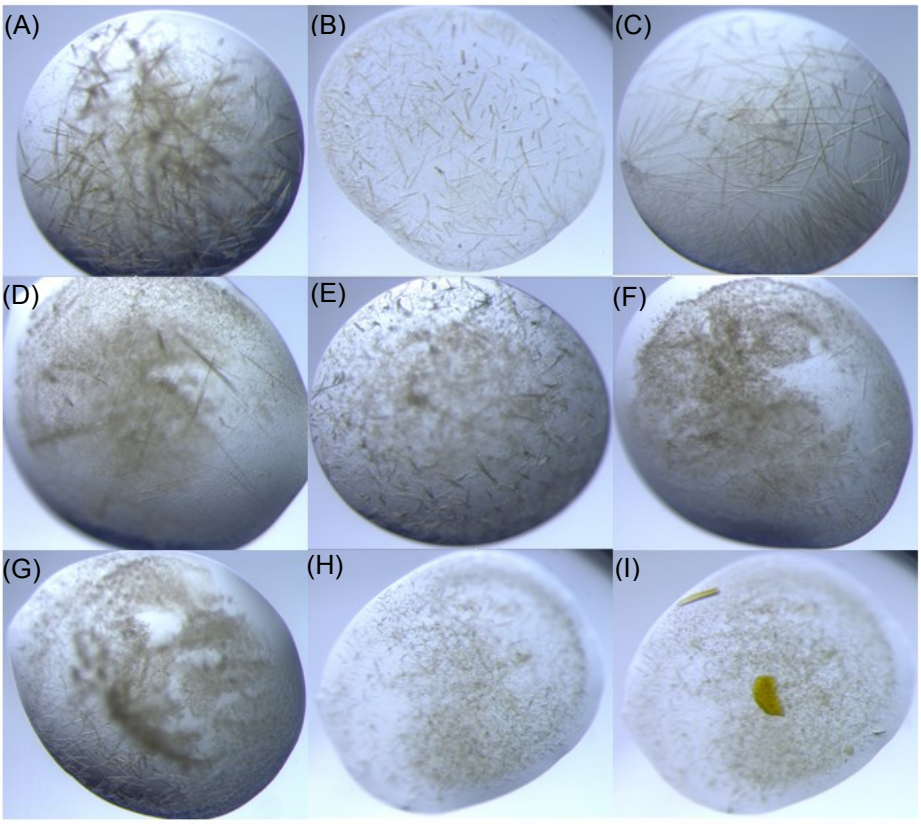

Figure 34. Crystals obtained from the initial screening of BsDyp.
The crystals observed are mostly needle-like shapes as in PpDyp, except for plate **(I)** which has a flat plate-like appearance and a thicker needle shape at its edge. The reddish-brown colour due to the haem iron at the active site of the BsDyp is present as in PpDyp but there is a reduced colour intensity for the BsDyp crystals in the screening plates. The well conditions for each of the screens are: (A) JCSG D6 – 0.2 M magnesium chloride, 0.1 M Tris and 20% w/v PEG 8,000, pH 8.5; (B) JCSG D5 – 0.1 M HEPES and 70% v/v 2, 4-methyl pentanediol (MPD), pH 7.5 (C) JCSG G5 – 0.005 M magnesium chloride, 0.1 M HEPES, 12% w/v PEG 3,350, pH 7.5; (D) PEG/Ion B8 – 0.2 M Magnesium formate dihydrate and 20% w/v PEG 3,350, pH 7.0; (E) PEG/Ion D12 – 0.2 M Ammonium citrate dibasic, 20% w/v PEG 3,350, pH 5.1; (F) PEG/Ion E10 – 8% v/v Tacsimate pH 4.0 and 20% w/v PEG 3,350; (G) JCSG E11 – 0.16 M calcium acetate, 0.08 M sodium cacodylate, 14.4% w/v PEG 8,000/20% v/v glycerol, pH 6.5; (H) JCSG C3 – 0.2 M ammonium nitrate, 20% w/v PEG 3,350; and (I) JCSG C2 – 1.0 M lithium chloride, 0.1 M sodium citrate, 20% w/v PEG 6,000, pH 4.0.

5.4.2 Optimisation of crystallisation conditions of BsDyp

I optimised the conditions observed during the initial screening of BsDyp using the hanging-drop vapour method manually on 24-well Linbro tissue culture plates with an increase in well solutions (1 ml) and droplet volume (1 µl) to promote the formation of better diffracting crystals. The initial screen showed that a combination of magnesium, calcium, ammonium and lithium salts, together with polymers such as glycerol, PEG 3,350, 6,000 and 8,000 over a pH range of 4.0 – 8.5, resulted in the formation of BsDyp crystals and the optimisation was done by varying these initially discovered conditions. The drops with successful crystal growth are shown in Figure 35**.**

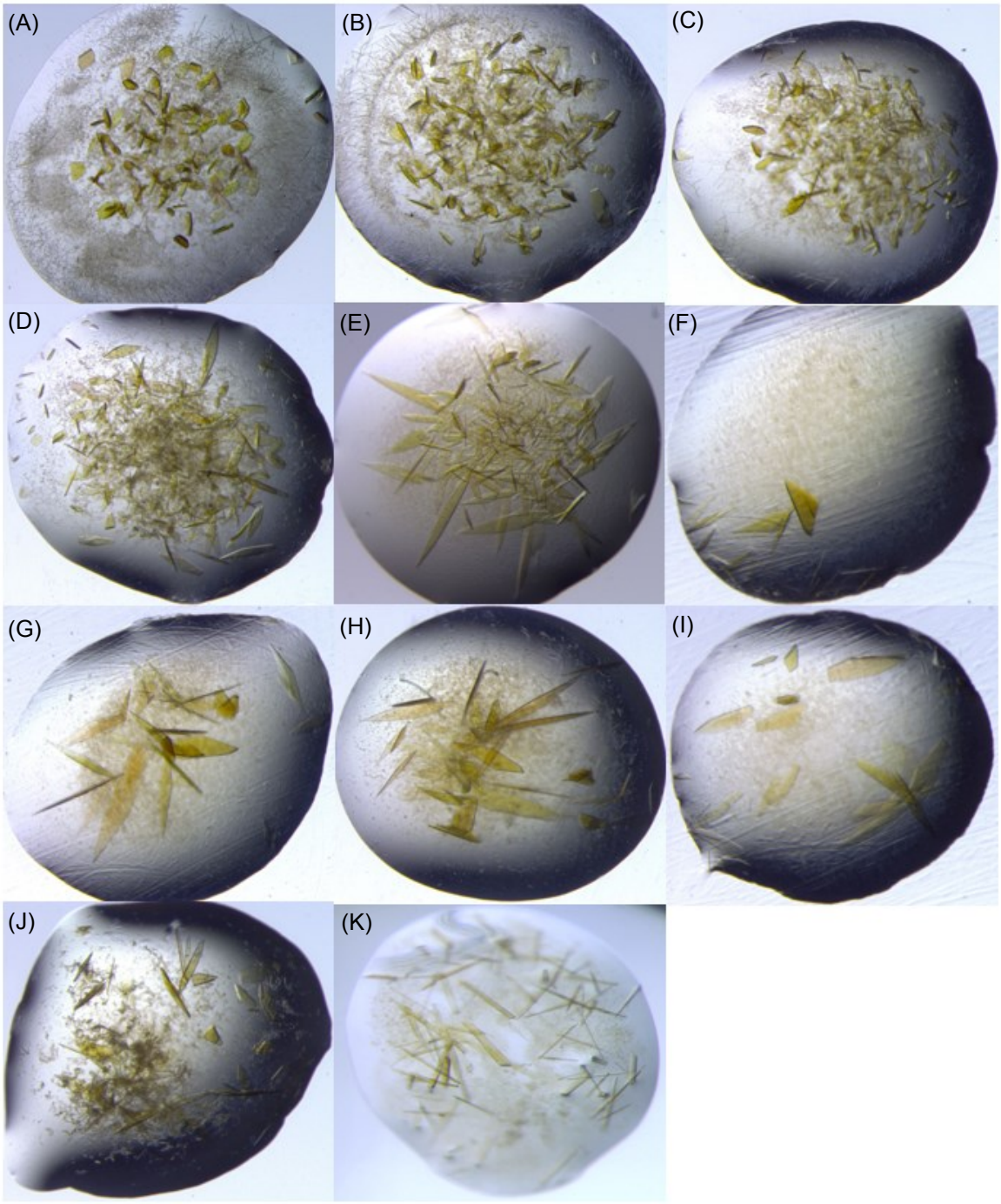

Figure 35. Crystals from the optimisation of BsDyp.
These are crystals obtained from the optimisations of BsDyp based on the results of the initial screening shown in Figure 34. The crystals all have the reddish-brown colour due to the haem iron and are mostly the flat plate-like shape of varying sizes, plate (K) being the exception with needle-like crystals together with some rectangular crystals within its hanging drop. All the crystals were fragile and had a tendency to break up into smaller pieces when they were being transferred for data collection. All of the drops from (A) to (J) are at pH 4.0 and have 0.1 M sodium citrate in them. The rest of the drops i.e. (A) to (J) are made up of: (A) 0.8 M Lithium chloride and 15% PEG 6,000; (B) 0.9 M Lithium chloride and 15% PEG 6,000; (C) 1.0 M Lithium chloride and 15% PEG 6,000; (D) 1.05 M Lithium chloride and 15% PEG 6,000; (E) 1.0 M Lithium chloride and 10% PEG 6,000 (F) 1.05 M Lithium chloride and 10% PEG 6,000; (G) and (H) 1.1 M Lithium chloride and 10% PEG 6,000; (I) and (J) 1.2 M Lithium chloride PEG 6,000. Drop (K) is made up of 0.2 M ammonium nitrate and 20% w/v PEG 3,350

5.4.3 Structural determination of BsDyp

The crystals obtained in section **5.4.2** were harvested from the drops, quickly transferred to a cryoprotectant solution (well solutions in which the crystals were harvested plus 20% PEG 200) and flash-cooled in liquid nitrogen. The crystals were transferred using uni-pucs to the Diamond Light Source (Didcot, UK). I collected multiple datasets on the beamline, I04-1 and from these datasets the best statistics obtained were used in determining the structure of BsDyp. Molecular replacement, a technique which involves the use of a known search molecule to solve for an unknown structure (Rossmann, 2001), was used for the structural determination of BsDyp in space group $P\ 1\ 2_1\ 1$ to 2.75 Å . The search model used was the *Thermobifida fusca* dye-decolourising peroxidase (PDB ID: 5fw4). All structure figures were generated using PyMol 1.8 (Schrodinger, 2015). Table 5.4.3 shows all of the data pertaining to X-ray data collection and refinement statistics. Figures 36 shows the structure of BsDyp at 2.75 Å in its monomeric form, dimeric form, the haem at its active site and the residues surrounding it and alignments of BsDyp with its closest homologue, the dye-decolourising peroxidase from *Thermobifida fusca*.

Table 5.4.3. Data collection and refinement statistics

BsDyp	
Beamline	I04-1
Wavelength(Å)	2.75
Resolution range (Å)	48.68 – 2.751 (2.849 – 2.751)
Space group	P 1 2_1 1
Unit cell (Å) ***a***	157.109
b	73.093
c	220.094
β (º)	109.938
Total reflections	676,064 (60,699)
Unique reflections	111,233 (10,439)
Multiplicity	6.1 (5.8)
Completeness (%)	90.41 (85.87)
Mean I/sigma (I)	5.75 (1.35)
Wilson B–factor	34.18
R-merge	0.3263 (1.281)
R-meas	0.3569 (1.404)
R-pim	0.1414 (0.5609)
$CC_{1/2}$	0.974 (0.746)
CC*	0.993 (0.924)
Reflections used for R-free	5,417 (481)
R-work	0.3125 (0.3075)
R-free	0.4365 (0.4477)
CC(work)	0.860 (0.826)
CC(free)	0.637 (0.457)
Number of non-hydrogen atoms:	32,847
macromolecules	32,389
solvent	458
Protein residues	4,164
RMS (bonds)	0.021
RMS (angles)	2.03
Ramachandran favoured (%)	73.82
Ramachandran allowed (%)	17.02
Ramachandran outliers (%)	9.16
Rotamer outliers (%)	12.00
Clashscore	57.97
Average B-factor:	25.08
macromolecules	25.17
solvent	18.99

Statistics for the highest-resolution shell are shown in parentheses.

(A)

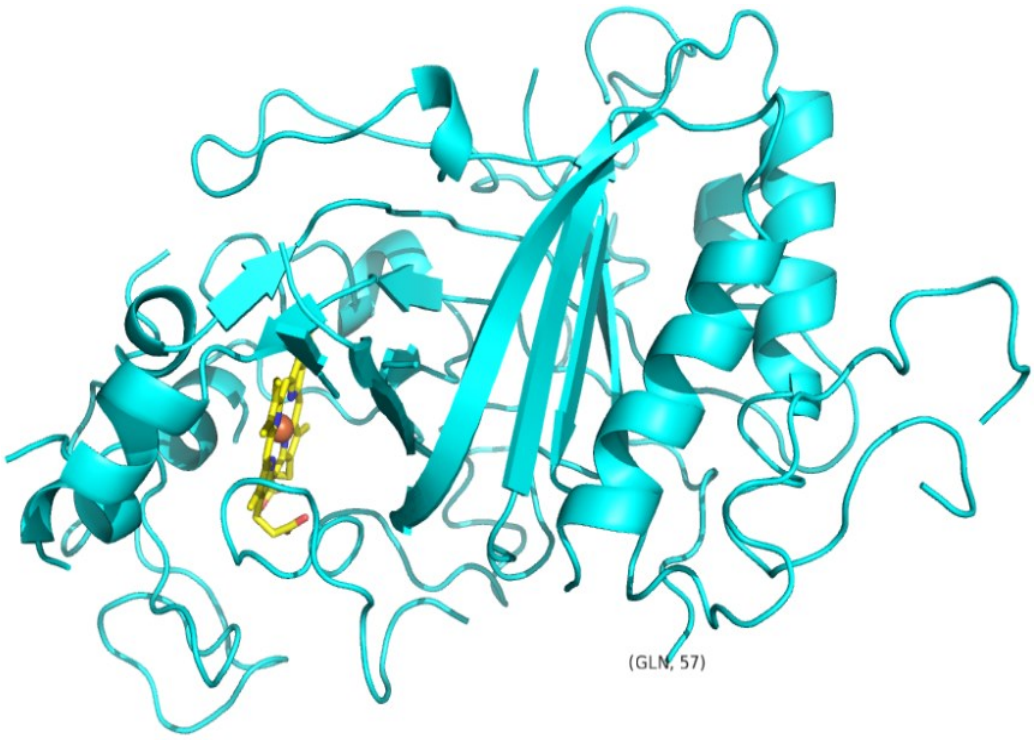

(B)

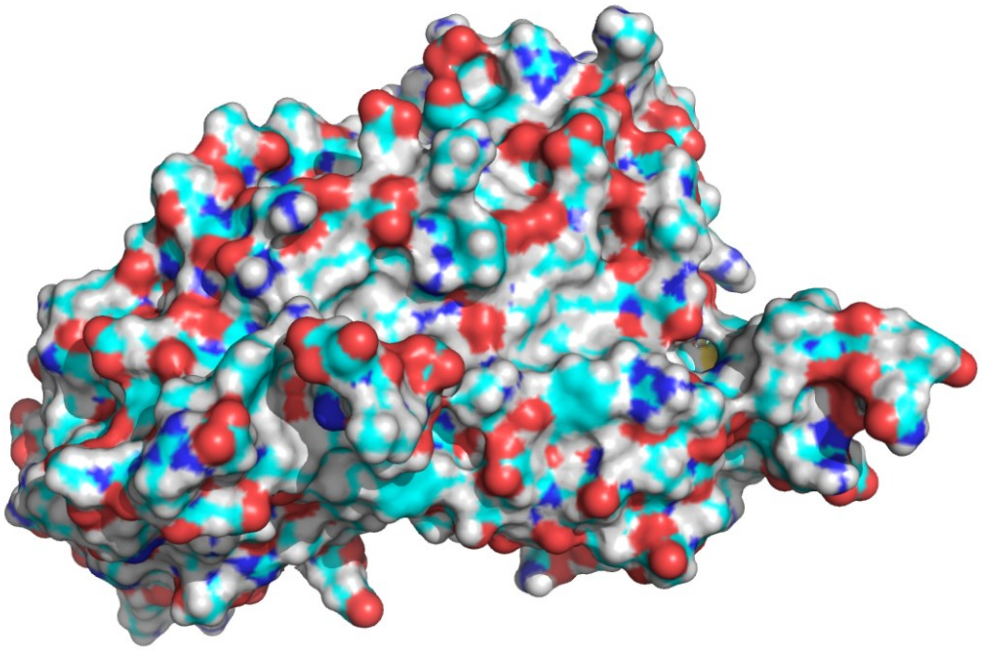

Figure 36. Structure of BsDyp monomer.
The X-ray crystallographic structure of BsDyp generated by PyMol 1.8 (Schrodinger, 2015). The top figure is a cartoon representation and shows α-helices, β-sheets, β-turns and the loops that make up the structure of BsDyp. The Glutamine-57 residue at the N-terminus of the BsDyp model is also labelled. The model shows the iron protoporphyrin IX (haem *b*) typically found in the active site of most peroxidases (Fujii, 2016). The iron atom at the centre of the haem is denoted by a brown sphere, the four nitrogen atoms attached directly to the central iron were represented by a deep blue colour and yellow denoted the colour of the rest of the protoporphyrin IX structure. The bottom picture is a representation of the surface of the BsDyp monomer.

(A)

(B)

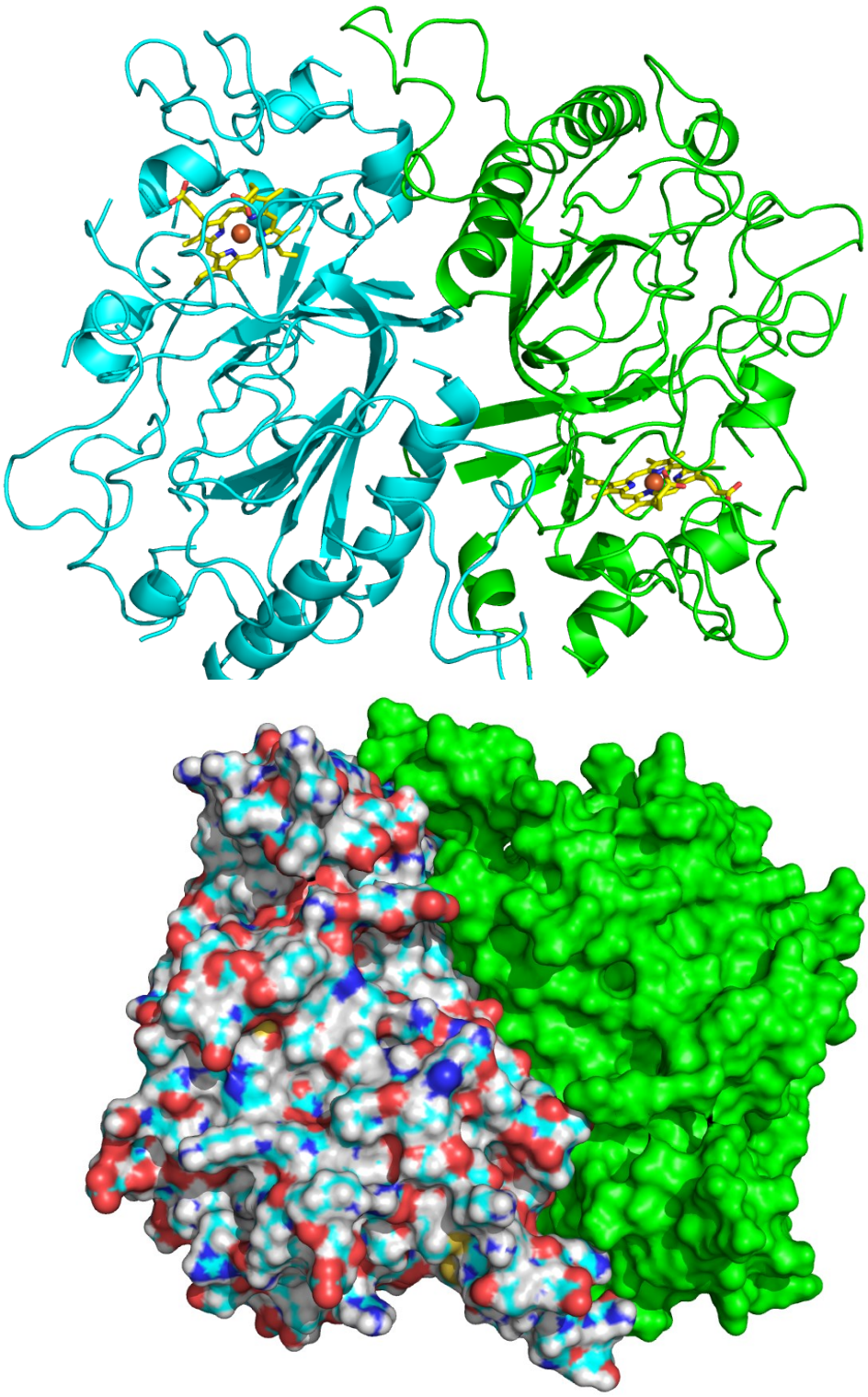

Figure 37. Structure of BsDyp dimer.
This is the crystallographic structure of the dimer of BsDyp generated by PyMol 1.8 (Schrodinger, 2015). The top figure is a cartoon representation of both monomers making up the dimer and shows the various secondary structures as well as the two haem irons at the active site of the monomers. Monomer 1 on the left is represented as light blue while Monomer 2 on the right is depicted as light green. The iron at the centre of the haem group could be Fe^{2+} or Fe^{3+} depending on the length of the exposure of the BsDyp to X-rays during data collection at the synchrotron facility (Rahmanpour et al., 2016). The bottom picture is a surface description of the BsDyp dimer also shown in two major different colour schemes to represent each monomer.

A.

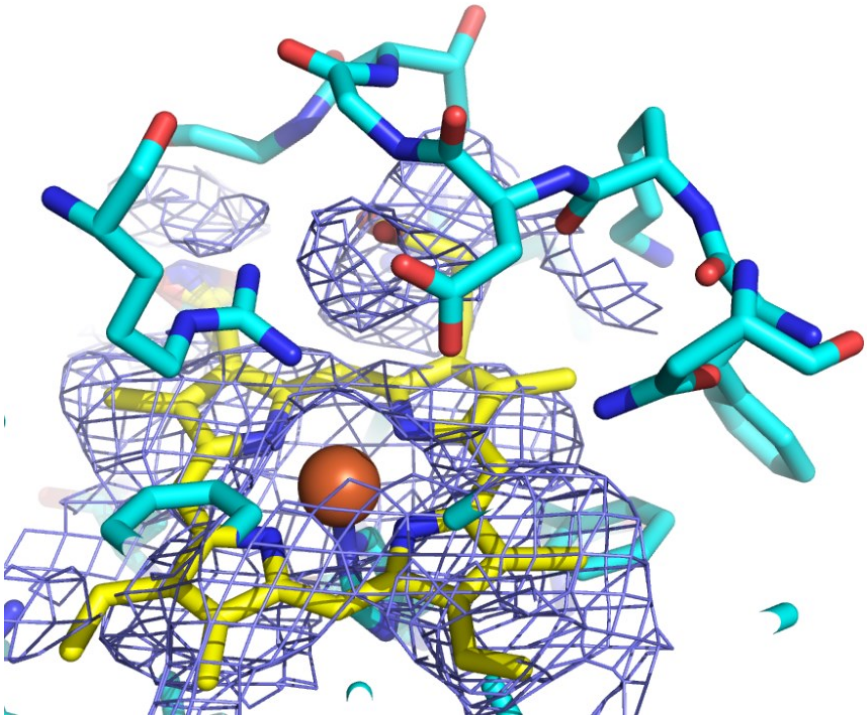

B.

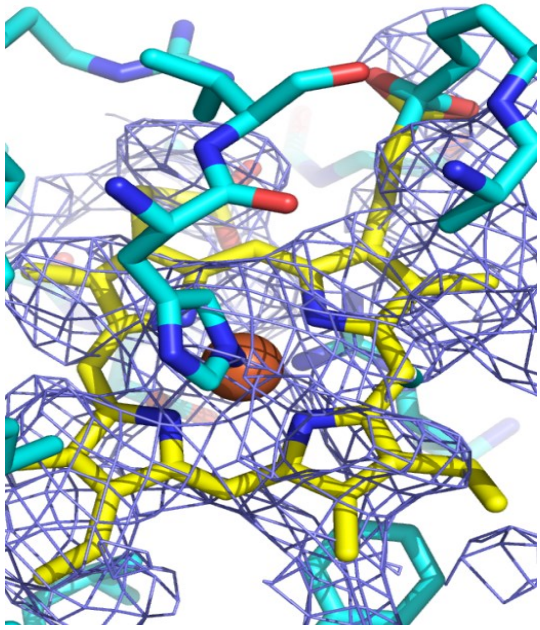

Figure 38. Distal and proximal views of active site haem and surrounding residues in BsDyp. The two images represent the Distal **(A)** and Proximal **(B)** view of the haem, together with its corresponding electron density at the active site of BsDyp. The colour scheme for the amino acid residues is as follows: Red – oxygen atoms; Deep blue – nitrogen atoms and Light blue – carbon atoms. Hydrogen atoms are not represented. The iron represented by the brown sphere is seen to be tetrahedrally coordinated by the four nitrogen atoms of the porphyrin ring. The three amino acid residues, Arginine 339, Aspartic acid 240 and Asparagine 234 in **(A)** and the Histidine 326 in **(B)** all play a role in anchoring the haem group in place in BsDyp. All of the active site residues also play a role in transporting electrons both to and from the haem during BsDyp's reaction with different substrates (Sugano, 2009). This model also confirms the absence of a distal Histidine residue, a feature common among all dye-decolourising peroxidases.

A.

B.

C.

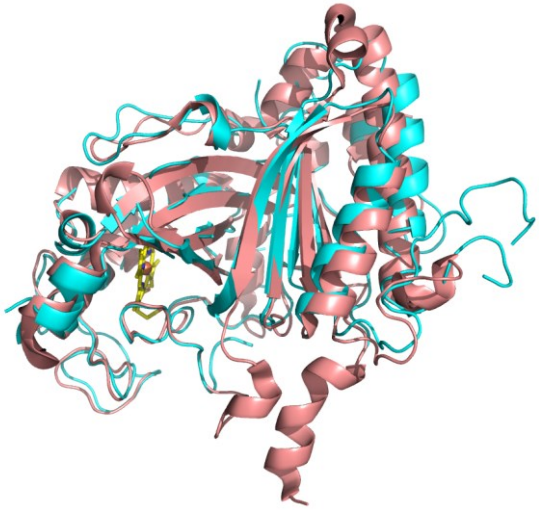

Figure 39. Multiple structural alignment of BsDyp with other dye-decolourising peroxidases. The solved BsDyp structure was aligned with three previously deposited structures in the Protein database (PDB). The three proteins share higher than 30% primary sequence identity with BsDyp. BsDyp is represented by a light blue colour while the protein being compared against are represented by the other colours. The three proteins, PDB identities, their percentage sequence identities, and the resolution of their crystal structures are: - (A) Dyp-type peroxidase (SCO2276) from *Streptomyces coelicolor*, 4GRC, 45%, 2.0 Å; (B) EfeB from *Escherichia coli* O157 in complex with heme, 3O72, 38%, 1.95 Å; (C) Dyp-type peroxidase from *Thermobifida fusca*, 5FW4, 34%, 1.8 Å. (Lukk et al., 2013, Liu et al., 2011, Rahmanpour et al., 2016).

The BsDyp crystallographic structure shows a combination of α-helices and β-sheets. The β-sheets are anti-parallel in nature and a combination of these with the α-helices leads to the formation of a ferredoxin-like fold in the enzyme. Ferredoxin-like folds are commonly found in dye-decolourising peroxidase family of proteins (Liu et al., 2017). The BsDyp structure seems to be divided into two major domains; (a) a ferredoxin-like fold domain and (b) a haem-binding domain. There is varying degrees of conservation of the secondary and non-secondary structure elements of the BsDyp structure when it is aligned with the three different proteins with the greatest variation being in the *Thermobifida fusca* protein which has the least similarity to BsDyp and the greatest match in structural alignment being with the *Streptomyces coelicolor* dyp-type peroxidase which also shares the closest similarity in primary sequence identity.

Despite the solved structure above giving us some information about the protein, it could not be deposited in the PDB as the anisotropic nature of the diffraction and limited resolution of the data meant that there was a degree of ambiguity in the resulting electron density obtained from phasing. Repeated modelling and refinement of the structure could not solve this problem, due to the nature of the crystals obtained (flat plates/needle-shaped) during the crystal production phase.

5.4.4 Protein engineering of BsDyp

A common approach to improving the quality of crystals is protein engineering (Rupp, 2010, Bonnefond et al., 2011). It had been observed during the determination of the crystal structure of BsDyp that the first electron density visible at the N-terminus is that of the Glutamine-57. Before this residue is a sequence of 8 positively charged amino acids (KKDEKEEE) that may have a destabilising effect on the formation of any secondary structures. I designed a truncated construct of BsDyp (BsDyp-trunc) that started at residue Asp-56 of the initial BsDyp construct was sub-cloned into pET 28a(+), sequenced and expressed in BL21(DE3) (Invitrogen) competent cells. Figure 40 shows the agarose gel images of the vector in the sub-cloning of the BsDyp-trunc.

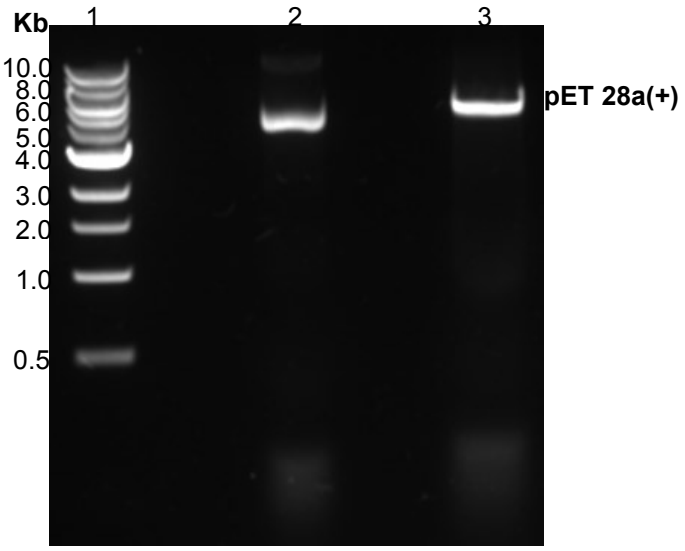

Figure 40. DNA agarose gel of the vector used for sub-cloning the truncated BsDyp (BsDyp-trunc)
Gel (A) is made up of: lane 1 – 1 Kb DNA ladder (NEB); lane 2 – uncut pET 28a(+); lane 3 - double digest of the pET 28a(+) by the type II restriction enzymes Nco1 and Xho1. The size of the pET 28a (+) is 5369 base pairs (bp). A PCR product of BsDyp-trunc with overhang at the 5' end containing the Nco1 restriction site, C$^{\vee}$CATGG and the 3' end containing the Xho1 restriction site C$^{\vee}$TCGAG was generated. The PCR product was ligated to the double-digested vector, transformed into Top 10 competent cells (Invitrogen), the transformants were sequenced and the correct sequences were then re-transformed into BL21 (DE3) (NEB) competent cells.

The BsDyp-trunc is made up of 363 amino acids and has a molecular weight of 40.1 KDa and an isoelectric point (pI) of 8.44. BsDyp-trunc was purified via a two-step purification strategy which involved an immobilized metal affinity chromatography (IMAC) step followed by a size exclusion chromatography (SEC) step. The IMAC step was done by passing the crude cell extract through a 1 ml HisTALON column (Takara Bio) which has a cobalt resin. Figure 41 shows the purification trace (a) and the SDS-PAGE gel (b) of this process.

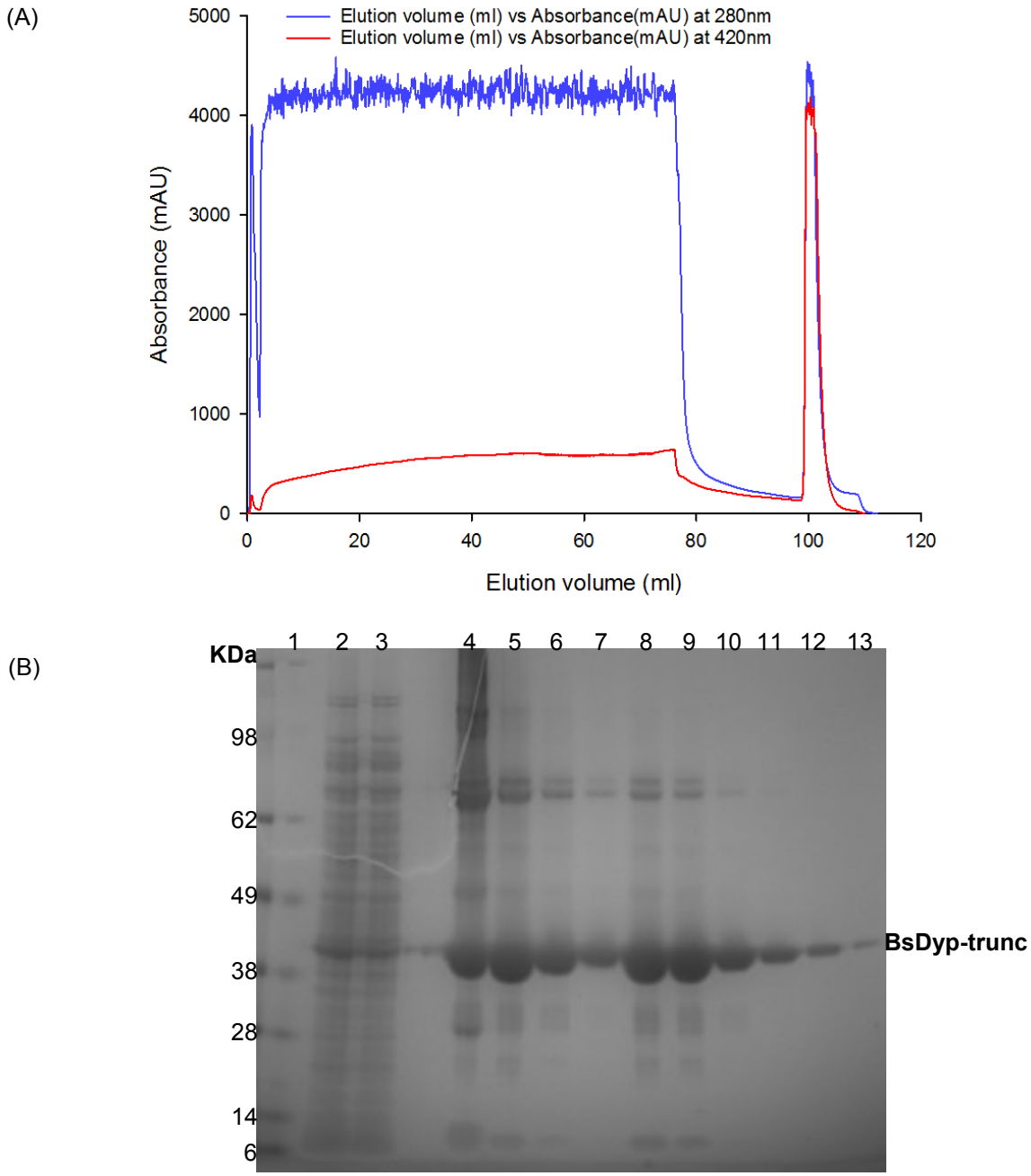

Figure 41. IMAC purification chromatogram of BsDyp-trunc.
The purification trace shown in (A) shows the absorbance at 280nm which monitors the presence of protein and the absorbance at 420 nm which monitors the presence of the haem iron of BsDyp-trunc. The fractions were collected over 20 column volumes. SDS-PAGE was carried out to visualise the collected fractions. Lane 1 had SeeBlue™ Plus2 pre-stained protein standard, lane 2 was loaded with the original extract of the cell extract of the BsDyp-trunc while lane 3 was loaded with the flow-through from the purification run that had never bound to the column and had come off during the washing step, while lanes 4-13 were loaded with fractions that were eluted from the rough peak around 100 ml on the elution volume axis. The BsDyp-trunc label on the right y-axis corresponds to the approximately 40 KDa size of the protein being purified.

The BsDyp-trunc fractions, as determined from both the purification chromatogram and the SDS-PAGE gel were pooled and concentrated to a final volume of 2.0 ml before being

applied to a HiLoad Superdex 200 pg 16/60 column (GE) for a size exclusion chromatography step shown in Figure 42.

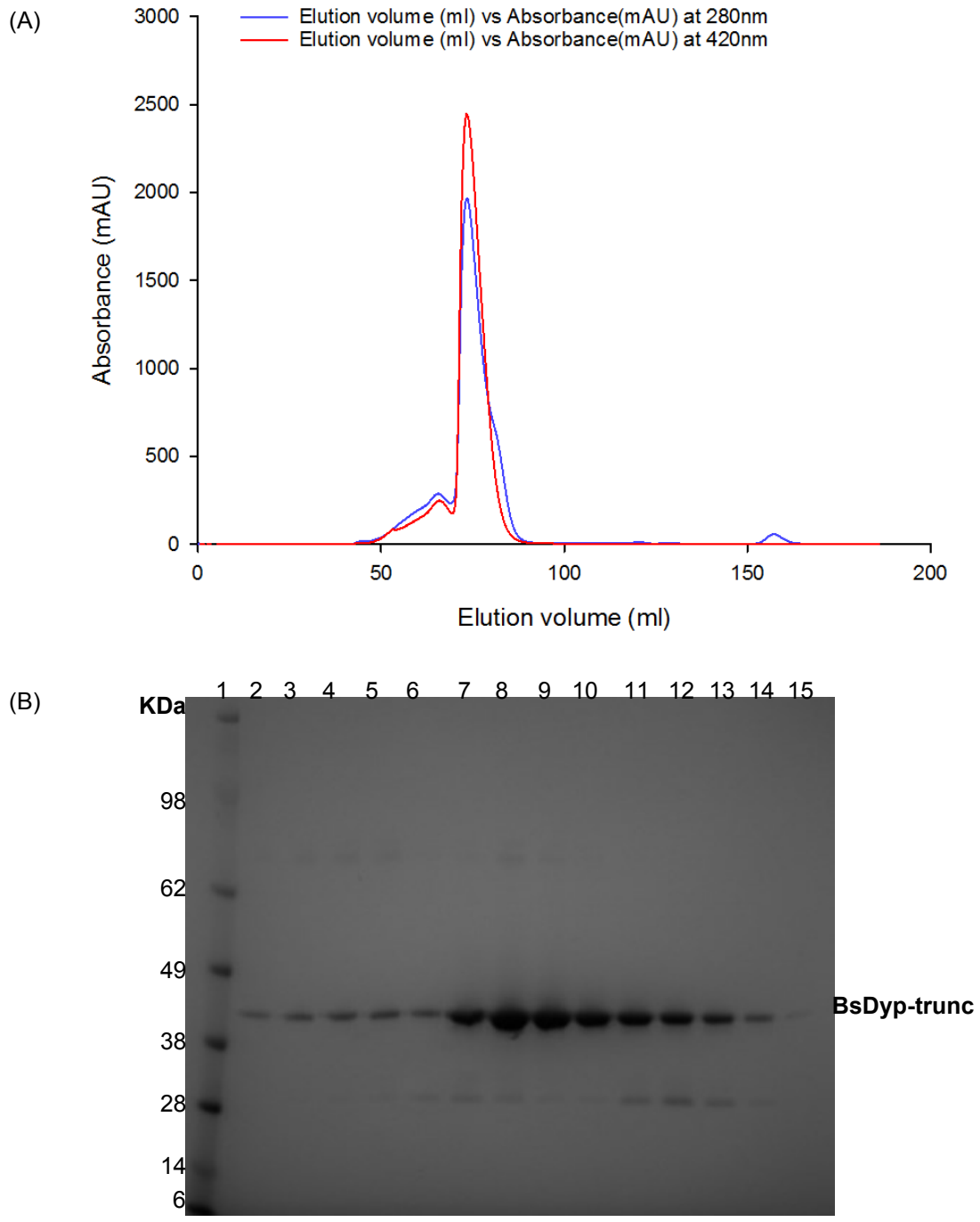

Figure 42. Size exclusion purification chromatogram of BsDyp-trunc.
The purification trace shown in (A) shows the absorbances at 280 nm and at 420 nm signifying the presence of protein and haem iron respectively. The SDS-PAGE gel shows: Lane 1 - SeeBlue™ Plus2 pre-stained protein standard; lane 2 – pooled and concentrated sample of the BsDyp-trunc applied to the HiLoad Superdex 200pg 16/60 column; lanes 3-15 - fractions that were eluted before, at the centre, and just after the rough peak around 70 ml on the elution volume axis. The BsDyp-trunc label on the right y-axis corresponds to the approximately 40 KDa size of the BsDyp-trunc. The second band on the gel and the little peak just before the big peak could correspond to the presence of a BsDyp-trunc dimer.

The purified BsDyp-trunc was used in setting up crystallization screens and only produced an amorphous shaped crystal and clusters of needle shaped crystals (Figure 43) which failed to produce better crystals despite several optimisation attempts.

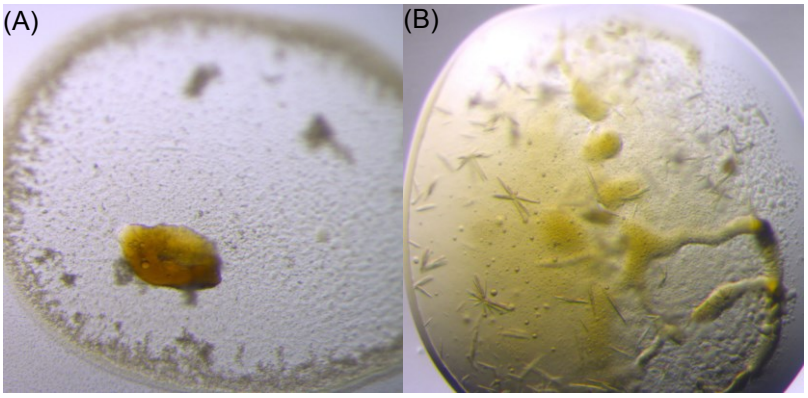

Figure 43. Crystals from the screening plates of truncated BsDyp.
Both crystal plates show the same reddish-brown colour due to the haem iron at the active site of the BsDyp-trunc with (A) being a deeper shade than (B). The well condition for each screening plates: (A) JCSG B5 – 0.1 M sodium cacodylate pH 6.5, 40% v/v 2,4-methyl pentanediol/ 5% w/v PEG 8,000; (B) JCSG C2 – 1.0 M lithium chloride, 0.1 M sodium citrate/ pH 4.0 and 20% w/v PEG 6,000.

5.5 Summary and discussion

Both recombinant *Pseudomonas putida* MET94 and *Bacillus subtilis* dye-decolorizing peroxidases, PpDyp and BsDyp respectively were crystallised. The grade of the crystals produced for both proteins were not high quality. For PpDyp, the diffraction pattern gave quite a high level of anisotropy and an attempt at selenomethionine labelling was undertaken to correct this which did not lead to an improvement in crystal quality and diffraction data as expected. For BsDyp, a low resolution crystallographic structure was generated which was able to give us some information on its possible oligomeric state of the protein, its haem microenvironment as well as likely residues involved in its haem coordination. The residues observed were similar to that of other dye-decolourising peroxidases. The low resolution of the structure meant that the information on its dimeric nature and the exact position of all the individual atoms could not be verified by the PDBePISA server. Protein engineering to truncate its disordered N-terminal region did not achieve the positive effect on crystal quality that was hoped for.

Further work to improve the quality of the crystals needs to be done, as this is the first step towards getting better structural data. A rational design of portions of both enzymes could prove the best means of achieving this as it has been shown that the active site of this class of enzymes is very good at adjusting to mutations, with the haem capable of switching its hydrogen bonding and ligand coordination partners if necessary. This could mean the production of more stable and better diffracting crystals. The information obtained when combined with information available on their electrochemistry should shed light on their redox potential and ways of manipulating this, their haem coordination ability and whether its active site residues have a role to play in its oligomeric state. The ability of the enzymes to break down different classes of substrates, depending on what mutations have taken place in

them could also be taken advantage of in the industry to turn them into true specialist enzymes as well. The current promiscuity of the enzymes could make them less financially feasible in industrial processes (Zubieta et al., 2007, Sezer et al., 2013, Chen et al., 2015, Li et al., 2017, Liu et al., 2017).

Chapter 6: Discussion and Conclusion

The main aim of this doctorate study was to utilise one of the major components of lignocellulosic biomass, lignin, to characterise several lignin degrading enzymes of fungal and bacterial origin and to identify some lignin degradation products to see if we could get any useful materials from them. From my results in Chapter 3, I showed that the *Pichia Pastoris* expression system could be used for expressing the laccase from *Panus rudis*. The laccase was active on several model substrates and this was demonstrated both in liquid and solid media. The optimum temperature and pH at which the laccase is most active was shown in the chapter and this was utilised in designing the lignin degradation experiments.

Lignin degradation has been recognised as a very difficult but necessary process by the chemical industry for a long period of time. It was needed because to get to the cellulose present in lignocellulosic biomass, the lignin had to be removed. Several chemical methods have been developed to do this but for this study, a method that would require the use of little or no chemicals was decided on. Enzymatic degradation using the laccase was utilised to break it down because it has the reputation of being a green enzyme. The degradation of the lignin could also add value to the lignocellulose breakdown process if any new, useful products were discovered. Various techniques were used to examine the industrial waste product, Kraft lignin, as a substrate for enzymatic degradation and to see if any of the degradation products could find industrial use or be a compound that could be useful for making other industrially useful compounds.

Scanning electron microscopy was a very simple technique to identify the morphological changes to the lignin while the degradation was taking place but the major information it revealed was that the freeze-drying process, which was a required part of the sample preparation process, had a greater impact on the morphology of the Kraft lignin than the

actions of the laccase on the Kraft lignin. It also showed that not all enzymes create easily visible physically recognisable changes on the lignin polymer when they carry out the degradation process. This highlighted the need for a more molecular examination of the lignin degradation process.

FTIR spectroscopy is a highly used technique in identifying various components of intact biomass, and any changes taking places in degraded biomass. It is able to differentiate between various types of technical lignins and for my purposes, identifying functional groups being modified during the degradation of lignin. Combining FTIR with the multivariate statistical analysis, PCA, I was able to not only identify the bonds being modified during the degradation process, which were alkyl C-O ether bonds being stretched, stretching of the C-S bonds which indicates that the laccase has a role to play in ether bond cleavage or at least in making the bond susceptible to cleavage by other enzymes. I was also able to show the importance of the mediator, acetosyringone in the degradation of the Kraft lignin by *Panus rudis* laccase.

The next step was an identification of some of the compounds that were present in the degradation mixture and this was done using FTICR-MS. To date, no FTICR-MS studies of enzymatic degradation of lignin has been published. This technique enabled me to show the various classes of compounds that were present at the beginning and at the end of a seven-day reaction. Van Krevelen and double bond equivalent plots for both time points give a picture of the changes that are taking place in the various aromatic groups present within the mixture. All the plots also helped to clearly show that the depolymerisation of the Kraft lignin was taking place as there was a reduction in the overall amounts of high mass compounds and an increase in the amounts of low mass compounds among the lignin degradation compounds This technique allows the tracking of the changes the compounds have undergone during the

degradation and identify resulting compounds that could be useful as platform chemicals. It falls short of fully identifying all of the chemical species present in the mixture but a combination with techniques such as gas chromatography and liquid chromatography mass spectrometry could help to solve this problem.

The crystallisation of two dye-decolorizing peroxidases (BsDyp and PpDyp), another class of lignin degrading enzymes was done as part of this thesis project but only one, BsDyp produced any diffraction data that could be modelled into structural data. This enzyme is dimeric, and I identified the residues involved in the coordination of haem, but further information could not be obtained due to the quality of the crystals obtained. A rational design of portions of both proteins should lead to an improvement in their crystallographic data and help add to the relatively limited crystallographic database on lignin degrading enzymes.

Future work

Purification of an active *Panus rudis* laccase separating the enzyme from all of the other components of the media in which it was present during the course of this experiment is vital. A redesign of the expression system followed by a newly designed purification strategy could be helpful in achieveing this. More characterisation of the pure enzyme could be done using model compounds to find out what are the best mediators for enhancing its activity, when thje enzyme needs mediators and at what concentration of enzyme and mediators, the enzyme is at its most optimal. A proper investigation of the bonds in lignin that the pure *Panus rudis* laccase actually acts on could be done first with smaller lignin model compounds and based on the results move on to technical lignins and even biomass feedstock. An experiment to properly separate the lignin into its component fractions such as gel permeation chromatography is necessary to see how this affects the *Panus rudis* laccase's activity. To get

better results from the FT-ICR mass spectrometry experiments, it would be useful to isolate any specifically useful or abundant degradation products from the degradation mix and carry out isotopic fine analysis and fragmentation experiments. This would help to validate the assignations and improve the accuracy of the assignments of the data overall. Using Liquid Chromatography Mass Spectrometry (LCMS) and Gas Chromatography Mass Chromatography (GC-MS) could also help in the identification of more of the compounds identified during the course of this project. For the dye-decolourising peroxidases, several alternatives from a redesign of the DNA construct, to a difference in the seeding conditions or method of the purified enzyme could help with the acquisition of the requisite structural data. A screen based on different additives could also be the key to finally obtaining protein crystals that produce good X-ray crystallography structural data. This is by no means an exhaustive list and other experiments could be proposed based on the results of those mentioned here as well.

References

Abdel-Hamid, A. M., Solbiati, J. O. & Cann, I. K. O. (2013) Chapter One - Insights into Lignin Degradation and its Potential Industrial Applications. *In:* SIMA, S. & GEOFFREY, M. G. (eds.) **Advances in Applied Microbiology**. Academic Press.

Adams, P. D., Afonine, P. V., Bunkoczi, G., Chen, V. B., Davis, I. W., Echols, N., Headd, J. J., Hung, L. W., Kapral, G. J., Grosse-Kunstleve, R. W., Mccoy, A. J., Moriarty, N. W., Oeffner, R., Read, R. J., Richardson, D. C., Richardson, J. S., Terwilliger, T. C. & Zwart, P. H. 2010. PHENIX: a comprehensive Python-based system for macromolecular structure solution. **Acta Crystallogr., Sect. D: Biol. Crystallogr.***,* 66(2)**:** pp.213-221.

Afonine, P. V., Grosse-Kunstleve, R. W., Echols, N., Headd, J. J., Moriarty, N. W., Mustyakimov, M., Terwilliger, T. C., Urzhumtsev, A., Zwart, P. H. & Adams, P. D. 2012. Towards automated crystallographic structure refinement with phenix.refine. **Acta Crystallogr., Sect. D: Biol. Crystallogr.***,* 68(4)**:** pp.352-367.

Ahmad, M., Roberts, J. N., Hardiman, E. M., Singh, R., Eltis, L. D. & Bugg, T. D. H. 2011. Identification of DypB from Rhodococcus jostii RHA1 as a lignin peroxidase. **Biochemistry***,* 50(23)**:** pp.5096-5107.

Ahvazi, B., Cloutier, E., Wojciechowicz, O. & Ngo, T.-D. 2016. Lignin Profiling: A Guide for Selecting Appropriate Lignins as Precursors in Biomaterials Development. **ACS Sustainable Chem. Eng.***,* 4(10)**:** pp.5090-5105.

Altschul, S. F., Gish, W., Miller, W., Myers, E. W. & Lipman, D. J. 1990. Basic local alignment search tool. **J Mol Biol***,* 215(3)**:** pp.403-10.

Araújo, A. S., Da Rocha, L. L., Tomazela, D. M., Sawaya, A. C. H. F., Almeida, R. R., Catharino, R. R. & Eberlin, M. N. 2005. Electrospray ionization mass spectrometry fingerprinting of beer. **Analyst***,* 130(6)**:** pp.884-889.

Azadi, P., Inderwildi, O. R., Farnood, R. & King, D. A. 2013. Liquid fuels, hydrogen and chemicals from lignin: A critical review. **Renewable and Sustainable Energy Reviews***,* 21(0)**:** pp.506-523.

Baldrian, P. 2006. Fungal laccases – occurrence and properties. **FEMS Microbiology Reviews**, 30(2): pp.215-242.

Bendtsen, J. D., Nielsen, H., Widdick, D., Palmer, T. & Brunak, S. 2005. Prediction of twin-arginine signal peptides. **BMC Bioinformatics**, 6167-167.

Boeriu, C. G., Bravo, D., Gosselink, R. J. A. & Van Dam, J. E. G. 2004. Characterisation of structure-dependent functional properties of lignin with infrared spectroscopy. **Industrial Crops and Products**, 20(2): pp.205-218.

Bonnefond, L., Schellenberger, P., Basquin, J., Demangeat, G., Ritzenthaler, C., Chênevert, R., Balg, C., Frugier, M., Rudinger-Thirion, J., Giegé, R., Lorber, B. & Sauter, C. 2011. Exploiting Protein Engineering and Crystal Polymorphism for Successful X-ray Structure Determination. **Crystal Growth & Design**, 11(10): pp.4334-4343.

Bourbonnais, R. & Paice, M. G. 1990. Oxidation of non-phenolic substrates: An expanded role for laccase in lignin biodegradation. **FEBS Letters**, 267(1): pp.99-102.

Bozell, J. J. 2014. Approaches to the Selective Catalytic Conversion of Lignin: A Grand Challenge for Biorefinery Development. **Top Curr Chem**.

Bugg, T. D. H., Ahmad, M., Hardiman, E. M. & Rahmanpour, R. 2011. Pathways for degradation of lignin in bacteria and fungi. **Natural Product Reports**, 28(12): pp.1883-1896.

Camarero, S., Sarkar, S., Ruiz-Duenas, F. J., Martinez, M. J. & Martinez, A. T. 1999. Description of a versatile peroxidase involved in the natural degradation of lignin that has both manganese peroxidase and lignin peroxidase substrate interaction sites. **J. Biol. Chem.**, 274(15): pp.10324-10330.

Chen, C., Shrestha, R., Jia, K., Gao, P. F., Geisbrecht, B. V., Bossmann, S. H., Shi, J. & Li, P. 2015. Characterization of Dye-decolorizing Peroxidase (DyP) from Thermomonospora curvata Reveals Unique Catalytic Properties of A-type DyPs. **Journal of Biological Chemistry**, 290(38): pp.23447-23463.

Chen, H., Ferrari, C., Angiuli, M., Yao, J., Raspi, C. & Bramanti, E. 2010a. Qualitative and quantitative analysis of wood samples by Fourier transform infrared spectroscopy and multivariate analysis. **Carbohydrate Polymers***,* 82(3)**:** pp.772-778.

Chen, V. B., Arendall, W. B., Iii, Headd, J. J., Keedy, D. A., Immormino, R. M., Kapral, G. J., Murray, L. W., Richardson, J. S. & Richardson, D. C. 2010b. MolProbity: all-atom structure validation for macromolecular crystallography. **Acta Crystallogr., Sect. D: Biol. Crystallogr.***,* 66(1)**:** pp.12-21.

Cheng, G., Kent, M. S., He, L., Varanasi, P., Dibble, D., Arora, R., Deng, K., Hong, K., Melnichenko, Y. B., Simmons, B. A. & Singh, S. 2012. Effect of Ionic Liquid Treatment on the Structures of Lignins in Solutions: Molecular Subunits Released from Lignin. **Langmuir***,* 28(32)**:** pp.11850-11857.

Claus, H. 2004. Laccases: structure, reactions, distribution. **Micron***,* 35(1-2)**:** pp.93-96.

Colpa, D. I., Fraaije, M. W. & Van Bloois, E. 2014. DyP-type peroxidases: a promising and versatile class of enzymes. **J. Ind. Microbiol. Biotechnol.***,* 41(1)**:** pp.1-7.

Corpet, F. 1988. Multiple sequence alignment with hierarchical clustering. **Nucleic Acids Res.***,* 16(22)**:** pp.10881-90.

Crestini, C., Melone, F., Sette, M. & Saladino, R. 2011. Milled Wood Lignin: A Linear Oligomer. **Biomacromolecules***,* 12(11)**:** pp.3928-3935.

Davis, I. W., Leaver-Fay, A., Chen, V. B., Block, J. N., Kapral, G. J., Wang, X., Murray, L. W., Arendall, W. B., 3rd, Snoeyink, J., Richardson, J. S. & Richardson, D. C. 2007. MolProbity: all-atom contacts and structure validation for proteins and nucleic acids. **Nucleic Acids Res***,* 35(Web Server issue)**:** pp.W375-83.

Doherty, W. O. S., Mousavioun, P. & Fellows, C. M. 2011. Value-adding to cellulosic ethanol: Lignin polymers. **Industrial Crops and Products***,* 33(2)**:** pp.259-276.

Dwivedi, U. N., Singh, P., Pandey, V. P. & Kumar, A. 2011. Structure-function relationship among bacterial, fungal and plant laccases. **Journal of Molecular Catalysis B: Enzymatic***,* 68(2)**:** pp.117-128.

Eggert, C., Temp, U., Dean, J. F. D. & Eriksson, K.-E. L. 1996. A fungal metabolite mediates degradation of non-phenolic lignin structures and synthetic lignin by laccase. **FEBS Letters***,* 391(1–2)**:** pp.144-148.

Emsley, P. 2017. Tools for ligand validation in Coot. **Acta Crystallogr., Sect. D: Struct. Biol.***,* 73(3)**:** pp.203-210.

Emsley, P. & Cowtan, K. 2004. Coot: model-building tools for molecular graphics. **Acta Crystallogr., Sect. D: Biol. Crystallogr.***,* D60(12, Pt. 1)**:** pp.2126-2132.

Emsley, P., Lohkamp, B., Scott, W. G. & Cowtan, K. 2010. Features and development of Coot. **Acta Crystallogr., Sect. D: Biol. Crystallogr.***,* 66(4)**:** pp.486-501.

Evans, P. R. 2011. An introduction to data reduction: Space-group determination, scaling and intensity statistics. **Acta Crystallogr., Sect. D: Biol. Crystallogr.***,* 67(4)**:** pp.282-292.

Evans, P. R. & Murshudov, G. N. 2013. How good are my data and what is the resolution? **Acta Crystallogr., Sect. D: Biol. Crystallogr.***,* 69(7)**:** pp.1204-1214.

Faix, O. (1991) Classification of Lignins from Different Botanical Origins by FT-IR Spectroscopy. **Holzforschung - International Journal of the Biology, Chemistry, Physics and Technology of Wood***.*

Faix, O. Fourier transform infrared spectroscopy [of lignin in solid state]. 1992. Springer, 83-109.

Ferrer, A., Alciaturi, C., Faneite, A. & Ríos, J. (2016) Analyses of Biomass Fibers by XRD, FT-IR, and NIR. *In:* VAZ JR, S. (ed.) **Analytical Techniques and Methods for Biomass***.* Cham: Springer International Publishing.

Fujii, H. (2016) Chapter 9 Model Complexes of Heme Peroxidases. **Heme Peroxidases***.* The Royal Society of Chemistry.

Gall, D. L., Kim, H., Lu, F., Donohue, T. J., Noguera, D. R. & Ralph, J. 2014. Stereochemical Features of Glutathione-dependent Enzymes in the Sphingobium sp. Strain SYK-6 β-Aryl Etherase Pathway. **Journal of Biological Chemistry**, 289(12)**:** pp.8656-8667.

Gall, D. L., Kontur, W. S., Lan, W., Kim, H., Li, Y., Ralph, J., Donohue, T. J. & Noguera, D. R. 2018. In Vitro Enzymatic Depolymerization of Lignin with Release of Syringyl, Guaiacyl, and Tricin Units. **Applied and Environmental Microbiology**, 84(3)**:** pp.

Gasteiger, E., Gattiker, A., Hoogland, C., Ivanyi, I., Appel, R. D. & Bairoch, A. 2003. ExPASy: the proteomics server for in-depth protein knowledge and analysis. **Nucleic Acids Res.**, 31(13)**:** pp.3784-3788.

Gianfreda, L., Xu, F. & Bollag, J.-M. 1999. Laccases: A useful group of oxidoreductive enzymes. **Biorem. J.**, 3(1)**:** pp.1-25.

Giardina, P., Faraco, V., Pezzella, C., Piscitelli, A., Vanhulle, S. & Sannia, G. 2010. Laccases: a never-ending story. **Cell Mol Life Sci**, 67(3)**:** pp.369-85.

Hakulinen, N., Andberg, M., Kallio, J., Koivula, A., Kruus, K. & Rouvinen, J. 2008. A near atomic resolution structure of a Melanocarpus albomyces laccase. **Journal of Structural Biology**, 162(1)**:** pp.29-39.

Hakulinen, N., Kiiskinen, L.-L., Kruus, K., Saloheimo, M., Paananen, A., Koivula, A. & Rouvinen, J. 2002. Crystal structure of a laccase from Melanocarpus albomyces with an intact trinuclear copper site. **Nature structural biology**, 9(8)**:** pp.601-605.

Higuchi, T. 1990. Lignin biochemistry: Biosynthesis and biodegradation. **Wood Science and Technology**, 24(1)**:** pp.23-63.

Higuchi, Y., Aoki, S., Takenami, H., Kamimura, N., Takahashi, K., Hishiyama, S., Lancefield, C. S., Ojo, O. S., Katayama, Y., Westwood, N. J. & Masai, E. 2018. Bacterial Catabolism of β-Hydroxypropiovanillone and β-Hydroxypropiosyringone Produced in the Reductive Cleavage of Arylglycerol-β-Aryl Ether in Lignin. **Applied and Environmental Microbiology**, 84(7)**:** pp.

Himmel, M. E., Ding, S.-Y., Johnson, D. K., Adney, W. S., Nimlos, M. R., Brady, J. W. & Foust, T. D. 2007. Biomass Recalcitrance: Engineering Plants and Enzymes for Biofuels Production. **Science**, 315(5813)**:** pp.804-807.

Hofrichter, M., Ullrich, R., Pecyna, M. J., Liers, C. & Lundell, T. 2010. New and classic families of secreted fungal heme peroxidases. **Appl. Microbiol. Biotechnol.**, 87(3)**:** pp.871-897.

Huang, H.-W., Zoppellaro, G. & Sakurai, T. 1999. Spectroscopic and kinetic studies on the oxygen-centered radical formed during the four-electron reduction process of dioxygen by Rhus vernicifera laccase. **J. Biol. Chem.**, 274(46)**:** pp.32718-32724.

Huang, Y., Wang, L., Chao, Y., Nawawi, D. S., Akiyama, T., Yokoyama, T. & Matsumoto, Y. 2012. Analysis of Lignin Aromatic Structure in Wood Based on the IR Spectrum. **J. Wood Chem. Technol.**, 32(4)**:** pp.294-303.

Jarrell, T. M., Marcum, C. L., Sheng, H., Owen, B. C., O'lenick, C. J., Maraun, H., Bozell, J. J. & Kenttamaa, H. I. 2014. Characterization of organosolv switchgrass lignin by using high performance liquid chromatography/high resolution tandem mass spectrometry using hydroxide-doped negative-ion mode electrospray ionization. **Green Chemistry**, 16(5)**:** pp.2713-2727.

Kabsch, W. 2010. XDS. **Acta Crystallographica Section D**, 66(2)**:** pp.125-132.

Karplus, P. A. & Diederichs, K. 2012. Linking Crystallographic Model and Data Quality. **Science**, 336(6084)**:** pp.1030-1033.

Kawai, S., Umezawa, T., Shimada, M. & Higuchi, T. 1988. Aromatic ring cleavage of 4,6-di(tert-butyl)guaiacol, a phenolic lignin model compound, by laccase of Coriolus versicolor. **FEBS Letters**, 236(2)**:** pp.309-311.

Kelly, B. T., Graham, S. C. & Owen, D. J. 2016. Using selenomethionyl derivatives to assign sequence in low-resolution structures of the AP2 clathrin adaptor. **Acta Crystallogr., Sect. D: Struct. Biol.**, 72(3)**:** pp.336-345.

Kew, W., Blackburn, J. W. T., Clarke, D. J. & Uhrín, D. 2017a. Interactive van Krevelen diagrams – Advanced visualisation of mass spectrometry data of complex mixtures. **Rapid Communications in Mass Spectrometry**, 31(7)**:** pp.658-662.

Kew, W., Goodall, I., Clarke, D. & Uhrín, D. 2017b. Chemical Diversity and Complexity of Scotch Whisky as Revealed by High-Resolution Mass Spectrometry. **Journal of The American Society for Mass Spectrometry**, 28(1)**:** pp.200-213.

Kim, S., Kramer, R. W. & Hatcher, P. G. 2003. Graphical Method for Analysis of Ultrahigh-Resolution Broadband Mass Spectra of Natural Organic Matter, the Van Krevelen Diagram. **Analytical Chemistry**, 75(20)**:** pp.5336-5344.

Kim, S. J. & Shoda, M. 1999. Purification and characterization of a novel peroxidase from Geotrichum candidum Dec 1 involved in decolorization of dyes. **Appl. Environ. Microbiol.**, 65(3)**:** pp.1029-1035.

Koch, B. P. & Dittmar, T. 2006. From mass to structure: an aromaticity index for high-resolution mass data of natural organic matter. **Rapid Communications in Mass Spectrometry**, 20(5)**:** pp.926-932.

Kontur, W. S., Bingman, C. A., Olmsted, C. N., Wassarman, D. R., Ulbrich, A., Gall, D. L., Smith, R. W., Yusko, L. M., Fox, B. G., Noguera, D. R., Coon, J. J. & Donohue, T. J. 2018. Novosphingobium aromaticivorans uses a Nu-class glutathione S-transferase as a glutathione lyase in breaking the β-aryl ether bond of lignin. **Journal of Biological Chemistry**, 293(14)**:** pp.4955-4968.

Krissinel, E. & Henrick, K. 2004. Secondary-structure matching (SSM), a new tool for fast protein structure alignment in three dimensions. **Acta Crystallogr D Biol Crystallogr**, 60(Pt 12 Pt 1)**:** pp.2256-68.

Krissinel, E. & Henrick, K. 2007. Inference of Macromolecular Assemblies from Crystalline State. **Journal of Molecular Biology**, 372(3)**:** pp.774-797.

Kujawinski, E. B., Freitas, M. A., Zang, X., Hatcher, P. G., Green-Church, K. B. & Jones, R. B. 2002. The application of electrospray ionization mass spectrometry (ESI MS) to the structural characterization of natural organic matter. **Organic Geochemistry***,* 33(3)**:** pp.171-180.

Kumar, S. V. S., Phale, P. S., Durani, S. & Wangikar, P. P. 2003. Combined sequence and structure analysis of the fungal laccase family. **Biotechnol. Bioeng.***,* 83(4)**:** pp.386-394.

Lancefield, C. S., Rashid, G. M. M., Bouxin, F., Wasak, A., Tu, W.-C., Hallett, J., Zein, S., Rodríguez, J., Jackson, S. D., Westwood, N. J. & Bugg, T. D. H. 2016. Investigation of the Chemocatalytic and Biocatalytic Valorization of a Range of Different Lignin Preparations: The Importance of β-O-4 Content. **ACS Sustainable Chemistry & Engineering***,* 4(12)**:** pp.6921-6930.

Lee, S.-K., Debeer George, S., Antholine, W. E., Hedman, B., Hodgson, K. O. & Solomon, E. I. 2002. Nature of the Intermediate Formed in the Reduction of O2 to H2O at the Trinuclear Copper Cluster Active Site in Native Laccase. **J. Am. Chem. Soc.***,* 124(21)**:** pp.6180-6193.

Li, K., Xu, F. & Eriksson, K. E. 1999. Comparison of fungal laccases and redox mediators in oxidation of a nonphenolic lignin model compound. **Appl Environ Microbiol***,* 65(6)**:** pp.2654-60.

Li, L.-L., Yuan, H., Liao, F., He, B., Gao, S.-Q., Wen, G.-B., Tan, X. & Lin, Y.-W. 2017. Rational design of artificial dye-decolorizing peroxidases using myoglobin by engineering Tyr/Trp in the heme center. **Dalton Transactions***,* 46(34)**:** pp.11230-11238.

Li, W., Cowley, A., Uludag, M., Gur, T., Mcwilliam, H., Squizzato, S., Park, Y. M., Buso, N. & Lopez, R. 2015. The EMBL-EBI bioinformatics web and programmatic tools framework. **Nucleic acids research***,* 43(W1)**:** pp.W580-4.

Liu, Q., Luo, L. & Zheng, L. 2018. Lignins: Biosynthesis and Biological Functions in Plants. **International Journal of Molecular Sciences***,* 19(2)**:** pp.335.

Liu, X., Du, Q., Wang, Z., Zhu, D., Huang, Y., Li, N., Wei, T., Xu, S. & Gu, L. 2011. Crystal Structure and Biochemical Features of EfeB/YcdB from Escherichia coli O157: ASP235 PLAYS DIVERGENT ROLES IN DIFFERENT ENZYME-CATALYZED PROCESSES. **Journal of Biological Chemistry***,* 286(17)**:** pp.14922-14931.

Liu, X., Yuan, Z., Wang, J., Cui, Y., Liu, S., Ma, Y., Gu, L. & Xu, S. 2017. Crystal structure and biochemical features of dye-decolorizing peroxidase YfeX from Escherichia coli O157 Asp143 and Arg232 play divergent roles toward different substrates. **Biochemical and Biophysical Research Communications***,* 484(1)**:** pp.40-44.

Long, L., Tian, D., Hu, J., Wang, F. & Saddler, J. 2017. A xylanase-aided enzymatic pretreatment facilitates cellulose nanofibrillation. **Bioresource Technology***,* 243898-904.

Lukk, T., Hetta, A. M. A., Jones, A., Solbiati, J., Majumdar, S., Cronan, J. E., J.A., G. & Nair, S. K. 2013. DyP-type peroxidases from Stretptomyces and Thermobifida can modify organosolv lignin. **To be published**.

Lupoi, J. S., Singh, S., Parthasarathi, R., Simmons, B. A. & Henry, R. J. 2015. Recent innovations in analytical methods for the qualitative and quantitative assessment of lignin. **Renewable and Sustainable Energy Reviews***,* 49871-906.

Macfarlane, A. L., Mai, M. & Kadla, J. F. (2014) 20 - Bio-based chemicals from biorefining: lignin conversion and utilisation. *In:* WALDRON, K. (ed.) **Advances in Biorefineries***.* Woodhead Publishing.

Madhavi, V. & Lele, S. S. 2009. Laccase: properties and applications. **BioResources***,* 4(4)**:** pp.No pp. given.

Maldhure, A. V., Ekhe, J. D. & Deenadayalan, E. 2012. Mechanical properties of polypropylene blended with esterified and alkylated lignin. **Journal of Applied Polymer Science***,* 125(3)**:** pp.1701-1712.

Marjasvaara, A., Torvinen, M. & Vainiotalo, P. 2005. Laccase-catalyzed mediated oxidation of benzyl alcohol: the role of TEMPO and formation of products including benzonitrile studied by nanoelectrospray ionization Fourier transform ion cyclotron resonance mass spectrometry. **J. Mass Spectrom.***,* 39(10)**:** pp.1139-1146.

Martinez, A. T., Speranza, M., Ruiz-Duenas, F. J., Ferreira, P., Camarero, S., Guillen, F., Martinez, M. J., Gutierrez, A. & Del Rio, J. C. 2005. Biodegradation of lignocellulosics: Microbial, chemical, and enzymatic aspects of the fungal attack of lignin. **Int. Microbiol.***,* 8(3)**:** pp.195-204.

Martínez, A. T., Ruiz-Dueñas, F. J., Camarero, S., Serrano, A., Linde, D., Lund, H., Vind, J., Tovborg, M., Herold-Majumdar, O. M., Hofrichter, M., Liers, C., Ullrich, R., Scheibner, K., Sannia, G., Piscitelli, A., Pezzella, C., Sener, M. E., Kılıç, S., Van Berkel, W. J. H., Guallar, V., Lucas, M. F., Zuhse, R., Ludwig, R., Hollmann, F., Fernández-Fueyo, E., Record, E., Faulds, C. B., Tortajada, M., Winckelmann, I., Rasmussen, J.-A., Gelo-Pujic, M., Gutiérrez, A., Del Río, J. C., Rencoret, J. & Alcalde, M. 2017. Oxidoreductases on their way to industrial biotransformations. **Biotechnology Advances***,* 35(6)**:** pp.815-831.

Martínez, Á. T., Speranza, M., Ruiz-Dueñas, F. J., Ferreira, P., Camarero, S., Guillén, F., Martínez, M. J., Gutiérrez, A. & Del Río, J. C. 2005. Biodegradation of lignocellulosics: Microbial, chemical, and enzymatic aspects of the fungal attack of lignin. **International Microbiology***,* 8(3)**:** pp.195-204.

Mccoy, A. J., Grosse-Kunstleve, R. W., Adams, P. D., Winn, M. D., Storoni, L. C. & Read, R. J. 2007. Phaser crystallographic software. **J. Appl. Crystallogr.***,* 40(4)**:** pp.658-674.

Mendes, S., Catarino, T., Silveira, C., Todorovic, S. & Martins, L. O. 2015. The catalytic mechanism of A-type dye-decolourising peroxidase BsDyP: neither aspartate nor arginine is individually essential for peroxidase activity. **Catalysis Science & Technology***,* 5(12)**:** pp.5196-5207.

Miettinen, I., Mäkinen, M., Vilppo, T. & Jänis, J. 2015. Compositional Characterization of Phase-Separated Pine Wood Slow Pyrolysis Oil by Negative-Ion Electrospray Ionization Fourier Transform Ion Cyclotron Resonance Mass Spectrometry. **Energy & Fuels***,* 29(3)**:** pp.1758-1765.

Millis, C. D., Cai, D., Stankovich, M. T. & Tien, M. 1989. Oxidation-reduction potentials and ionization states of extracellular peroxidases from the lignin-degrading fungus Phanerochaete chrysosporium. **Biochemistry***,* 28(21)**:** pp.8484-9.

Morozova, O. V., Shumakovich, G. P., Gorbacheva, M. A., Shleev, S. V. & Yaropolov, A. I. 2007. “Blue” laccases. **Biochemistry (Moscow)***,* 72(10)**:** pp.1136-1150.

Mukhopadhyay, M. & Banerjee, R. 2015. Yellow Laccase-Mediated Lignin Degradation of Ricinus communis: A Future Agricultural Biomass for Biofuel Production. **Agricultural Research***,* 4(3)**:** pp.309-318.

Nitta, K., Kataoka, K. & Sakurai, T. 2002. Primary structure of a Japanese lacquer tree laccase as a prototype enzyme of multicopper oxidases. **Journal of Inorganic Biochemistry***,* 91(1)**:** pp.125-131.

Otterbein, L., Record, E., Longhi, S., Asther, M. & Moukha, S. 2000. Molecular cloning of the cDNA encoding laccase from Pycnoporus cinnabarinus I-937 and expression in Pichia pastoris. **European Journal of Biochemistry***,* 267(6)**:** pp.1619-1625.

Ozer, A., Uzuner, U., Guler, H. I., Ay Sal, F., Belduz, A. O., Deniz, I. & Canakci, S. 2017. Improved pulp bleaching potential of Bacillus subtilis WB800 through overexpression of three lignolytic enzymes from various bacteria. **Biotechnology and Applied Biochemistry***,* 65(4)**:** pp.560-571.

Paliwal, R., Rawat, A. P., Rawat, M. & Rai, J. P. N. 2012. Bioligninolysis: Recent Updates for Biotechnological Solution. **Applied Biochemistry and Biotechnology***,* 167(7)**:** pp.1865-1889.

Pandey, M. P. & Kim, C. S. 2011. Lignin Depolymerization and Conversion: A Review of Thermochemical Methods. **Chemical Engineering & Technology***,* 34(1)**:** pp.29-41.

Pardo, I., Chanaga, X., Vicente, A. I., Alcalde, M. & Camarero, S. 2013. New colorimetric screening assays for the directed evolution of fungal laccases to improve the conversion of plant biomass. **BMC Biotechnol.***,* 1390.

Pereira, J. H., Heins, R. A., Gall, D. L., Mcandrew, R. P., Deng, K., Holland, K. C., Donohue, T. J., Noguera, D. R., Simmons, B. A., Sale, K. L., Ralph, J. & Adams, P. D. 2016. Structural and Biochemical Characterization of the Early and Late Enzymes in the Lignin β-Aryl Ether

Cleavage Pathway from Sphingobium sp. SYK-6. **Journal of Biological Chemistry**, 291(19)**:** pp.10228-10238.

Petersen, T. N., Brunak, S., Von Heijne, G. & Nielsen, H. 2011. SignalP 4.0: discriminating signal peptides from transmembrane regions. **Nature Methods**, 8785.

Pfanzagl, V., Nys, K., Bellei, M., Michlits, H., Mlynek, G., Battistuzzi, G., Djinovic-Carugo, K., Van Doorslaer, S., Furtmüller, P. G., Hofbauer, S. & Obinger, C. 2018. Roles of distal aspartate and arginine of B-class dye-decolorizing peroxidase in heterolytic hydrogen peroxide cleavage. **Journal of Biological Chemistry**, 293(38)**:** pp.14823-14838.

Piontek, K., Antorini, M. & Choinowski, T. 2002a. Crystal structure of a laccase from the fungus Trametes versicolor at 1.90-A resolution containing a full complement of coppers. **J Biol Chem**, 277(40)**:** pp.37663-9.

Piontek, K., Antorini, M. & Choinowski, T. 2002b. Crystal Structure of a Laccase from the FungusTrametes versicolor at 1.90-Å Resolution Containing a Full Complement of Coppers. **Journal of Biological Chemistry**, 277(40)**:** pp.37663-37669.

Popescu, C.-M., Popescu, M.-C., Singurel, G., Vasile, C., Argyropoulos, D. S. & Willfor, S. 2007. Spectral characterization of eucalyptus wood. **Appl. Spectrosc.**, 61(11)**:** pp.1168-1177.

Rahmanpour, R., Rea, D., Jamshidi, S., Fülöp, V. & Bugg, T. D. H. 2016. Structure of Thermobifida fusca DyP-type peroxidase and activity towards Kraft lignin and lignin model compounds. **Archives of Biochemistry and Biophysics**, 59454-60.

Ralph, J., Lundquist, K., Brunow, G., Lu, F., Kim, H., Schatz, P., Marita, J., Hatfield, R., Ralph, S., Christensen, J. & Boerjan, W. 2004. Lignins: Natural polymers from oxidative coupling of 4-hydroxyphenyl- propanoids. **Phytochemistry Reviews**, 3(1-2)**:** pp.29-60.

Rasmussen, S. & Dixon, R. A. 1999. Transgene-Mediated and Elicitor-Induced Perturbation of Metabolic Channeling at the Entry Point into the Phenylpropanoid Pathway. **The Plant Cell**, 11(8)**:** pp.1537-1551.

Reiss, R., Ihssen, J., Richter, M., Eichhorn, E., Schilling, B. & Thöny-Meyer, L. 2013. Laccase *versus* Laccase-Like Multi-Copper Oxidase: A Comparative Study of Similar Enzymes with Diverse Substrate Spectra. **PLoS ONE***,* 8(6)**:** pp.e65633.

Robert, X. & Gouet, P. 2014. Deciphering key features in protein structures with the new ENDscript server. **Nucleic Acids Research***,* 42(W1)**:** pp.W320-W324.

Rosini, E., Allegretti, C., Melis, R., Cerioli, L., Conti, G., Pollegioni, L. & D'arrigo, P. 2016. Cascade enzymatic cleavage of the β-O-4 linkage in a lignin model compound. **Catalysis Science & Technology***,* 6(7)**:** pp.2195-2205.

Rossmann, M. G. 2001. Molecular replacement - historical background. **Acta Crystallogr., Sect. D: Biol. Crystallogr.***,* D57(10)**:** pp.1360-1366.

Ruiz-Dueñas, F. J., Morales, M., García, E., Miki, Y., Martínez, M. J. & Martínez, A. T. 2009. Substrate oxidation sites in versatile peroxidase and other basidiomycete peroxidases. **Journal of Experimental Botany***,* 60(2)**:** pp.441-452.

Rupp, B. (2010) **Biomolecular crystallography : principles, practice, and application to structural biology***,* New York, N.Y. ; Abbingdon, New York, N.Y. ; Abbingdon : Garland Science.

Sailaja, R. R. N. & Deepthi, M. V. 2010. Mechanical and thermal properties of compatibilized composites of polyethylene and esterified lignin. **Materials & Design***,* 31(9)**:** pp.4369-4379.

Santos, A., Mendes, S., Brissos, V. & Martins, L. 2014. New dye-decolorizing peroxidases from Bacillus subtilis and Pseudomonas putida MET94: towards biotechnological applications. **Applied Microbiology and Biotechnology***,* 98(5)**:** pp.2053-2065.

Sato, Y., Moriuchi, H., Hishiyama, S., Otsuka, Y., Oshima, K., Kasai, D., Nakamura, M., Ohara, S., Katayama, Y., Fukuda, M. & Masai, E. 2009. Identification of Three Alcohol Dehydrogenase Genes Involved in the Stereospecific Catabolism of Arylglycerol-β-Aryl Ether by Sphingobium sp. Strain SYK-6. **Applied and Environmental Microbiology***,* 75(16)**:** pp.5195.

Schrodinger, Llc. (2015) The PyMOL Molecular Graphics System, Version 1.8.

Schwanninger, M., Rodrigues, J. C., Pereira, H. & Hinterstoisser, B. 2004. Effects of short-time vibratory ball milling on the shape of FT-IR spectra of wood and cellulose. **Vibrational Spectroscopy***,* 36(1)**:** pp.23-40.

Sezer, M., Santos, A., Kielb, P., Pinto, T., Martins, L. O. & Todorovic, S. 2013. Distinct Structural and Redox Properties of the Heme Active Site in Bacterial Dye Decolorizing Peroxidase-Type Peroxidases from Two Subfamilies: Resonance Raman and Electrochemical Study. **Biochemistry***,* 52(18)**:** pp.3074-3084.

Sigoillot, J.-C., Berrin, J.-G., Bey, M., Lesage-Meessen, L., Levasseur, A., Lomascolo, A., Record, E. & Uzan-Boukhris, E. (2012) Chapter 8 - Fungal Strategies for Lignin Degradation. *In:* LISE, J. & CATHERINE, L. (eds.) **Advances in Botanical Research***.* Academic Press.

Singh, R., Grigg, J. C., Armstrong, Z., Murphy, M. E. P. & Eltis, L. D. 2012. Distal Heme Pocket Residues of B-type Dye-decolorizing Peroxidase: Arginine but not Aspartate is Essential for Peroxidase Activity. **J. Biol. Chem.***,* 287(13)**:** pp.10623-10630.

Singhvi, M. S., Chaudhari, S. & Gokhale, D. V. 2014. Lignocellulose processing: a current challenge. **RSC Adv.***,* 4(16)**:** pp.8271-8277.

Sivalingam, G. N., Yan, J., Sahota, H. & Thalassinos, K. 2013. Amphitrite: A program for processing travelling wave ion mobility mass spectrometry data. **International Journal of Mass Spectrometry***,* 345-34754-62.

Solomon, E. I., Sundaram, U. M. & Machonkin, T. E. 1996. Multicopper Oxidases and Oxygenases. **Chem. Rev. (Washington, D. C.)***,* 96(7)**:** pp.2563-2605.

Stein, N. 2008. CHAINSAW : a program for mutating pdb files used as templates in molecular replacement. **Journal of Applied Crystallography***,* 41(3)**:** pp.641-643.

Stenson, A. C., Marshall, A. G. & Cooper, W. T. 2003. Exact Masses and Chemical Formulas of Individual Suwannee River Fulvic Acids from Ultrahigh Resolution Electrospray Ionization Fourier Transform Ion Cyclotron Resonance Mass Spectra. **Analytical Chemistry***,* 75(6)**:** pp.1275-1284.

Sugano, Y. 2009. DyP-type peroxidases comprise a novel heme peroxidase family. **Cell. Mol. Life Sci.**, 66(8)**:** pp.1387-1403.

Sugano, Y., Muramatsu, R., Ichiyanagi, A., Sato, T. & Shoda, M. 2007. DyP, a unique dye-decolorizing peroxidase, represents a novel heme peroxidase family: ASP171 replaces the distal histidine of classical peroxidases. **J Biol Chem**, 282(50)**:** pp.36652-8.

Tessarolo, N. S., Silva, R. V. S., Vanini, G., Casilli, A., Ximenes, V. L., Mendes, F. L., De Rezende Pinho, A., Romão, W., De Castro, E. V. R., Kaiser, C. R. & Azevedo, D. A. 2016. Characterization of thermal and catalytic pyrolysis bio-oils by high-resolution techniques: 1H NMR, GC×GC-TOFMS and FT-ICR MS. **Journal of Analytical and Applied Pyrolysis**, 117257-267.

Van Den Ent, F., Lockhart, A., Kendrick-Jones, J. & Löwe, J. 1999. Crystal structure of the N-terminal domain of MukB: a protein involved in chromosome partitioning. **Structure**, 7(10)**:** pp.1181-1187.

Vanholme, R., Morreel, K., Ralph, J. & Boerjan, W. 2008. Lignin engineering. **Current Opinion in Plant Biology**, 11(3)**:** pp.278-285.

Vanitjinda, G., Nimchua, T. & Sukyai, P. 2019. Effect of xylanase-assisted pretreatment on the properties of cellulose and regenerated cellulose films from sugarcane bagasse. **International Journal of Biological Macromolecules**, 122503-516.

Vishtal, A. & Kraslawski, A. 2011. CHALLENGES IN INDUSTRIAL APPLICATIONS OF TECHNICAL LIGNINS. **BioResources**, 6(3)**:** pp.3547-3568.

Wang, Y., Liu, Q., Yan, L., Gao, Y., Wang, Y. & Wang, W. 2013. A novel lignin degradation bacterial consortium for efficient pulping. **Bioresource Technology**, 139113-119.

Wei, W. & Wu, S. 2017. Depolymerization of cellulose into high-value chemicals by using synergy of zinc chloride hydrate and sulfate ion promoted titania catalyst. **Bioresource Technology**, 241760-766.

Weng, J.-K., Li, X., Bonawitz, N. D. & Chapple, C. 2008. Emerging strategies of lignin engineering and degradation for cellulosic biofuel production. **Current Opinion in Biotechnology**, 19(2)**:** pp.166-172.

Wong, D. W. S. 2009. Structure and action mechanism of ligninolytic enzymes. **Appl. Biochem. Biotechnol.**, 157(2)**:** pp.174-209.

Wu, Z., Rodgers, R. P. & Marshall, A. G. 2004. Two- and Three-Dimensional van Krevelen Diagrams: A Graphical Analysis Complementary to the Kendrick Mass Plot for Sorting Elemental Compositions of Complex Organic Mixtures Based on Ultrahigh-Resolution Broadband Fourier Transform Ion Cyclotron Resonance Mass Measurements. **Analytical Chemistry**, 76(9)**:** pp.2511-2516.

Xu, F., Shin, W., Brown, S. H., Wahleithner, J. A., Sundaram, U. M. & Solomon, E. I. 1996. A study of a series of recombinant fungal laccases and bilirubin oxidase that exhibit significant differences in redox potential, substrate specificity, and stability. **Biochim Biophys Acta**, 1292(2)**:** pp.303-11.

Yang, C., Yue, F., Cui, Y., Xu, Y., Shan, Y., Liu, B., Zhou, Y. & Lü, X. 2018. Biodegradation of lignin by Pseudomonas sp. Q18 and the characterization of a novel bacterial DyP-type peroxidase. **Journal of Industrial Microbiology & Biotechnology**, 45(10)**:** pp.913-927.

Yoshida, H. 1883. Yoshida: Chemistry of lacquer (Urushi). **J. Chem. Soc., Trans.**, 43472-486.

Yoshida, K., Cheynier, V. & Quideau, S. (2016) **Recent Advances in Polyphenol Research**.

Yoshida, T., Tsuge, H., Konno, H., Hisabori, T. & Sugano, Y. 2011. The catalytic mechanism of dye-decolorizing peroxidase DyP may require the swinging movement of an aspartic acid residue. **FEBS J**, 278(13)**:** pp.2387-94.

Zhang, M., Wu, F., Wei, Z., Xiao, Y. & Gong, W. 2006. Characterization and decolorization ability of a laccase from Panus rudis. **Enzyme and Microbial Technology**, 39(1)**:** pp.92-97.

Zhao, C. & Lercher, J. A. (2013) Chapter 9 - Catalytic Depolymerization and Deoxygenation of Lignin A2 - Triantafyllidis, Kostas S. *In:* LAPPAS, A. A. & STÖCKER, M. (eds.) **The Role of Catalysis for the Sustainable Production of Bio-fuels and Bio-chemicals**. Amsterdam: Elsevier.

Zubieta, C., Joseph, R., Krishna, S. S., Mcmullan, D., Kapoor, M., Axelrod, H. L., Miller, M. D., Abdubek, P., Acosta, C., Astakhova, T., Carlton, D., Chiu, H.-J., Clayton, T., Deller, M. C., Duan, L., Elias, Y., Elsliger, M.-A., Feuerhelm, J., Grzechnik, S. K., Hale, J., Han, G. W., Jaroszewski, L., Jin, K. K., Klock, H. E., Knuth, M. W., Kozbial, P., Kumar, A., Marciano, D., Morse, A. T., Murphy, K. D., Nigoghossian, E., Okach, L., Oommachen, S., Reyes, R., Rife, C. L., Schimmel, P., Trout, C. V., Van Den Bedem, H., Weekes, D., White, A., Xu, Q., Hodgson, K. O., Wooley, J., Deacon, A. M., Godzik, A., Lesley, S. A. & Wilson, I. A. 2007. Identification and structural characterization of heme binding in a novel dye-decolorizing peroxidase, TyrA. **Proteins: Struct., Funct., Bioinf.***,* 69(2)**:** pp.234-243.